Tampere University

Antti Laitinen

UTILIZATION OF DRONES IN VERTICAL PROFILE MEASUREMENTS OF THE ATMOSPHERE

Faculty of engineering and natural sciences
Master of science thesis
July 2019

ABSTRACT

ANTTI LAITINEN: Utilization of drones in vertical profile measurements of the atmosphere
Tampere University
Masters thesis, 74 pages
July 2019
Master of science degree programme in science and engineering
Major: Advanced engineering physics
Examiners: Prof. Miikka Dal Maso and Dr. Anne Hirsikko

Keywords: Drone, weather, vertical profiling, temperature, humidity, UAV

Numerical weather predicition and climate models require accurate and continuous measurements of the atmosphere. Radiosoundings conducted daily all over the world provide the backbone for these measurements thanks to their accuracy and high spatial resolution. However they are expensive and thus are limited to only a few profile measurements per day. Especially within boundary layer this is not enough and to fill this gap a new type of drone-based measurement system has been developed. The recent emergence of drones has brought new opportunities in atmospheric research and in this study their utilization in meteorological profiling is investigated.

The measurement system consists of an octocopter with a Vaisala RD41 dropsonde attached underneath for temperature and humidity measurements. This drone is accompanied by a custom-build ground station that allows autonomous operation. With the drone measurements up to 450 m were possible.

To investigate the capabilities of drone-borne setups for vertical profiling, the temperature and humidity measurements were compared between ascending and descending legs of the flight as well as collocated radiosonde measurements. Statistical analysis on the differences between the measured profiles was conducted and individual case studies were performed for better understanding of the effects caused by the drone and the different atmospheric conditions.

The results indicate a warm bias in the drone measurements when compared against radiosonde measurements, and this bias is higher during the ascend leg. Ascend leg shows a bias of 0.4 °C when compared against the radiosonde measurements and the descend leg shows a bias of 0.2 °C. The ascend leg shows a bias of 0.3 °C when compared against the descend leg. The relative humidity measurements with the drone show a dry bias when compared against radiosonde measurements. The ascending leg has a bias of -1.9 % and the descending leg -0.3 %. The difference between ascend and descend legs is -1.4 %. Thus the descending leg agrees better with the radiosonde measurements, but also the ascending leg generally agrees with the radiosonde measurements within half a degree in temperature and two percentage relative humidity.

TIIVISTELMÄ

ANTTI LAITINEN: Droonien hyödyntäminen ilmakehän pystyprofiilimittauksissa
Tampereen yliopisto
Diplomityö, 74 sivua
Heinäkuu 2019
Teknis-Luonnontieteellinen DI-tutkinto-ohjelma
Pääaine: Teknillinen fysiikka
Tarkastajat: Prof. Miikka Dal Maso ja FT Anne Hirsikko

Avainsanat: Drooni, sääpalvelut, pystyprofiili, lämpötila, kosteus

Numeerinen sääennustaminen sekä ilmastomallit vaativat tarkkoja ja jatkuvia mittauksia ilmakehän tilasta. Tarkat ja hyvällä korkeusresoluutiolla tehtävät radioluotaukset muodostavat perustan näille mittauksille. Radioluotaukset ovat kuitenkin kalliita toteuttaa ja tästä syystä niiden kattavuus rajoittuu muutamaan pystyprofiiliin päivässä. Erityisesti rajakerroksen tutkimiseen tämä ei riitä ja tästä syystä on kehitetty uudentyyppien droonialusta ilmakehän mittaamiseen. Droonien yleistyminen viime vuosina on tuonut uusia mahdollisuuksia myös ilmakehätutkimukseen ja tässä työssä tutkitaan niiden soveltuvuutta meteorologiseen profilointiin.

Käytetty mittauslaitteisto koostuu kahdeksanroottorisesta multikopterista (drooni) jonka alapuolelle on kiinnitetty Vaisalan RD41 dropsondi lämpötilan ja kosteuden mittaamiseen. Laitteistoon kuuluu lisäksi maa-asema joka mahdollistaa mittausten tekemisen itsenäisesti. Käytetyllä droonilla mittauksia pystytään tekemään 450 m asti.

Laitteiston kyvykyyden tutkimiseksi mitattuja lämpötila- ja kosteusprofiileja vertailtiin lennon nousevan ja laskevan osuuden kesken sekä referenssiluotauksiin. Havaittuja eroja analysoitiin käyttäen tilastollisia menetelmiä sekä tarkastelemalla yksittäisiä profiileja.

Työn tulokset viittaavat siihen että drooniin perustuva laitteisto mittaa hieman korkeampaa lämpötilaa kuin luotaukset, ja ylösnousevalla osuudella tämä ero on suurempi. Nouseva osuus näyttää keskimäärin 0.4 °C korkeampaa lämpötilaa kuin vastaava radioluotaus ja laskeva 0.2 °C. Verrattaessa nousevaa ja laskevaa osuutta keskenään näyttää nouseva noin 0.3 °C korkeampaa lämpötilaa. Suhteellisen kosteuden mittauksessa laitteisto mittaa matalampaa kosteutta kuin luotaukset. Ero nousevan osuuden ja luotausten välillä on noin -1.9 % ja laskevan ja luotausten välillä noin -0.3 %. Ero nousevan ja laskevan osuuden välillä suhteellisessa kosteudessa on noin -1.4 %. Tulokset osoittavat että alastuleva osuus vastaa luotauksia paremmin kuin nouseva. Kuitenkin myös nouseva osuus vastaa luotauksia noin puolen asteen tarkkuudella lämpötilassa ja kahden prosentin tarkkuudella suhteellisessa kosteudessa.

PREFACE

Working on this thesis has been a time consuming but also very rewarding. It has been really interesting to work with a system that is still under development and could potentially bring many new aspects to atmospheric measurements. This work will also conclude over 6 years of studies at Tampere University of Technology (or Tampere University as it is known by the time of writing this thesis), a period in my life that I will surely long for.

First and foremost I want to thank my advisors Anne Hirsikko from the Finnish Meteorological Institute, who offered me this project to work on and Miikka Dal Maso from Tampere University for agreeing to examine my work. Both have also given invaluable guidance during my work. I also thank Jarkko Hirvonen for helping with the meteorological aspect of the analysis, Jani Gustafsson for the technical guidance and the observations unit for the working atmosphere. Additionally I want to thank my friends, family and especially my girlfriend Stephanie for their support throughout my thesis.

Geneve, 23.7.2019

Antti Laitinen

CONTENTS

ABBREVIATIONS

FMI	Finnish Meteorological Institute
MWR	Microwave radiometer
LiDAR	Light detection and ranging
GRUAN	(Global Climate Observing System) Reference Upper-Air Network
UAV	Unmanned aerial vehicle
RTD	Resistor temperature detector
NTC	Negative temperature coefficient
PRTD	Platinum resistor temperture detector
RH	Relative humidity
AGL	Above ground level
ASL	Above sea level
IQR	Interquartile range
RMSE	Root mean squared error

1. INTRODUCTION

Weather affects the daily life of everyone, and thus weather forecasts are of general interest. This has been the case since ancient times, when people were trying to forecast weather based on cloud formation and the movement of earth around the sun. The weather forecast techniques have certainly improved since these times, and today the advanced numerical weather models help the meteorologists to forecast the upcoming weather with increased accuracy. Nowadays it is also increasingly important to have accurate predictions of upcoming weather. Number of sectors have especially need for accurate weather forecasts, such as aviation, marine transit and agriculture to name a few. Accurate weather forecasts are also important in prediction of hazardous weather, in order to give enough time for preparation.

High-resolution forecast models have been implemented to forecast these hazardous weather events (Illingworth *et al.* 2015). However, in order for these models to perform well, accurate, continuous and high-resolution measurements of the atmosphere are needed. Atmospheric measurements are also required for validation of the forecast models.

There are number of different instruments developed for atmospheric measurements. These can be categorized in two groups: remote sensing and in-situ measurements. Remote sensing instruments typically use the scattering or emissions of electromagnetic waves such as light from the atmosphere to determine condition of atmosphere. These instruments tend to have high temporal resolution. In-situ instruments can be stationed on ground level or fixed on radiosondes or airplanes. Currently the most widely used measurement instrument for meteorological profiling of the atmosphere is the radiosonde, which has been in use for decades and has been proven to be reliable, accurate and unmatched in vertical profiling of the atmosphere. However they also have their drawbacks: radiosondes are generally disposable since after measuring throughout the atmosphere the balloon which the radiosonde is attached to will burst and the sonde falls on the ground, possibly in remote area where retrieving is difficult or impossible. This significantly raises the costs of radio sounding since each sounding requires a new sensor. This also severely limits the temporal resolution of radio soundings. For example in Finland the Finnish Meteorological Institute (FMI) conducts soundings four times a day which, when taken into account the variable characteristics of atmosphere through the day, is insufficient. Especially the boundary layer varies strongly during the day and measurements within the boundary layer are important. One might also consider the environmental impact of the falling debris which might not be disposed correctly. Yet there has not been a single instrument to replace radiosondes and they continue to be used on daily basis all over the world.

A new type of in-situ measurement is made possible by emergence of drones or multicopters, which provide a new way to conduct in-situ measurements especially in the lower atmosphere. In the oxford dictionary, drone is defined as "unmanned aerial vehicle commanded over radio link" and further that "Drones range from large winged aircraft ... to a small multiple-rotor helicopters used by hobbyists for both indoor and outdoor use." (Butterfield & Szymanski 2018). In this thesis the word drone refers to a multiple-rotor helicopter. More detailed information on the used drone is found on section 3.1. These drones provide new and exciting opportunities for atmospheric measurements. Increased control in three dimensions over radiosondes provide better spatial accuracy both in horizontal and vertical directions.

In atmospheric sciences drones have already been harnessed for measurements of atmospheric aerosols and air quality (Kuuluvainen *et al.* 2018). and investigation of turbulence in boundary layer (Båserud *et al.* 2016). Few studies have also harnessed different types of unmanned aerial vehicles for meteorological profiling of the atmosphere (Martin *et al.* (2011), Palomaki *et al.* (2017), Jonassen *et al.* (2015), Greene *et al.* (2019)). Fixed-wing drones have been more commonly used for vertical profiling, but also multicopters have been harnessed for this purpose.

In a pilot study conducted by the FMI an octocopter with capabilities for autonomous operation has been equipped with Vaisala RD41 dropsonde for temperature and humidity measurements. The measurements are made at a measurement site in Jokioinen in order to evaluate the performance of the drone setup for meteorological profiling. Radiosoundings are performed four times a day at the site, allowing comparison against measurements made by radiosondes.

The aim of this thesis is to evaluate the capabilities of drones as measurements instruments of the atmosphere and compare them to existing instruments. Especially the emphasis is on how the measurements differ between ascending and descending legs of the drone flight and how the drone compares against radiosonde measurements. The questions this thesis aims to answer are: how and why do the measured temperature and humidity differ between the ascending and descending leg of the drone flight, how do they compare against radiosondes and are drones viable option for vertical profiling of the atmosphere?

The first chapter of this thesis provides a general outlook on the other currently used instruments for vertical profiling in order to understand the strengths and weaknesses of existing instruments. In addition the principles of the measurement sensors mounted on the drone are presented to understand how the measurements are taken and what affects the measured quantities. The second chapter presents the measurement site and the measurement setup as well as the used methods for the data acquisition, correction and analysis. The third chapter presents the results from two measured profiles and the statistical analysis of the measured data set. Finally, the fourth chapter is the discussion chapter where the analysis and the results are wrapped up and the conclusions are presented.

2. COMMONLY USED INSTRUMENTS AND SENSORS

The most common instruments used for atmospheric profiling are microwaveradiometers, lidars and radiosondes. Out of these three microwaveradiometers and lidars are remote sensing instruments, which use electromagnetic waves emitted or reflected from the atmosphere in order to determine the condition of the atmosphere. Radiosondes are in-situ instruments, carrying sensors attached on a balloon through the atmosphere, allowing in-situ measurements at different heights. For the in-situ measurements different types of temperature and humidity sensors have been developed.

2.1 Microwave radiometer

Microwaveradiometer (MWR) measures the emission in microwave wavelength range (1 GHz to 170 GHz). In the atmosphere this emission mainly comes from gases, which emit radiation due to thermal radiation. This radiation can be modelled by blackbody radiation, as stated by Plank's law

$$L(T,\lambda) = \frac{2hc^2}{\lambda^5}\frac{1}{e^{hc/\lambda k_B T}-1} \tag{1}$$

where $L(T,\lambda)$ is the emitted power per surface area per steradian ($\mathrm{W\,m^{-3}sr^{-1}}$), h is the Plank's constant, c is the speed of light, λ is the emitted wavelength and k_B is the boltzmann constant. In order to solve T from this equation, a Rayleigh-Jeans approximation can be used: when λ is large, the term $e^{hc/\lambda k_B T}$ is small. Then, by applying taylor expansion for e^x yields

$$e^x \approx 1 + x + \frac{x^2}{2!} + \frac{x^3}{3!}...$$

and for small x, $e^x \approx 1+x$. Applying this approximation for equation 1, with $x = \frac{hc}{\lambda k_B T}$, the expression for $L(T,\lambda)$ can be simplified into

$$L(T,\lambda) \approx \frac{2hc^2}{\lambda^5}\frac{1}{1+\frac{hc}{\lambda k_B T}-1} = \frac{2hc^2}{\lambda^5}\frac{1}{\frac{hc}{\lambda k_B T}} = \frac{2k_B T c}{\lambda^4} \tag{2}$$

from which T can, in principle, be solved:

$$T = \frac{L(T,\lambda)\lambda^4}{2k_B c}. \tag{3}$$

Derivation follows an example by Rees (2012).

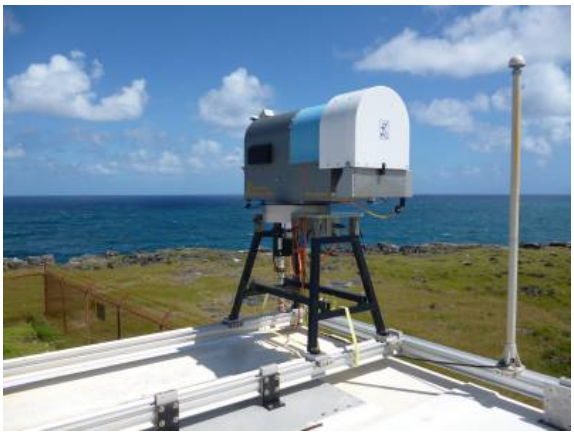

Figure 1. *Microwave radiometer in Barbados (Lev 2016)*

The temperature in equation 3 is called *brightness temperature* (Skou & Le Vine 2006), and labeled T_B. This is the measured quantity by the microwave radiometer. For a black body, the brightness temperature equals the actual temperature. For a gray body, with emissivity ε the relationship between the actual temperature and the brightness temperature is

$$T_b = \varepsilon T. \tag{4}$$

The data measured at different frequencies with MWR allows the determination of different properties such as temperature and humidity (Guiraud *et al.* 1979). The advantages of MWRs include their high temporal resolution (1 s to 3 s, (Barrera-Verdejo *et al.* 2016)) and robustness and they can provide continuous, automated measurements which are important for many numerical weather prediction models. With MRWs it is possible to measure throughout the troposphere, and also through clouds (Schroeder *et al.* 2015). However precipitable clouds pose difficulties even for MWRs (Barrera-Verdejo *et al.* 2016) and the vertical resolutions of MWR is rather poor (0.1 km to 1 km, (Rose *et al.* 2005)). The uncertainty in the measured temperature varies between 0.3 K and 3 K, depending on the calibration method (Maschwitz *et al.* 2013). For the humidity measurements, Massaro *et al.* (2015) concluded that the uncertainty in the absolute humidity can vary from 0.9 $\mathrm{g\,m^{-3}}$ at altitudes below 500 m to 0.01 $\mathrm{g\,m^{-3}}$ at the top of the troposphere.

MWRs can be be operated from ground level (such as the one in picture 1), but they are also used on the satellites for measuring the temperature of the atmosphere (Spencer *et al.* 1990) and oceans (Wentz *et al.* 2000).

2.2 LiDAR

Lidar (Light detection and ranging) instruments use optical frequencies of electromagnetic waves to detect aerosol particles suspended in the atmosphere. There are multiple different lidar systems implemented for different purposes, but the common aspect of all of these instruments is that they use laser light, typically between 355 nm - 1064 nm. The atmosphere is irradiated with said laser and the backscattered light from aerosols and

molecules is measured using a telescope. Low-power lidars are often called ceilometers, and have been used for detection of the cloud base height for a long time (Illingworth *et al.* 2015).

In lidar systems the received power by the telescope and the power of the laser are related by the lidar equation (Wandinger 2005):

$$P_r = P_l \frac{A}{r^2} O \mu \beta \exp(-2 \cdot \int_0^r \alpha(r')dr'), \tag{5}$$

where P_r is the received power by the telescope, P_l is the power of the equipped laser, A is the telescope area r is the scattering height, O is the overlap-function that depends on the setup between laser and the telescope, c is the speed of light, μ is a constant depending on efficiency of the receiving system, β is the backscattering coefficient and α is the extinction coefficient of the atmosphere. As it is evident from equation 5, there are two unknown properties dependent on the atmospheric conditions: the backscattering coefficient β and the extinction coefficient α. As it is impossible solve one equation with two unknown variables, an approximation has to be made. Usually the approximated variable is the ratio of backscattering and extinction coefficients, so called lidar ratio (sometimes denoted L) $S = \frac{\alpha}{\beta}$ (Fernald *et al.* 1972). This approximation is needed to solve the equation when only one measured signal is available. The estimation of the lidar ratio unavoidably leads to error in the calculated extinction and backscattering coefficients, and thus the value chosen should be carefully considered. The overlap effect and the basic operating principle of lidar system is depicted in figure 2. The overlap function is denoted with O. The overlap function is caused by the cone of the laser pulse being aligned along a different axis than the cone of the receiving telescope, and thus the light scattered at lower altitudes can not reach the telescope (Halldórsson & Langerholc 1978). This can severly limit the availability of the lidar data in the lower altitudes. Depending on the system, the availability of usable data can begin from 500 m (Barrera-Verdejo *et al.* 2016) to 1 km (Wandinger & Ansmann 2002), and with near-field optics this can be reduced to approximately 120 m (Engelmann *et al.* 2016). For ceilometers the overlap function may be sufficient already at the height of 30 m (Münkel *et al.* 2010).

Newer lidar system are also capable of detecting the Raman scattering from molecules in the atmosphere. This allows calculation of of backscattering coefficient and extinction coefficient separately as there are two different signals allowing calculation. Thus no approximation of lidar ratio is needed. However, this technique has its drawbacks, when strong background signal can cover the relatively weak signal from the Raman scattering. Generally Raman measurements are possible during the nigh-time measurements when the background signal is much lower. However, this allows more accurate prediction of lidar ratio to be used for retrievals for the day time measurements.

Using the Raman scattering, measurement of the atmospheric temperature profile is possible (Strauch *et al.* (1971), Balin *et al.* (2004), Fraczek *et al.* (2012)). Certain Raman lidars are also capable of humidity (Balin *et al.* 2004) and pressure (Fraczek *et al.* 2012)

measurements. For the temperature measurements the statistical error for Raman lidar according to Balin *et al.* (2004) is dependent on the altitude of the measured signal, ranging from around 0.5 K for altitudes below 9.5 km to 1.5 K at the top of troposphere and 4.5 K at around 20 km. On the other hand, Fraczek *et al.* (2012) found the temperature uncertainty to be less than 0.6 K in clear air and less than 1.4 K inside cloud. For humidity measurements the uncertainties were not given.

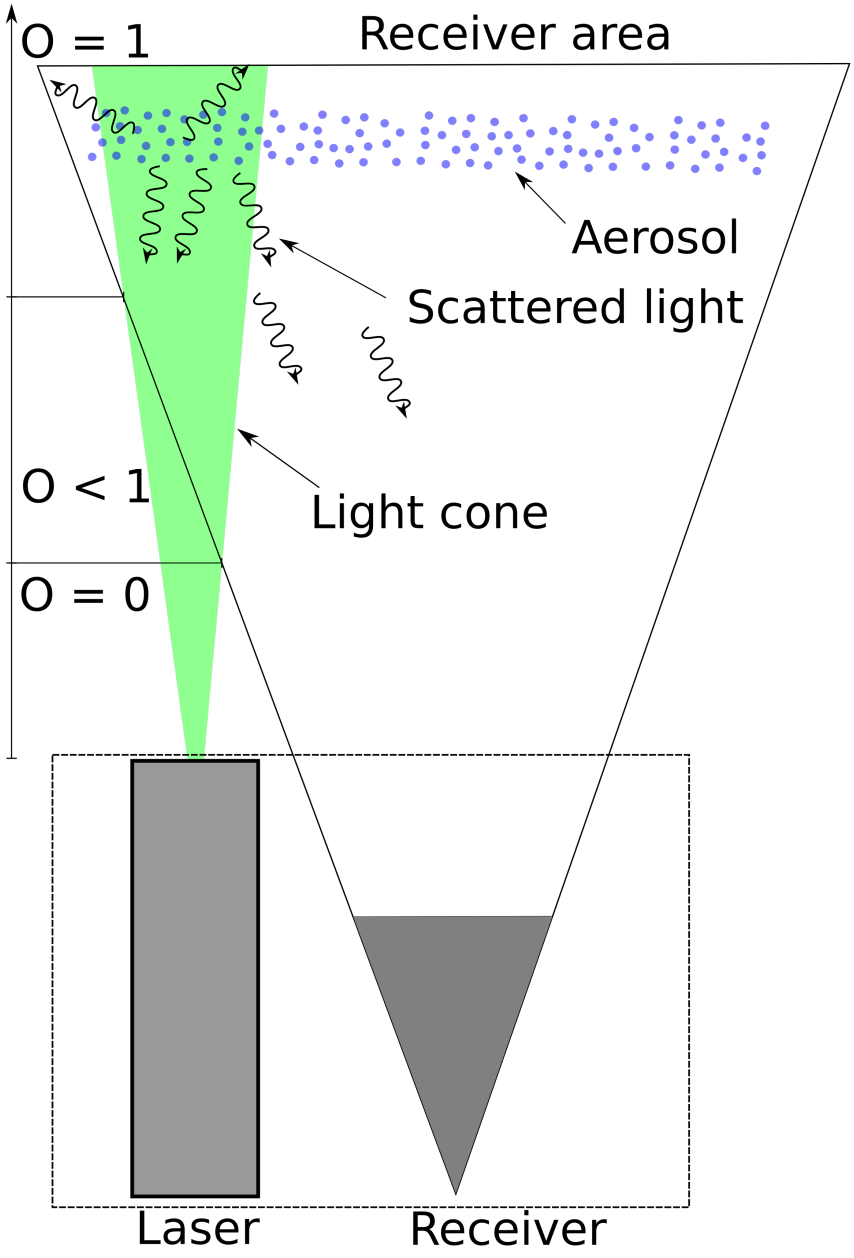

Figure 2. *The basic principle of a lidar system. The emitted laser pulse is scattered from the molecules and aerosol in the atmosphere, and the scattered light is detected using a receiver. The figure also depicts the overlap effect (denoted with O). At lower altitudes this function is 0, in the mid altitudes between 0 and 1 and finally reaching 1 at higher altitudes.*

When the laser pulse scatters from the small particles in the atmosphere, a small shift in

the frequency of the scattered laser happens when the scatterer moves with respect to the emitted laser. This is called the doppler shift, and it can be used to determine the wind speed by determining the velocities of the scattering particles (Chanin *et al.* 1989). The lidar systems taking advantage of this effect are called doppler lidars. These lidars are used for wind measurements throught the atmosphere.

Lidars can provide robust and automated vertical profiles of the atmospheric backscattering and extinction. However the overlap effect limits the usability of the data near ground, and the laser pulse can not penetrate clouds, thus limiting the measurement altitude during cloud presence.

2.3 Radiosondes

Radiosondes observations are probably the most well known of the atmospheric measurements. Tethered to a weather balloon which reach can an altitude of 53 km (Yoshitaka *et al.* 2003), radiosondes are important and widely used tools for profile measurements of the atmosphere. Radiosondes are commonly used for operational weather forecasting, but they also provide valuable in-situ data for climate research. Daily there are around 1000 soundings conducted around the world (Dirksen *et al.* 2014).

Radiosondes are mainly used for profile measurements of temperature and humidity, but they have also been utilized for aerosol measurements in the stratosphere (Hofmann *et al.* 1975). They also form the backbone for the Global Climate Observing System Reference Upper-Air Network (GRUAN), which utilizes radiosondes and satellite observations to create a long-term reference-quality data records. In addition, by using a radar to track the position of the radiosonde, measurement of the winds is also possible. Sometimes radiosondes with wind measurements capabilities are referred to as rawinsonde (*ra*dar*wi*ndsonde)

On a radiosonde the sensor is attached to a radio transmitter, which uses radio frequencies to transmit the data to the ground station. This is attached to a weather balloon with a nylon wire approximately 60 m long, in order to minimize the effect of the balloon on the ambient temperature and humidity. In addition to the payload and the balloon, the flight train consists of a parachute, deployed after the balloon bursts to ensure a safe landing of the payload and an unwinder to unwind the nylon string after launch. The balloon can weight between 0.3 kg to 1.2 kg and the ascend rate is around $5\,\mathrm{m\,s^{-1}}$. The gas inside the balloon is usually hydrogen, although helium or natural gases are also used. (Dabberdt *et al.* 2003). The different parts of the weather balloon flight train can be seen in figure 3.

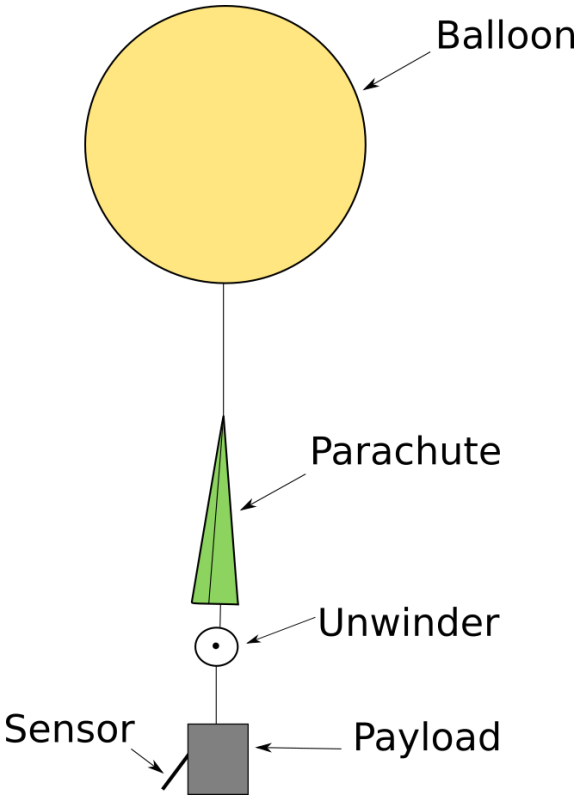

Figure 3. *Different parts of the a weather balloon flight train*

The transmitter unit transmits the data to the ground station for data collection. It also includes a GPS chip for the positioning of the radiosonde. The altitude of the balloon can be calculated either from the measured pressure or the GPS. Usually pressure is used at lower altitudes, but at higher altitudes the uncertainty of the GPS is lower than the height calculated from the pressure and thus at higher altitude GPS is used. Dirksen *et al.* (2014) found out that for Vaisala RS92 radiosonde the pressure uncertainty exceeds the GPS at around 15 km altitude.

2.4 Unmanned aerial vehicles

In addition to weather balloons, unmanned aerial vehicles (UAVs) have been used as a sensor platform for atmospheric measurements. While fixed-wing UAVs have been more common for meteorological profiling, lately multicopters have also been used as a platform for meteorological as well as aerosol measurements. The advantage of UAVs in atmospheric measurements is that they are generally cheaper compared to radiosoundings, and the reusability of the sensors makes it also possible to use more expensive sensors that on the radiosondes would be too costly. The drone used in this study is a multicopter, and more detailed description of the measurement setup is given in section 3.1. In addition, both radiosondes and UAVs require different sensors for the measurement of temperature, humidity and pressure. An overview of different sensor types is given in the next section.

2.5 Sensors

There exist multiple different sensor configurations for measuring temperature, humidity and pressure. The most common sensor for temperature, humidity and pressure measurements are presented here. In addition at the end aspects that should be considered when taking measurements are discussed.

2.5.1 Temperature sensors

Temperature sensors have to respond to the changes in ambient temperature. The first temperature measurement devices relied on the thermal expansion of liquids or metals. A traditional thermometer is filled with liquid, commonly mercury, which expands when the temperature rises and contract when it lowers. This change in the volume allows the detection of changes in temperature. These thermometers are called liquid-in-glass thermometers, and they can have an accuracy of 0.02 °C (Swindells & States. 1958). Another traditional thermometer uses two different types of metals with different thermal expansion coefficients. When the temperature changes, other block of metal will expand or contract more than the other, causing the joined block of metal to twist as the temperature changes.

However, more sophisticated and accurate thermometers rely on electrical sensors, where the change in temperature generally causes a change in the resistance or voltage, which can be measured. This change can then be used to calculate the change in the temperature.

There are mainly three types of different temperature sensors in use: Resistor temperature detectors (RTD), negative temperature coefficient (NTC) detectors and thermocouples.

Resistor temperature detectors

Resistor temperature detectors are generally made out of metal, and rely on the property that the conductivity is inversely proportional to the temperature. This is explained by the Drude-model, developed by Paul Drude (Drude 1900), which relates the conductivity to the temperature as follows:

$$\sigma = \frac{ne^2ul}{4k_bT}, \tag{6}$$

where σ is the conductivity of the metal, n is the number of atoms in a cubic centimeter, e is the elementary charge, u is the velocity of the electrons in the metal, l is the mean free path for the electron, k_b is the Boltzmann constant and T is the temperature. The Drude-model assumes that electrons in the metal act like a gas, carrying the electrical current as they move through the metal when an electric field is applied. While moving through the gas they collide with the atoms of the metal, slowing down their movement and reducing the conductivity. The mean free path l describes the average distance an electron can travel between the collisions. Because the resistance R is the inverse of the

conductivity σ, increase in temperature also causes increase in resistance as per equation 6.

When investigating the temperature dependance of the resistance, it is useful to consider a small change in temperature dT which leads to small fractional change in resistance R:

$$\frac{dR}{R} = \alpha dT, \tag{7}$$

where $\frac{dR}{R}$ is the change in resistance, dT is the change in temperature and α is a temperature coefficient that determines the change in resistance with change in temperature (Law & Rennie 2015). If α does not change significantly with temperature, equation 7 can be written

$$R_1 - R_0 = \alpha(T_1 - T_0)R_0, \tag{8}$$

where the R_1 and T_1 are the new resistance and temperature and R_0 andT_0 are the original resistance and temperature. This equation can be inverted to give the temperature T_1:

$$T_1 = \frac{R_1 - R_0}{\alpha R_0} + T_0. \tag{9}$$

The equation can be used to determine the temperature T_1 when the resistance R_1 is measured and if the resistance R_0 at temperature T_0 and temperature coefficient α are known. The temperature coefficient can be determined by measuring the resistance at, for example 0° C and 100° C. The relationship in equation 9 only holds true if the relationship between resistance and temperature is linear; in practice this is not always the case, especially in wider temperature ranges.

The material of the sensor determines the response of the resistance to the changes in temperature. While for example copper follows equation 8 well within all practical temperatures (Dellinger 1911), some materials require higher-order terms to accurately determine the response. A commonly used material in RTDs is platinum, which generally requires a cubic function. This is called the Callendar-Van Dusen equation (Fernicola & Iacomini 2008), and it is of the form

$$R(T) = R(T_0)[1 + A \cdot T + B \cdot T^2 + (T - 100)C \cdot T^3], \tag{10}$$

where $R(T)$ is resistance at temperature T, $R(T_0)$ is the resistance at temperature T_0 and A, B and C are experimentally determined constants. While this equation holds for temperatures from around $-200\,^\circ$C to $660\,^\circ$C, a simplified version can be used for temperatures between $0\,^\circ$C and $660\,^\circ$C (Yang *et al.* 2015):

$$R(T) = R(T_0)[1 + A \cdot T + B \cdot T^2]. \tag{11}$$

Other widely used materials for RTDs are gold, nickel and silver (Childs *et al.* 2000). The chose material depends on the application. Platinum is a common choice in RTDs for its high accuracy and platinum resistance temperature detectors (PRTDs) are used for

defining the international temperature scale (Preston-Thomas 1990). In order to manufacture PRTDs accurate enough for this purpose, it is important to ensure that they are strain free. Strains in the sensor will decrease its accuracy and thus industrially used sensors are less accurate. Keeping the sensor strain-free is often impossible, practically limiting the accuracy between 0.01 °C to 0.2 °C (Hashemian & Petersen (1992), see Childs *et al.* (2000)). It is also noteworthy that for high accuracy a cubic formula for the relationship between temperature and resistance is insufficient, requiring as high as 15^{th} order formula (Preston-Thomas 1990). However, for smaller temperature ranges even linear formula can keep the error below 0.4 °C at 50 °C (Childs *et al.* 2000).

Resistance detector thermometers are used in application when high accuracy and long time stability is required. However, compared to thermocouples their measurement range is limited and the response time is longer. A platinum resistance detector is used in the Vaisala RD41 dropsonde used for the measurements in this study.

Negative temperature coefficient detector

Negative temperature coefficient (NTC) sensors, also called thermistors, are made out of semiconductors. For semiconductors the resistance decreases with increasing temperature, thus the temperature coefficient is negative. This behaviour relates to the way semiconductors operate. The current is carried at the conduction band, which in semiconductors is separated from the valence band by small energy difference. In order for the electrons to get to the conduction band they need to overcome this energy difference. This energy can be provided by an electric field, but also the thermal energy of the electrons can provide enough energy. Thus an increase in temperature lowers the additional energy needed and the resistivity is decreased. The equation relating temperature and resistivity is (Steinhart & Hart 1968)

$$\rho^{-1} = F(T)\exp -\Delta E/2k_B T, \tag{12}$$

where $F(T)$ is a function of temperature, ΔE is the energy difference between the valence band and the conduction band, k_B is the Boltzmann constant and T is the temperature. While this equation in principle relates the resistivity to the temperature, an experimental curve has been fitted for semiconductors. This is the Steinhart-Hart equation (Steinhart & Hart 1968) and has the form

$$T^{-1} = A + B\log(R) + C(\log(R))^3, \tag{13}$$

where R is the resistance and A, B and C are constants that have to be experimentally derived for each sensor. NTC sensors are used because of their cheap price and high accuracy. However they are only usable on limited temperature range. For this reason they are generally used in biomedical applications where the accuracy is preferred over capability to measure temperature over wide range.

Thermocouples

Thermocouples are based on the Seebeck effect (Goldsmid 2016). The Seebeck effects causes current in a circuit made of two dissimilar metals, when one of the junctions is kept at warmer temperature than the other. The temperature gradient between the junctions causes a thermoelectric potential on the wires. When the wires are made out of different metals there is a potential difference between the wires, and thus a current is generated. Another possibility for thermocouple is to keep the other junction open, when the voltage difference between the wires can be measured. This voltage difference is proportional to the temperature difference between the ends of the wires, so if the temperature and the voltage difference at the open end is known, the temperature at the other junction can be calculated (Goldsmid 2016):

$$\Delta T = \frac{V}{\alpha_{AB}}, \tag{14}$$

where ΔT is the temperature difference, V is the measured voltage and α_{AB} is the differential Seebeck coefficient. This forms the basis for thermocouples. The principle of operation for thermocouples in illustrated in figure 4. When the junction w_1 is placed into warmer temperature than the ends c_1 and c_2, a voltage forms between the ends c_1 and c_2. Usually the cold junction is kept at a reference temperature.

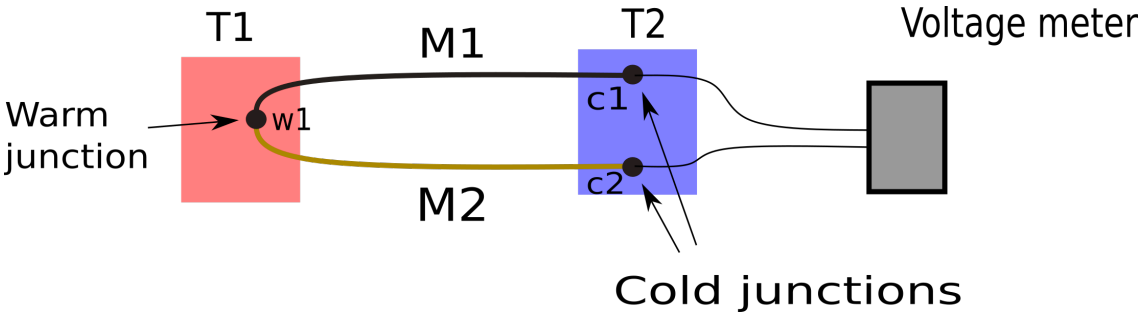

Figure 4. *Principle of operation of a thermocouple*

Thermocouples can be used when high temperature range (for thermocouples the range can be $-213\,^{\circ}\mathrm{C}$ to $1000\,^{\circ}\mathrm{C}$) or robustness is needed (Fontes 2005).

2.5.2 Humidity sensors

Humidity, which is defined as the amount of water vapour in air, can be characterized by three different units: Relative humidity, absolute humidity and specific humidity. The absolute humidity is the mass of the water vapour carried in certain mass of dry air. Absolute humidity is expressed in units $\mathrm{g\,kg^{-1}}$. If assuming ideal gas, absolute humidity can be calculated from equation

$$H = \frac{M_w p}{M_a (P - p)}, \tag{15}$$

where M_w is the molar mass of water, M_a is the molar mass of air, p is the partial pressure of water vapour, P is the total pressure. The relative humidity RH is the fraction of water

vapor pressure in air to the water equilibrium vapor pressure:

$$RH = 100\frac{p}{p_s}, \tag{16}$$

where p_s is the water equilibrium vapor pressure. (Moyers & Baldwin 1999). Specific humidity is the mass of water vapour per unit mass of moist air, expressed in $\mathrm{g\,kg^{-1}}$ (Allaby 2013). Dew point temperature is also related to the humidity. Specifically, it is the temperature at which water vapour starts to condensate given the humidity and the ambient temperature. The dew point temperature in degrees Celsius can be approximated with

$$t_d = t\left[1 - \frac{(t+273.15)\ln\frac{RH}{100}}{L/R_w}\right]^{-1}, \tag{17}$$

where L is the enthalpy of vaporization and R_w is the gas constant for water vapour (Lawrence 2005).

For the measurement of humidity, different types of sensor have been implemented. One commonly used sensor uses thin-film polymer between electrodes, essentially forming a capacitor. The polymer is acting as the dielectric material between the electrodes and the capacitance is thus proportional to the dielectric constant of the polymer. When the polymer absorbs the water vapour from the air, the dielectric constant changes and this change can be used to determine the relative humidity. While the relative permittivity for a polymer ranges from 3 to 6, for water vapour it is around 7800 at 25 °C. Thus, even a small amount of absorbed water vapor can be detected. The capacitance for such a sensor can range from 45 pF to 70 pF. (Yamazoe & Shimizu 1986). Absorption of the water occurs when the water molecules form bonds with the polymer. The relationship between the relative number of bonds and the relative humidity is (Salasmaa & Kostamo 1986)

$$\theta = \frac{\frac{RaP_0}{b'(2\pi mkT)^{1/2}} \cdot e^{(q(\theta)-q_0)/kT}}{1 + \frac{RaP_0}{b'(2\pi mkT)^{1/2}} \cdot \exp(q(\theta) - q_0/kT)}, \tag{18}$$

where R is the relative humidity, a is the effective area of a bonding site, P_0 is the partial pressure of water vapor, $q(\theta)$ is the binding energy of a water molecule in polymer, q_0 is the binding energy of water molecule in water, b' is the probability of emission of water molecules, k is the Boltzmann constant and T is the absolute temperature. The Vaisala Humicap® sensor is based on this technology (Salasmaa & Kostamo 1986), and this sensor is used in the dropsonde used in the measurements. The configuration for this sensor can be seen in figure 5.

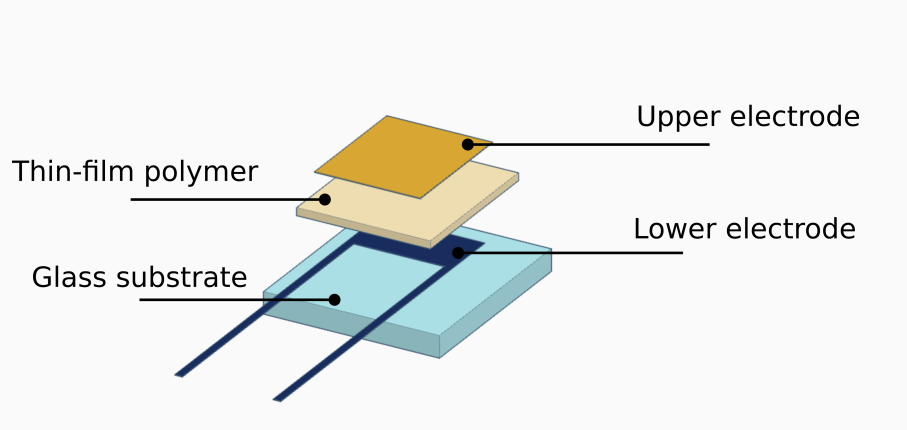

Figure 5. *Configuration of a Vaisala Humicap humidity sensor. Adapted from (Yamazoe & Shimizu 1986)*

Another type of humidity sensor is based on the resistance. A resistance humidity sensor is based on polymer. Thin-film polymers are crosslinked, and when the material adsorbs water the resistance increases. This leads to lower resistance in air that is more humid, and this relationship between resistance and humidity allows the measurement of relative humidity. The resistance humidity sensor can have an accuracy of 3 %, and can be coated with protective coating to make it resistant against cigarette smoke and oil (Hijikagawa *et al.* 1983).

A third type of humidity sensor is based on thermal conductivity. There are two NTC sensors in this setup, one is sealed in dry air and the other one is exposed to the ambient air. The difference in the resistances of these thermistors is directly proportional to the absolute humidity (Okcan & Akin 2004).

2.5.3 Pressure sensors

For the measurements of pressure, a capacitor can be used (Kubba *et al.* 2016). The capacitance of the capacitor can be expressed

$$C = \varepsilon \frac{A}{d}, \tag{19}$$

where ε is the electric constant, A is the size of the plates and d is the distance of the plates. In a pressure sensor, one plate is rigid and one plate is flexible to allow movement when the pressure changes. With the changing pressure, the flexible plate moves closer or farther away from the rigid plate, changing the distance d and thus changing the capacitance. This change can be measured, allowing the detection of the change in pressure.

In atmospheric measurements, the altitude is often calculated from the measured pressure. The change in pressure is related to the change in height by the hydrostatic equation (Atkins & Escudier 2013) which has the form

$$\frac{dp}{dh} = -\rho g, \tag{20}$$

where p is the pressure, h is the height, ρ is the air density and g is the gravitational acceleration. The air density ρ can be replaced by $\frac{P}{R_a T}$, where R_a is the gas constant for air and T is the temperature. This is stated by ideal gas law, and $R_a = \frac{R}{M_a}$ where R is the gas constant and M_a is the molar mass of air. After this replacement the equation 20 can be separated:

$$dh = -\frac{R_a T}{g}\frac{dp}{P}, \tag{21}$$

and if the temperature T is assumed to be constant, which especially in the lower atmosphere is a reasonable assumption, the equation 21 is an ordinary first-order differential equation and can be solved by integration:

$$\int_0^H dh = \int_{P_0}^P -\frac{R_a T}{g}\frac{dp}{P}, \tag{22}$$

which after solving the integral becomes

$$H = -\frac{R_a T}{g}\ln\frac{P}{P_0}, \tag{23}$$

where P_0 is the pressure at ground level. The equation 23 is often called the hypsometric equation (Wallace & Hobbs 2006) and it can be used to calculate the height if the pressure P is measured and the pressure P_0 is known. However, this only works in the lower part of the atmosphere where the temperature can be assumed to be constant.

2.5.4 Measurement considerations

When measuring fluid temperature with an electric sensor, careful consideration must be placed in interpretation of the results. Often, the fluid temperature is assumed to be the temperature measured by the sensor: however this is not always a reasonable approximation. When measuring temperature with a sensor that is placed into the medium, it affects the temperature of the fluid around it and the actual temperature measured is the temperature of the sensor. Under different conditions this temperature can be significantly different from the true temperature of the fluid and depending on the application and the accuracy required this can lead to incorrect results. The sensor changes its temperature depending on its mass m, specific heat capacity c and added heat Q, following the equation

$$mc\Delta T = Q, \tag{24}$$

where ΔT is the change in temperature. In order to determine how the temperature changes with time, the equation 24 can be derived with respect to time to yield

$$mc\frac{dT}{dt} = \dot{Q}, \tag{25}$$

where $\dot{Q}$ is the time derivative of the heat added to the sensor. This variable includes all the sources and sinks of heat. These sources are indentified by Luers (1990). For a sensor placed in the atmosphere, heat sources would be the absorbed solar radiation, absorbed

terrestrial radiation, and in case of sensors that require a current flow through the sensor, the heat caused be this current. Heat sink would be the emitted radiation of the sensor. In addition, heat will be transferred through convection from the sensor to the air around it and conducted along the wires of the circuit. These depend on the temperature differences and can be either sinks or sources. Plugging in all of these terms into equation 25 yields

$$mc\frac{dT}{dt} = \dot{q}_{abs} - \dot{q}_{em} + \dot{q}_{conv} - \dot{q}_{cond} + \dot{q}_{el}, \tag{26}$$

where q_{abs} is the absorbed radiation by the sensor, q_{em} is the emitted radiation of the sensor, q_{conv} is the heat transferred through convection, q_{cond} is the heat transferred through conduction and q_{el} is the heat caused by the electric current in the sensor. The dot above each q refers to the time derivative of each variable. When the sensor is in heat balance with its surroundings, the term $\frac{dT}{dt}$ in equation 26 is equal to 0 and the left-hand side of said equation can be neglected. Thus all the heat sources and sinks balance each other out. In order to relate this to the ambient temperature and the sensor temperature, the convection term is in a key role. The convection of heat from a solid to a fluid can be expressed using Newton's law for cooling

$$\dot{q}_{conv} = -A \cdot h_c(T_s - T_\infty), \tag{27}$$

where A is the total area of the solid (in this case the sensor), h_c is the convective heat transfer coefficient, T_s is the sensor temperature and T_∞ is the ambient temperature. Plugging this relationship into equation 26 and setting $\frac{dT}{dt} = 0$, yields

$$\dot{q}_{abs} - \dot{q}_{em} - Ah_c(T_s - T_\infty) - \dot{q}_{cond} + \dot{q}_{el} = 0 \tag{28}$$

and after rearranging the terms, the expression for the temperature difference between the sensor T_s and ambient air T_∞ can be expressed as

$$T_s - T_\infty = \frac{\dot{q}_{abs} - \dot{q}_{em} - \dot{q}_{cond} + \dot{q}_{el}}{Ah_c}. \tag{29}$$

From the equation 29 it is easy to see that T_s and T_∞ are equal only if all the heat sinks and sources are either 0 or balance each other out. In practice this is not the case and thus a temperature difference will always remain between the sensor and the ambient air. However, some steps can be taken in order to minimize this effect to the point it can be neglected. For the absorption and emission, the sensor can be coated in order to reduce the interaction with radiation. The electrical current can be minimized by using small voltage and the convection coefficient can be maximized in order to increase the convection from the sensor to the ambient air. The convection coefficient h_c depends on the airflow velocity around the sensor. This relationship arises from the convective heat transfer coefficient's relationship to the Nusselt number (Herwig 2016),

$$h_c = \frac{kNu}{L}, \tag{30}$$

where k is the conductive heat transfer coefficient, Nu is the Nusselt number and l is the characteristic length for the sensor. The Nusselt number in turn is related to the Reynolds number with

$$Nu = 0.184 + 0.324Re^{0.5} + 0.291Re^{m}, \tag{31}$$

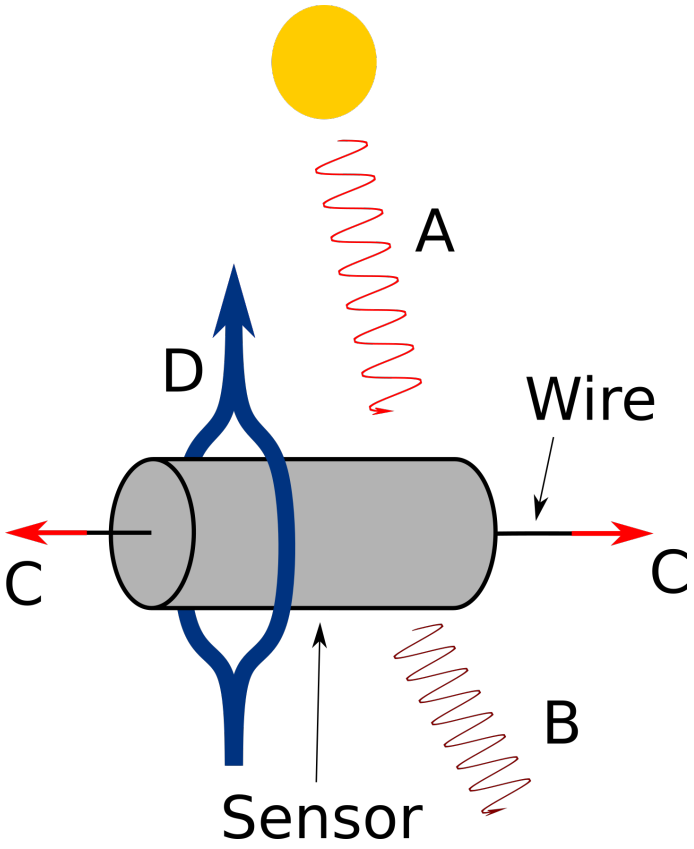

Figure 6. *The different effects that influence the heat balance of the sensor. A is the solar radiation, B is the emitted radiation, C is the heat conducted along the wires and D is the convection. In addition the electrical current warms the sensor which is not drawn here. Figure adapted from Luers (1990)*

where Re is the Reynolds number and $m = 0.247 + 0.0407 Re^{-0.168}$. The Reynolds number characterices the flow patterns in a fluid, and it is the ratio of inertial forces and the viscous forces (Reynolds 1883)

$$Re = \frac{uL}{\nu}, \tag{32}$$

where u is the air (or fluid) flow velocity, L is the characteristic length and ν is the kinematic viscosity. It is rather easy to see from equation 30, 31 and 32 that h_c is proportional to the air flow velocity u. Thus, with higher air flow speed around the sensor the convection coefficient h_c is higher and the temperature difference $T_s - T_\infty$ is smaller. A visualization of the different effects, excluding the electrical current, can be seen in figure 6.

The difference in temperature is often referred to as "radiation error" due to the biggest contributor to equation 29 usually being the solar radiation term $\dot{q}_{abs}$. This difference depends on the sensor geometry, and for the temperature sensor on Vaisala RS92 radiosonde this error can range from practically 0 at wind speed of 20 $\mathrm{m\,s^{-1}}$ and pressure of 1000 hPa to around 1.9 K at wind speed of 1 $\mathrm{m\,s^{-1}}$ and pressure of 15 hPa (Dirksen *et al.* 2014).

Equation 29 assumes that the sensor is at heat balance with the environment. However

when temperature changes the sensor takes certain time to respond to this change. This time is characterized by the response time of the sensor. Combining and rearranging the equations 26 and 27 yields

$$-\frac{mc}{Ah_c}\frac{dT}{dt} = (T_s(t) - T_\infty) + \dot{q}_{abs} - \dot{q}_{em} - \dot{q}_{cond} + \dot{q}_{el}. \tag{33}$$

Assuming that the only heat exchange is through convection, this equation becomes

$$-\frac{mc}{Ah_c}\frac{dT}{dt} = (T_s(t) - T_\infty), \tag{34}$$

and furthermore, by setting $\frac{mc}{Ah_c} = \tau$ and $(T_s(t) - T_\infty) = \Delta T(t)$ the equation becomes

$$-\tau\frac{dT}{dt} = \Delta T(t). \tag{35}$$

This equation is a first-order linear time invariant system and is satisfied by

$$\Delta T(t) = \Delta T_0 e^{-t/\tau}, \tag{36}$$

where t is the elapsed time, ΔT_0 is the temperature difference at $t = 0$ and τ is the response time of the sensor. Equation 36 indicates that when $t = \tau$ the temperature difference has decreased to $\frac{1}{e}$ of the original value. Thus the response time of the sensor tells how fast the sensor reacts to changes in ambient temperature. Sensors with lower response time are generally preferred. The response time of the sensor leads to time lag in case of strong temperature gradients, when the sensor cannot keep up with the fast changes of the temperature. This leads to the loss of these temperature spikes in the measured profiles.

For humidity sensors a temperature correction also has to be applied. When measuring the humidity, the actual measured value is the humidity inside the sensor. This can differ from the ambient humidity value due to different temperature inside the sensor, causing the saturation vapour pressure at the sensor to differ from the ambient value. The humidity can be corrected using equation (Dirksen *et al.* 2014)

$$RH_c = RH_m\frac{p_s(T + f\Delta T)}{p_s(T)}, \tag{37}$$

where RH_c is the correct humidity, RH_m is the measured humidity, $p_s(T)$ is the saturation vapour pressure at temperature T, T is the actual ambient temperature, ΔT is the temperature difference between the air and sensor that can be calculated using equation 29 and f is an experimentally derived sensitivity factor for the humidity sensor. Thus the difference between the measured humidity and the actual humidity depends on the temperature difference between the humidity sensor and the ambient temperature. Equation 37 estimates the humidity sensor temperature $(T + f\Delta T)$ using the same radiation correction that can be used for the temperature sensor. The saturation vapour pressure p_s at temperature t can be estimated using the experimentally derived equation

$$p_s = \frac{\exp 34.494 - \frac{4924.99}{t+273.1}}{(t+105)^{1.57}}, \tag{38}$$

where t is the temperature in degrees Celsius. This equation was derived by Huang (2018).

Similarly to the temperature sensors, the humidity sensors also suffer from the time lag caused by the response time of the sensor. Often the response times of the humidity sensors are higher than the temperature sensors, and especially in the upper atmosphere can smooth the profiles significantly (Dirksen *et al.* 2014).

3. METHODS AND MEASUREMENT SETUP

In this chapter the methods used for data analysis, the description of the measurement site and setup and the methods used for the corrections of temperature and humidity are presented.

3.1 Measurement setup

The measurements were made using a DJI Matrise 600 pro drone which has 8 rotors, maximum ascend speed of $5\,\mathrm{m\,s^{-1}}$ and maximum descend speed of $3\,\mathrm{m\,s^{-1}}$. The diagonal wheelbase of the drone is 1133 mm and dimensions 1668 mm x 1518 mm x 727 mm. The drone is capable of climbing up to 2500 m above sea level (ASL), but during this campaign the maximum height reached was approximately 450 m above ground level (AGL), corresponding to 554 m above sea level. The autonomous operation of the drone was made possible by custom build ground station, which takes care of the battery replacement between flights. The drone and the ground station were provided by a company called Rumble tools and can be seen in figure 7. The measurement instruments were located underneath the drone. For measurements the vertical velocity in the ascend leg was approximately $3\,\mathrm{m\,s^{-1}}$ and in the descend leg approximately $1\,\mathrm{m\,s^{-1}}$. This leads to a ascend time of around 150 s and descend time of around 450 s, and total flight time of around 10 min.

For measurements the drone was equipped with a Vaisala RD41 dropsonde that can be

Figure 7. *Rumble tools DJI Matrise pro drone inside the ground station.*

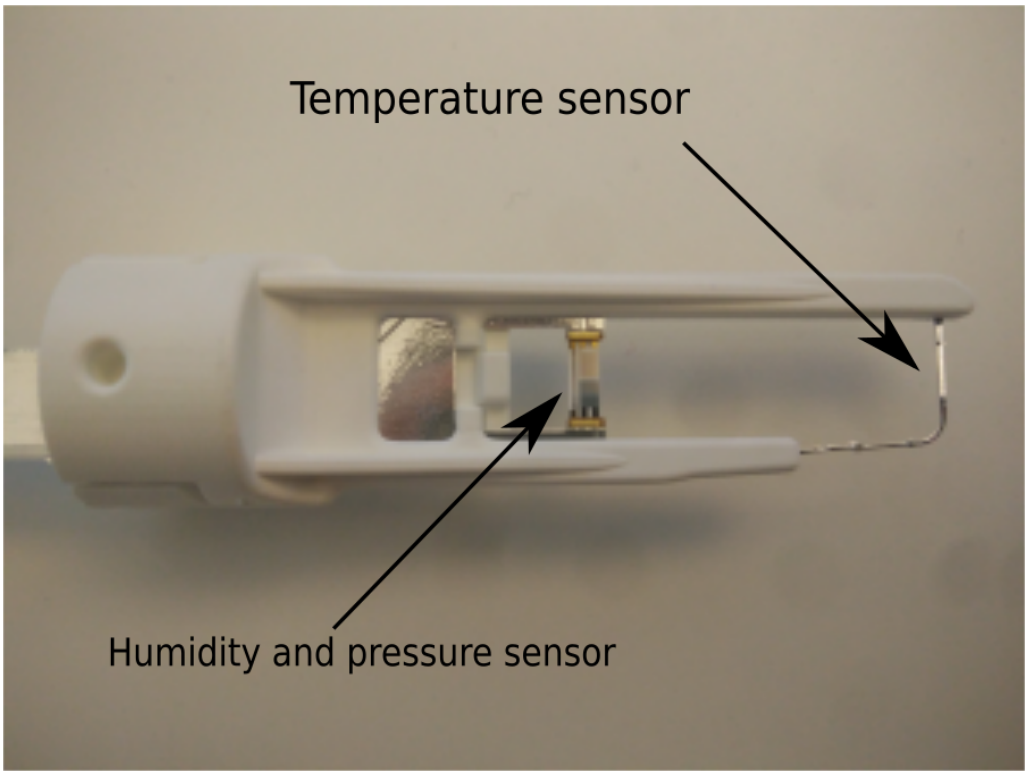

Figure 8. *Vaisala RD41 dropsonde sensor. The temperature sensor is the thin wire at the bottom and humidity and pressure sensor are attached to the slide above temperature sensor.*

seen in figure 8. The sonde has a platinum resistor sensor for temperature measurements, thin-film capacitor for relative humidity measurement and a silicon capacitor for pressure measurements. In RD41 the humidity sensor is also capable of sensing the temperature of the sensor, which is needed for correct the measured relative humidity into the actual ambient relative humidity. The range, resolution, repeatability and response time for each sensor are presented in table 1, as given by Vaisala (2018).

	Temperature	Humidity	Pressure
Range	−90 °C to 60 °C	0 %RH to 100 %RH	Surface pressure to 3 hPa
Resolution	0.01 °C	0.1 %RH	0.01 hPa
Repeatability	0.1 °C	2 %RH	0.4 hPa
Response time	0.5 s	20 °C <0.3 s −40 °C <10 s	

Table 1. *Range, resolution, repeatability and response time for each sensor. The response time is given at ambient conditions of* $6\,\mathrm{m\,s^{-1}}$ *wind speed and* 1000 hPa*. For pressure sensor the response time is not given.*

Specifications given in table 1 are given at a wind speed of $6\,\mathrm{m\,s^{-1}}$ and at 1000 hPa. The repeatability is given as an expanded standard deviation from the mean, with confidence level k = 2 (Vaisala 2018). The response time for the pressure sensor was not specified. The response time for the humidity sensor depends on the sensor temperature, and for low temperatures the response time can be multiple seconds. For the measurements conducted

for this work this does not pose difficulties, but in lower temperatures, especially in the upper atmosphere high response time leads to smoothing of the humidity profiles which should be taken into account (Dirksen *et al.* 2014).

3.2 Measurement site description

Measurements for were made at measurement site in Jokioinen. The site is located in Southwest Finland at 60.8140°N, 23.49761°E; approximately 105 km northwest from Helsinki (see figure 9). The site is located 104 m ASL and has been operational since 1957. The area around the site is mainly clay ground fields, with only few to no wind obstacles. A satellite image of the measurement site can be seen in figure 10.

Figure 9. *Location of Jokioinen on map. Source: Google (2019a)*

The measurement site has measurement instruments for temperature, pressure, humidity, wind, solar radiation, snow depth, visibility, cloud bottom height and precipitation. In addition, radio soundings are conducted in Jokioinen four times a day, at 00:00, 06:00, 12:00 and 18:00 UTC

For the corrections described in section 3.4 wind speed and global solar irradiance measurements was required. The global irradiance is measured at ground level using a Delta-

Figure 10. *Satellite image of the measurement site. Source: Google (2019b)*

T Devices Ltd. pyranometer and the wind speed is measured at different heights using a Leosphere WindCube® v2 wind doppler lidar. The wind doppler lidar is capable of measuring the wind speed and direction at the heights of 40 m, 60 m, 70 m, 80 m, 90 m, 100 m, 110 m, 120 m, 130 m, 140 m, 150 m and 160 m.

3.3 Campaign

The measurement campaign was conducted at the site in Jokioinen, from 31.08.2018 until 12.09.2018. During this period, there were measurements taken on 8 days. In total 34 flights were performed, and for 12 flights a radiosonde reference was available. The measurements were taken daily between 08:00 and 16:00 (GMT+3).

3.4 Measurement corrections

As described in section 2.5.4, there are sources of uncertainty when measuring the ambient air temperature and humidity arising from the radiation. While an effort can be made to derive these effects theoretically (as done by Luers (1990)), sensor specific, experimentally derived corrections also exists. One such correction was derived by Dirksen *et al.* (2014) and it is of the form

$$\Delta T = a \cdot x^b \qquad \text{with } x = \frac{I_a}{pv}, \tag{39}$$

where I_a is the total solar irradiance, p is the air pressure, v is the ventilation speed at the sensor and a and b are constants. These constants were determined statistically for Vaisala RS92 radiosonde, but here we assume they are also applicable for the RD41 used in the drone. The constants are $a = 0.18(\pm 0.03)$ and $b = 0.55(\pm 0.06)$. The actinic flux (the total radiation flux integrated over a sphere that originates from the sun, accounts for the direct and the scattered radiation) on the sensor was available from solar radiance measurement on the Jokioinen measurement site and the pressure was measured by the dropsonde. The ventilation speed was approximated from the drone movement in vertical and horizontal direction and the wind speed measurements. The detailed description is in section 3.4.1. After the radiation correction has been determined, the actual ambient temperature T_a is

$$T_a = T_m - \Delta T, \tag{40}$$

where T_m is the measured temperature and ΔT is calculated with equation 39.

3.4.1 Ventilation speed estimation

For equation 39, an estimation of the ventilation speed at the sensor is needed. This ventilation speed can be estimated from the horizontal and vertical movements of the drone and the wind speed. Figure 11 visualizes this situation.

For the effect of the vertical velocity on the ventilation speed the location of the sensor has to be considered. During the ascending phase, the sensor is behind the drone with respect to the direction of velocity and thus shielded from the air flow by the drone itself. Thus the ventilation speed is lower at the sensor when compared to the descending phase. During the descend phase the sensor is located in front of the drone with respect to the direction of velocity, and thus the drone does not shield the sensor from the airflow. This effect is illustrated in the figure 11, where the streamlines in dark blue represent the approximate airflow when the drone is ascending and the streamlines in light blue represent the airflow when the drone is descending. However, these streamlines are only meant to approximately visualize the situation, and are not based on simulations or calculations. This difference was resolved by setting the flow speed to $0\,\mathrm{m\,s^{-1}}$ during ascend phase, and keeping it at the descend velocity during descending phase. It should be noted though that the actual airflow during ascend may not be exactly $0\,\mathrm{m\,s^{-1}}$. For detailed characterization of the flow at the sensor for different ascending velocities computer simulations or laboratory tests would be needed, which was not possible in the framework of this work.

Lastly, the wind speed at the sensor affects the ventilation. The wind speed was available from the measurements made by the windcube lidar. However from this instrument the wind speed was only available in altitudes between 40 m and 160 m; thus the wind speed correction was also applied only to this range. For the total ventilation the wind speed and the ground speed had to be considered. For this purpose the total ventilation was calculated in latitudinal and longitudinal components and from these the total horizontal

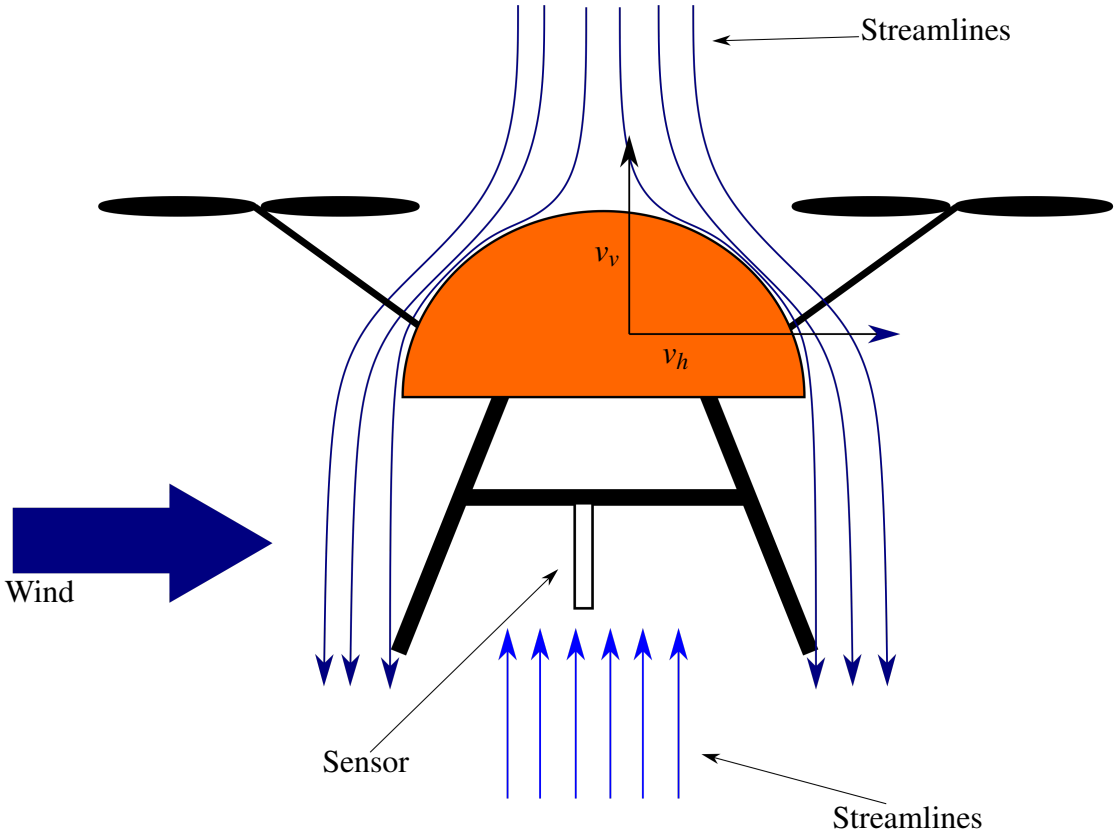

Figure 11. *Illustration of the different components affecting the ventilation at the sensor.*

ventilation speed was calculated using equation 41

$$v_h = \sqrt{(u_{lat} - v_{lat})^2 + (u_{lon} - v_{lon})^2}, \tag{41}$$

where v_h is the total horizontal ventilation speed, u is the wind speed, v is the horizontal velocity of the drone. Subscript lat refers to the latitudinal component and lon refers to the longitudinal component. The longitudinal and latitudinal components for wind speed are calculated from the wind speed and direction and for the drone velocity from the displacement in latitudinal and longitudinal direction.

Finally, the total ventilation speed was similarly calculated using equation

$$v = \sqrt{v_h^2 + v_v^2}, \tag{42}$$

where v is the total ventilation speed at the sensor, v_h was calculated using equation 41 and v_v is the vertical velocity of the drone. For the reasons mentioned above, during the ascend leg the vertical ventilation speed was set to 0. Then, for all of the measurements the horizontal and vertical speeds were calculated. In order to avoid errors caused by very low values for v, the value v_v for the equation 42 was taken to be the mean value from the

calculated vertical velocities. Then, the total ventilation speed v from the equation 42 is entered into the equation 39 in order to correct the effect of radiation on the sensor.

In case of multi-rotor drones the airflow caused by the rotors themselves is also a potential factor in the ventilation at the sensor. However characterization of this airflow also requires either modelling or laboratory testing and thus these effects are not being considered in the calculations.

3.4.2 Humidity correction

The measured humidity is corrected using the equation 37. However, since the humidity sensor on the used dropsonde has an integrated temperature sensor, no estimation for the humidity sensor temperature is needed. Thus the term $T + f\Delta T$ in equation 37 can be replaced with measured value T_h which is the humidity sensor temperature. Then the accuracy of the humidity measurements depends on how accurately the actual ambient temperature T can be measured, and the accuracy of the humidity sensor temperature T_h. Using these we get the equation for humidity correction

$$RH_c = RH_m \frac{p_s(T_h)}{p_s(T)}. \tag{43}$$

The saturation vapour pressures are calculated using equation 38.

3.5 Uncertainty estimation

All the corrections performed on the measured data causes further uncertainty that have to be taken into account in order to properly estimate the performance of the measurement setup. The total uncertainty budget consists of the uncertainty of the sensor itself and the uncertainties caused by the corrections.

While uncertainties can, in principle, be determined statistically from N independent measurements, in practice for atmospheric measurements this is impossible. In atmospheric measurements the consecutive measurements are always subject to spatial and temporal variations of the atmosphere itself, rendering purely statistical approach insufficient. In this case, a more detailed uncertainty analysis is required, using uncertainty propagation formula (Committee Guides Metrology 2008). It allows the estimation of total measurement uncertainty after corrections using the uncertainties of the input quantities. The total uncertainty is

$$u_t(X) = \sqrt{\sum_{i=1}^{N} \frac{\partial f(v_1, v_2 \dots v_N)}{\partial v_i}^2 u(v_i)^2}, \tag{44}$$

where u_t is the total uncertainty of variable X, f is the functional dependence of the variable X on the input variables v_i and $u(v_i)$ is the uncertainty of the i-th input variable. In some cases, evaluating the partial derivatives can be difficult in practice. For example

this can be the case for equations that are derived experimentally, such as the saturation pressure equation 38. Then the uncertainty can be evaluated numerically using equation:

$$u_t(X) = \frac{1}{2}\sqrt{\sum_{i=1}^{N}\{f(v_1, v_2, \ldots, v_i + u(v_i), \ldots, v_N) - f(v_1, v_2 \ldots, v_i - u(v_i), \ldots, v_N)\}^2}, \quad (45)$$

where the derivative in the equation 44 is replaced with the finite difference.

For determining the uncertainty in the measured temperature, the functional dependence of the temperature is expressed by equation 40. Combined with equation 39, the total uncertainty of the temperature can be determined using equation 44:

$$u_t(T) = \left\{ \left(\frac{\partial T}{\partial T_m}u(T_m)\right)^2 + \left(\frac{\partial T}{\partial a}u(a)\right)^2 + \left(\frac{\partial T}{\partial b}u(b)\right)^2 + \left(\frac{\partial T}{\partial I}u(I)\right)^2 + \left(\frac{\partial T}{\partial p}u(p)\right)^2 + \left(\frac{\partial T}{\partial b}u(v)\right)^2 \right\}^{\frac{1}{2}} \quad (46)$$

which, after solving the partial derivatives has the form

$$u_t(T) = \left\{ u(T_m)^2 + \left(\left(\frac{I}{pv}\right)^b \cdot u(a)\right)^2 + \left(a\frac{I}{pv}ln\left(\frac{I}{pv}\right)u(b)\right)^2 + \left(\frac{ba}{I}\right)\left(\frac{I}{pv}\right)^b u(I)\right)^2 + \left(\left(-\frac{ab}{p}\right)\left(\frac{I}{pv}\right)^b u(p)\right)^2 + \left(\left(-\frac{ab}{v}\right)\left(\frac{I}{pv}^b u(v)\right)^2 \right\}^{\frac{1}{2}}. \quad (47)$$

Using this equation with given input parameters the uncertainty can be calculated individually for each data point. The uncertainties used for the analysis are taken to be the uncertainties for each individual instrument as given by the manufacturer. For the Vaisala sensors these uncertainties are given in table 1. Since the uncertainties given are expanded with k = 2, the standard uncertainty used is this value divided by 2. For the temperature sensor, the uncertainty $u(T_m)$ is 0.05 °C and for the pressure sensor the uncertainty $u(p)$ is 0.2 hPa. The uncertainty of solar irradiance $u(I)$ is 3 % (Kipp & Zonen 2014). The uncertainties associated with the coefficients a ($u(a)$) and b ($u(b)$ are 0.03 and 0.06, respectively (Dirksen *et al.* 2014).

For the ventilation speed, the uncertainties arise from the uncertainty in the vertical and horizontal velocities and the uncertainty in wind speed. For wind speed, the uncertainty when measured with a radiosonde is $0.4\,\mathrm{m\,s^{-1}}$ to $1\,\mathrm{m\,s^{-1}}$ (Dirksen *et al.* 2014). For the wind cube the uncertainty is $0.1\,\mathrm{m\,s^{-1}}$ (Leosphere). In order to characterize the uncertainties in the horizontal and vertical velocity, the uncertainty is estimated statistically. For the velocity this approach is justified by the assumption that the mean velocity should

be constant (especially for the vertical velocity) and the deviations are random. For the statistical estimation, the uncertainty is taken to be the standard deviation of the measured quantities (Committee Guides Metrology 2008):

$$u(X) = \frac{1}{N-1}\sum_{j=1}^{N}(X_j - \overline{X})^2, \tag{48}$$

where $\overline{X}$ is the mean of the measurements. The vertical velocities are calculated from the height and time of the measurement points. The horizontal velocities are calculated using the equation 41. Using this method, the standard uncertainty for the vertical velocity is $5.47\,\mathrm{m\,s^{-1}}$ during the descend leg and $2.63\,\mathrm{m\,s^{-1}}$ for the ascend leg. Similarly for the horizontal velocity, the uncertainty is $0.11\,\mathrm{m\,s^{-1}}$. Since the uncertainty in the horizontal velocity is much smaller than in the vertical velocity, the uncertainty for the velocity is calculated based on the uncertainty in the vertical velocity and the wind speed. Since the ascend leg assumes vertical ventilation speed of 0, an uncertainty of $1\,\mathrm{m\,s^{-1}}$ is added for this leg to account for possible turbulence below the drone. For the wind speed, the uncertainty of $1\,\mathrm{m\,s^{-1}}$ is used. Then, the uncertainty in the ventilation speed can be calculated by applying equation 44 to equation 42, the resulting equation being

$$u(v) = \sqrt{\frac{v_h^2 \cdot u(v_h)^2 + v_v^2 \cdot u(v_v)^2}{v_h^2 + v_v^2}}. \tag{49}$$

The uncertainty calculated with this equation can be entered into the equation 47 to estimate the total uncertainty in radiation corrected temperature.

For the uncertainty in the measured humidity, the uncertainty equation 44 is applied to the humidity correction equation 43. Then for the uncertainty in the humidity we get

$$u_{RH} = \sqrt{\frac{\partial RH_c}{\partial RH_m}u(RH_m)^2 + \frac{\partial RH_c}{\partial p_s(T_h)}u(p_s(T_h))^2 + \frac{\partial RH_c}{\partial p_s(T)}u(T)^2} \tag{50}$$

and after solving the partial derivatives

$$u_{RH} = \sqrt{\frac{p_s(T_H)}{p_s(T)}u(RH_m)^2 + \frac{RH_m}{p_s(T)}u(p_s(T_h))^2 + RH_m\frac{p_s(T_h)}{p_s(T)^2}u(p_s(T))^2}. \tag{51}$$

The uncertainties in the saturated vapor pressure ($u(p_s(T_h))$ and $u(p_s(T))$) are calculated using the numerical estimation of uncertainty (equation 45). Then for the saturation vapor pressure we get the uncertainty

$$u_p(T) = \frac{1}{2}[p_s(T + u(T)) - p_s(T - u(T))]. \tag{52}$$

For the uncertainty in RH_m, the value of 1 % is used (table 1, divided by 2). The total uncertainty for the measured humidity is calculated by combining equations 51 and 52.

Example calculation

An example calculation for the temperature correction and the uncertainties in temperature and humidity are presented here. Let's consider the conditions observed at 06.09.2018 at 07:37 UTC. At the height of 30.7 m the temperature measured was 18.0 °C, the wind speed was 1.74 $\mathrm{m\,s^{-1}}$ and the global radiation was 412.2 $\mathrm{W\,m^{-2}}$. Measured pressure was 1002.6 hPa. Using the equation 39, we can estimate the radiation error on the sensor. For this the ventilation speed has to be estimated. This can be calculated with equation 42. The horizontal ventilation speed is calculated with equation 41, for this observation it is 1.53 $\mathrm{m\,s^{-1}}$. For the ascend leg the v_v is 0 and thus the total ventilation is simply 1.53 $\mathrm{m\,s^{-1}}$. Then the radiation error is

$$\Delta T = 0.18 \cdot \frac{412.2}{1002.6 \cdot 1.53} = 0.09, \tag{53}$$

thus the error for the ascending leg is 0.09 °C. Under the same conditions but during the descend leg, we set the v_v in equation 42 to $-1.5\,\mathrm{m\,s^{-1}}$ to correspond the descending velocity. Then the total ventilation is 2.14 $\mathrm{m\,s^{-1}}$ and the radiation error can be calculated with equation 53 after replacing the ventilation speed. Thus we get the radiation error of 0.07 °C during the descend leg. Finally, the corrected temperature would be 17.91 °C for the ascending leg and 17.93 °C for the descending leg.

To estimate the uncertainty in theses corrections, we use equation 47 with the given uncertainty parameters. For radiation of 412.2 $\mathrm{W\,m^{-2}}$ the uncertainty $u(I)$ is 12.4 $\mathrm{W\,m^{-2}}$. The uncertainty in the ventilation speed can be calculated with equation 49. Then for the ascending leg the ventilation uncertainty $u(v)$ is 1.4 $\mathrm{m\,s^{-1}}$. For the descending leg the uncertainty is 3.7 $\mathrm{m\,s^{-1}}$. Then, after plugging these into the equation 47 the uncertainty estimations for the temperature can be calculated. For the ascending leg this uncertainty is 0.13 °C and for the descending leg 0.08 °C.

For the same case, the measured humidity was 65.8 %. The temperature of the humidity sensor was measured to be 19.8 °C, slightly higher than the ambient temperature 18.0 °C. Then, the measured humidity is corrected using the equation 43. Using equation 38 we get the saturation vapor pressure in the ambient air to be 2310.5 hPa and inside the sensor 2064.7 hPa. Plugging these with the measured humidity into the correction equation we get the actual ambient relative humidity to be 73.6 %. The uncertainty can be estimated with the equations 51 and 52. Since we use the uncorrected temperature for the calculation, the uncertainty in the temperature is the uncertainty of the sensor, 0.05 °C. This leads to uncertainty of 1.2 %, which is only slightly higher than the uncertainty of the sensor itself.

If we use the corrected ambient temperature for the correction of the relative humidity, the corrected humidity is 74.1 % for the ascending leg and 74.0 % for the descending leg. The corresponding uncertainties are 1.4 % for the ascending leg and 1.2 % for the descending leg.

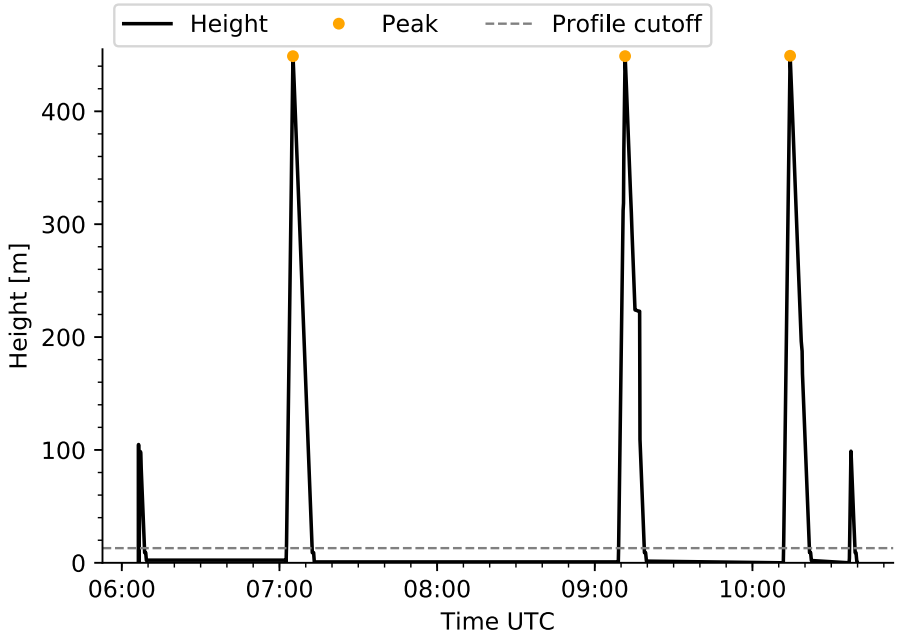

Figure 12. *Time series of the drone height from measurements at 31.08.2018. The black line indicates the height and the orange dots indicate the detected peaks for the height where from the ascend and descend are determined.*

3.6 Data acquisition

The data from the drone is saved in a text-file and stored online for the end user. Each file contains data for one day of measurements. In order to get the data from ascends and descends, these legs must be detected and extracted from the data set. To do this, the data is first read from the text-file into a dataframe. From the data the height is used as a determining variable for the leg. First from the measured heights the peaks above 300 m were detected: these are used as the peak heights for the drone flight (figure 12). Then from these points the height curve is followed forwards and backward in time, until the height is below 13 m: the data between these points are the ascend and descend for backward and forward in time, respectively (figure 13). Finally, all of these ascend - descend pairs are stored individually for further analysis.

The reason the data is only considered for heights above 13 m is that at this height on the descend leg the drone starts the automatic detection of the ground station. This can cause the drone to hover at fixed height for extended periods of time, and because the interest of this work is in the descending phase instead of a hovering drone, this data is excluded from the data analysis. However an example case of the measurements taken during this phase is discussed in section 4.6.

Before detecting the flight legs, spikes in height that are likely caused by measurement errors are removed. Spikes are determined by points that are more than 10-times higher when compared to their adjacent points. These are replaced with a an average height of

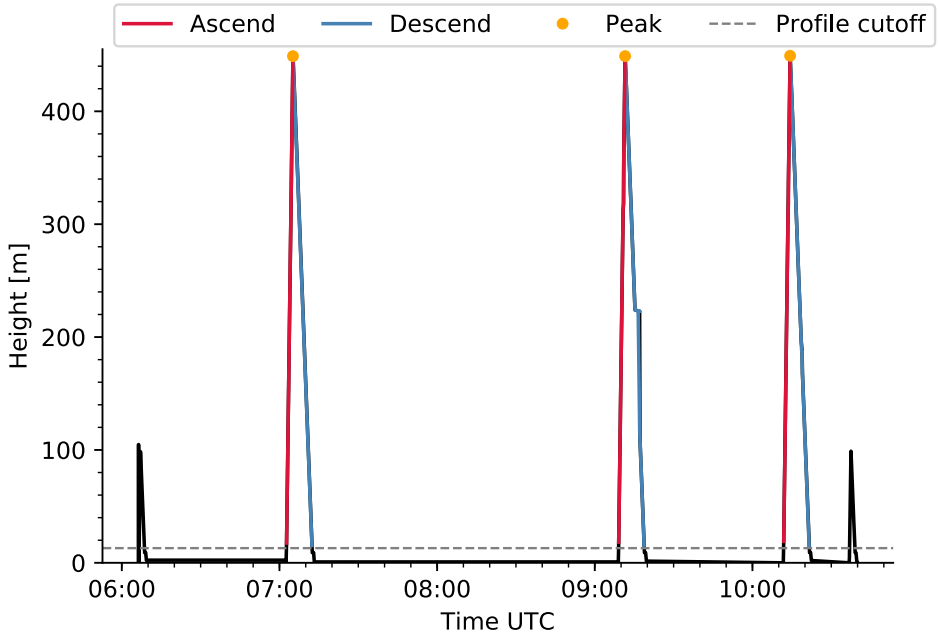

Figure 13. *The detected ascend and descend phases from the drone flight. A red line indicated an ascending phase and a blue line indicates a descending phase.*

the adjacent points. After removal of the spikes and detecting the legs, the horizontal velocity of the drone is calculated using the equation 41 and the method described in section 3.4.1. Using the required auxiliary data for the radiation and wind speed from the measurement site, the corrections for time lag and radiation are applied as described in section 3.4. Finally, the data is stored locally for further analysis.

3.7 Statistical methods

For the analysis of the data set, statistical methods are used. Mainly the used analysis technique is the student's t-test, which test either if the mean values of two data sets are statistically different or if the mean value of one data set is a given value. The t-test assumes normal distribution. For two data sets, the null hypothesis is $H_0 : \mu_1 = \mu_2$. The test value t is calculated as

$$t = \frac{\bar{x}_1 - \bar{x}_2}{\sqrt{\frac{s_1}{n} + \frac{s_2}{n}}}, \tag{54}$$

where $\bar{x}$ is the mean value of data set x, s is the variance of the data set and subscripts 1 and 2 refer to the two data different data sets. From this test variable t, the probability value p ,that the null hypothesis H_0 is true, can be calculated. Thus, if the probability value p is small (usually $p < 0.05$), the null hypothesis is rejected. Otherwise the conclusion is that the two measured means are not statistically different. (Fisher 1925). The t-test assumes a normal distribution, however with a large enough dataset this condition is usually satisfied according to the central limit theorem (Fisher 1925).

Sometimes the measured data also includes some data points far outside the otherwise

normally distributed data. These can often be traced to measurement errors or changing measurement conditions, and are called outliers. The detection of these data points can be done statistically, and there are few different methods for this. In this work a rather simple method that relies on interquartile range is used (Wilks 2005). The basis of this method is that the 1st and 3rd quartiles ($q_{0.25}$ and $q_{0.75}$ respectively) are calculated. Then the interquartile range (IQR) is defined as

$$IQR = q_{0.75} - q_{0.25} \tag{55}$$

and the limits for the outliers (upper limit l_u and lower limit l_l) are defined as

$$l_u = q_{0.75} + 1.5 \cdot IQR, \tag{56}$$

$$l_l = q_{0.25} - 1.5 \cdot IQR. \tag{57}$$

The data points lying outside of these limits are taken into consideration separately in order to explain the reason for the data lying outside the distribution.

4. RESULTS

In this chapter the results of the study are presented. In the section 4.1 two cases of example measurements are presented and discussed, and in the section 4.2 the measured data is analyzed using statistical methods. In the section 4.3 some cases with distinctly higher differences are analyzed in more detail. The section 4.4 describes the application of the radiation correction mentioned in section 3.4, in order to find out how it affects the measured temperature. The section 4.5 investigates the wind speed effect on the measured temperature difference to find out if the mixing of air caused by the wind affects the observed difference. In the section 4.6 the focus is on the behaviour of the temperature when the drone is not ascending or descending but hovering at a fixed height in order to characterize this behaviour.

4.1 Case studies

An example of measurements is presented in figure 14. The measured quantities from left are temperature, relative humidity and pressure. Measurements during the ascend leg are indicated by red curve and measurements during the descend leg by blue curve. The radiosonde measurements are indicated by dotted black curve. The uncertainty estimates are indicated by the lightly shaded area, according to the color of the curve. The black dots indicate the measurements taken on the ground level at the beginning of the drone flight.

The drone measurements are taken at the site in Jokioinen on 06.09.2018, ascend starting at 11:44 UTC and descend starting at 11:47 UTC and the radiosonde measurement starting at 11:30 UTC at the same location. For this profile the ascend temperature decreases monotonically from 19.6 °C at the height of 20 m to 15.4 °C at the height of 446 m. For the descend leg the temperature goes similarly almost monotonically from 19.1 °C at 17 m to 14.7 °C at 447 m. However during the descend leg there is a small temperature anomaly at around 420 m. For the radiosonde the temperature at ground level is 19.4 °C and 14.6 °C at 449 m. The temperature measured at ground level is 19.4 °C, agreeing well with the radiosonde measurement.

From the drone measurements a higher temperature anomaly from the radiosounding can be seen at the very top of the profile where the drone switches from ascending leg to descending leg. This is likely caused by the slower ascend velocity at the end of the leg and the drone being momentarily stationary at the turning point. The effect of the heat convected from the drone at this stage of the flight can cause the momentarily higher differences.

	Ascend	Descend	Each other
Median	0.68 °C	0.12 °C	0.58 °C
Mean	0.68 °C	0.11 °C	0.56 °C
Relative median	0.23 %	0.04 %	0.19 %
Relative mean	0.24 %	0.04 %	0.20 %

Table 2. *Median, mean, relative median and relative mean differences for temperatures measured on 06.09.2018 for the ascend leg at 11:44 UTC and descend leg at 11:47 UTC and radiosonde at 11:30 UTC. The columns indicate the differences between ascend and radiosonde (left), descend and radiosonde (middle) and between ascend and descend (left). Case 1.*

	Ascend	Descend	Each other
Median	−3.7 %	0.52 %	−4.12 %
Mean	−3.7 %	0.48 %	−4.15 %
Relative median	−4.8 %	0.7 %	−5.6 %
Relative mean	−4.8 %	0.7 %	−5.5 %

Table 3. *Median, mean, relative median and relative mean differences for relative humidities measured on 06.09.2018 for the ascend leg at 11:44 UTC and descend leg at 11:47 UTC and radiosonde at 11:30 UTC. The columns indicate the differences between ascend and radiosonde (left), descend and radiosonde (middle) and between ascend and descend (left). Case 1.*

The temperature measurement shows almost constant positive bias on ascend leg compared to descend and radiosonde, indicating that the air mass being measured at the ascend leg is not the same as during the descend leg. Also there is a small positive bias on the descend leg when compared to the radiosonde. When compared to the ground measurements the radiosonde and the descending leg agree better with the measured temperature than the ascend leg.

The median and mean differences as well as relative differences for temperature measurements are gathered on table 2. The humidity measurements show similarly better agreement between descend leg and radiosonde than between ascend leg and radiosonde. The humidity increases as with height also almost monotonically, in the ascend leg from 56.4 % at 20 m to 15.4 % at 446 m. For the descend leg the humidity increases from 52.0 % at 17 m to 60.4 % at 447 m. Lastly the radiosonde measured humidity of 69.7 % at the ground level and 82.0 % at 449 m. The humidity measured at the ground level is 70 %, which also agrees well with the radiosonde. The ascend leg for the humidity measurements shows a almost constant dry bias. Again, the radiosonde and the descending leg agree well with the ground measurements but the ascending leg seems to be far off. For this measurement the mean, median, relative median and relative mean differences are gathered in table 3.

The pressure measurements shown on the rightmost panel shows a practically constant slope from the surface to the top of the measured profile, which is expected since the

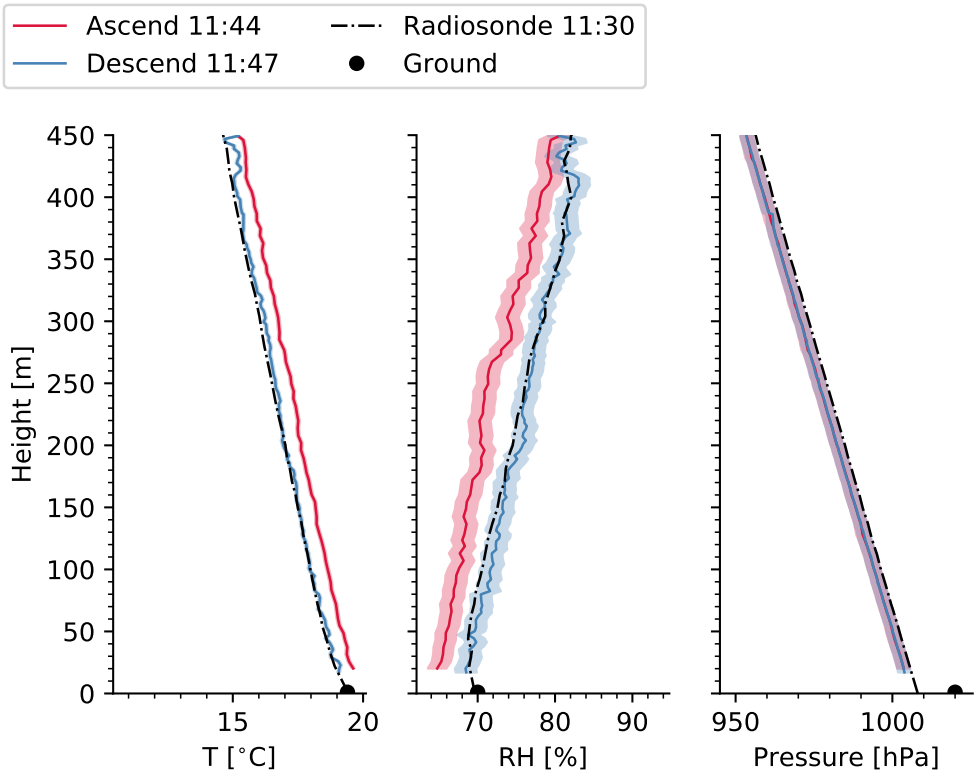

Figure 14. *Measured profiles of temperature, humidity and pressure. The measurements taken during ascend phase are indicated by red curve and the measurements during descend phase by blue curve. The dotted black curve indicates the reference measurements taken with radiosonde. The shaded areas indicate the uncertainty estimation. The black dots at the ground level indicate the ground measurements. Measurements are conducted at the measurement site in Jokioinen at 06.09.2018, ascend leg starting at 11:44 and descend leg at 11:47 UTC. Radiosonde launched at 11:30. Case 1.*

height is calculated from the pressure. At height of 22 m the radiosonde measures a pressure of 1006 hPa, and ascend and descend leg both measure the pressure of 1004 hPa at 20 m. Thus small difference in measured pressure can be seen between drone measurements and the radiosonde, but this can be attributed to the calibration of the sensors. Since the pressure is only used to calculate the height in the measurements, it is not of particular interest in this study and thus from now on only the temperature and humidity measurements will be considered.

The figure 15 shows the absolute differences in measured temperature and humidity of case 1. The temperature anomaly on the descend leg stays below 0.2 °C almost in the whole profile, the only exception being the bigger difference at around 420 m. For the ascend leg the difference is between 0.6 °C and 0.8 °C in the profile. Also the anomaly of the ascend leg at the lower altitude is closer to the difference between ascend leg and descend leg, while at higher altitude above 220 m the anomaly is clearly larger.

For the humidity measurement the anomaly during the descending leg is smaller at higher

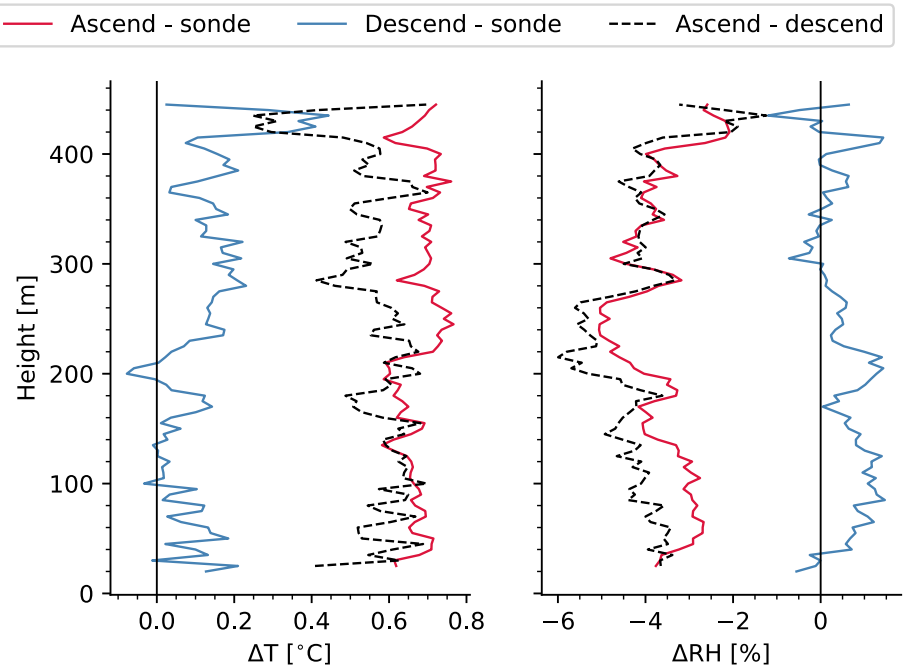

Figure 15. *Differences of temperature and humidity for case 1. The red and blue curves indicate the anomaly of ascend and descend from radiosonde, respectively. The dashed black curve indicate the difference between the ascend and descend legs. Temperature difference is on the left-hand profile and the humidity difference on the right-hand profile. The black vertical curves indicate the curve for 0 difference.*

altitude above 300 m and at lower altitude the anomaly is slightly higher. Unlike in the temperature profile, the anomaly during the ascending leg is close to the difference between the ascending and descending legs at higher altitudes, and in lowers altitudes the anomaly is lower than the difference between the legs.

In both profiles, the difference at the top of the profile is not 0, although this is what we would expect at the top where the drone turns back. This is caused by the interpolation of the data. The data has to be interpolated because the measurement heights are not necessarily the same during ascending and descending legs. In order to compare the differences at different heights the data has to be interpolated to make comparisons at the same height possible.

Another case example of a measurement is presented in figure 16. In this profile the ascend leg starts at 05:36 UTC, the descend leg at 05:38 UTC and the radiosonde is launched at 05:30 UTC. The time difference between the radiosonde and the drone flights then less than 10 minutes, and thus the temporal difference in measurements is small. In this measurement an inversion layer can be seen in the temperature profile between 230 m and 260 m. In this layer the behaviour of the temperature profile inverses: the temperature does not decrease monotonically as the altitude increases, but rather increases inside the layer before starting to decrease again. From this measurement it can be seen that the radiosonde and ascending leg detect the inversion layer at almost the same height, but

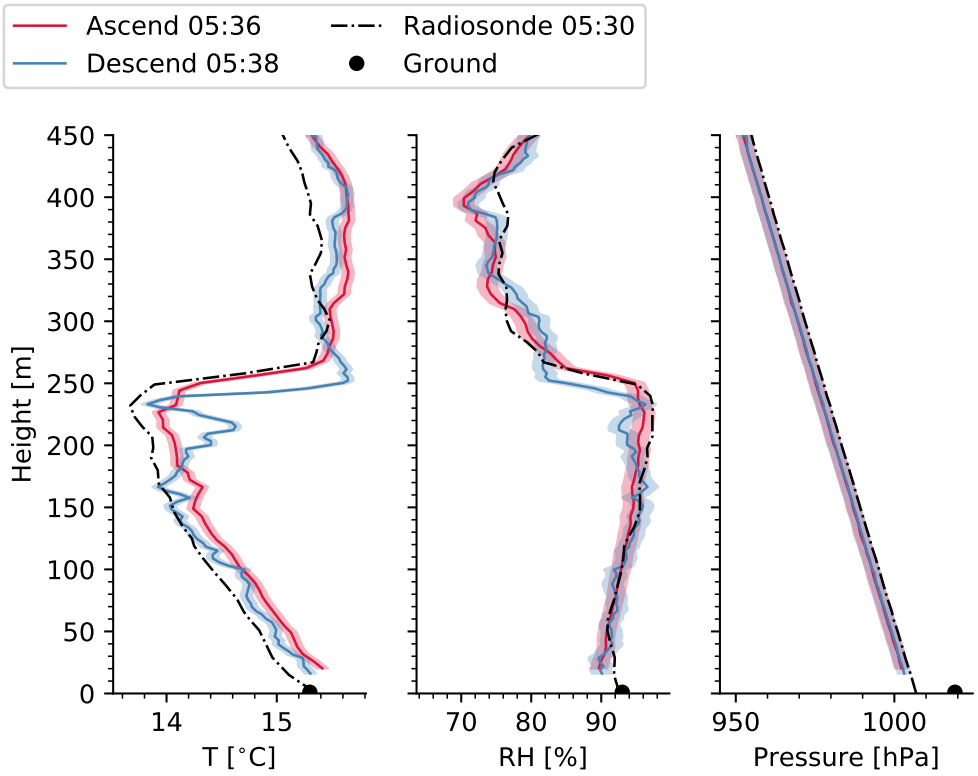

Figure 16. *Measured profiles of temperature, humidity and pressure. The measurements taken during ascend phase are indicated by solid, red curve and the measurements taken during descend phase by dashed, blue curve. The dotted black curve indicates the reference measurements taken with radiosonde. The shaded areas indicate the uncertainty estimation. The black dots at the ground level indicate the ground measurements. Measurements are conducted at the measurement site in Jokioinen at 07.09.2018 ascend leg starting at 05:36 UTC and descend leg at 05:38 UTC. The radiosonde is launched at 05:30 UTC. Case 2*

the descending leg detects it approximately 20 m lower. This can be caused by the air being pushed downwards by the rotors of the drone, thus pushing the layer of warmer air downwards at the location where the drone is measuring. Personal communication with researcher David Brus revealed similar phenomena being observed during aerosol measurements with a drone. Another explanation for the difference could be the time lag of the sensor, as during the descend leg due to the response time the measured temperature gradient would appear lower than during the ascend leg.

The inversion layer can also be seen in the humidity profile, albeit less clearly. In the humidity profile similar phenomena is visible where the ascending leg and the radiosonde measurement detected the change at higher altitude than the descending leg. For this measurements the temperature decreases first from 15.4 °C at the height of 20 m to 13.9 °C at 227 m during the ascend leg and from 15.3 °C at 16 m to 13.8 °C at 233 m during the descend leg. The radiosonde measures temperature of 15.3 °C at ground level and 13.7 °C at the height of 232 m. After this initial decrease in the temperature, the temperature rises to

	Ascend	Descend	Each other
Median	0.27 °C	0.17 °C	0.09 °C
Mean	0.25 °C	0.24 °C	0.01 °C
Relative median	0.09 %	0.06 %	0.03 %
Relative mean	0.09 %	0.08 %	0.00 %

Table 4. *Median, mean, relative median and relative mean for differences in temperature. The columns indicate the differences between ascend and radiosonde (left), descend and radiosonde (middle) and between ascend and descend (left). Case 2.*

15.4 °C at 270 m during the ascend leg and to 15.6 °C at 250 m during the descend phase. The radiosonde measures temperature of 15.3 °C at 267 m. At the top of the profile, 450 m the drone measures temperature of 15.3 °C and the radiosonde 15.0 °C. The temperature measured at the ground level is 15.3 °C, again agreeing with the radiosonde. Also the descending leg is in better agreement with the ground data than the ascending leg. For the humidity profile the measured humidity leg is 89.7 % at 20 m and increases to 96.1 % at 227 m during the ascend leg. During the descend leg the humidity is 90.1 % at 16 m and increases to 94.2 % at 240 m. The radiosonde measures humidity of 92.6 % at ground level and increases to 97.4 % at 232 m. From there the humidity decreases sharply in all profiles to 85.0 % at 262 m during the ascend phase, 84.7 % at 250 m during the descend phase and 81.8 % at 267 m for the radiosonde measurement. Above these altitudes the decrease is slower, and at the top of the profile the measured humidity 79.7 % for the drone. At this height the radiosonde measures humidity of 82.3 %. The humidity measured at the ground level is 93.0 %, showing again good agreement with the radiosonde. Here the descending leg yet again agrees better with the ground measurements as opposed to the ascending leg which seems to have high dry bias.

In both temperature and humidity profiles of case 2, there is a noticeably anomaly during the descend leg just below the inversion layer, showing a temperature difference of almost 1 °C and humidity difference of almost 5 % compared to the ascend leg and the radiosonde at the same altitude. The cause of this anomaly is not known, but it is suspected to be related to the turbulence of the atmosphere. The mean, median, relative mean and relative median of the temperature differences for case 2 are presented in table 4. While according to the table the ascending leg and descending leg would compare very well against each other, this is caused by the big negative bias during the ascend leg in temperature inside the inversion layer compared to smaller positive bias outside it.

For humidity the differences are presented in table 5. The differences from measurement case 2 are presented in figure 17. Similarly to the case 1, the temperature differences are in the left-hand side profile and the humidity differences in right-hand side profile. In the difference profile the higher differences between ascend and descend leg and higher descend anomaly can be seen in the inversion layer. Similarly in the differences of measured humidities the inversion layer is visible. The large differences inside the inversion layer indicates that in case of inversion the drone measurements do not perform as well

	Ascend	Descend	Each other
Median	−0.80 %	−0.36 %	−0.49 %
Mean	−0.67 %	−0.62 %	−0.07 %
Relative median	−1.0 %	−0.4 %	−0.5 %
Relative mean	−0.8 %	−0.6 %	−0.1 %

Table 5. *Median, mean, relative median and relative mean for differences in humidity. The columns indicate the differences between ascend and radiosonde (left), descend and radiosonde (middle) and between ascend and descend (left). Case 2.*

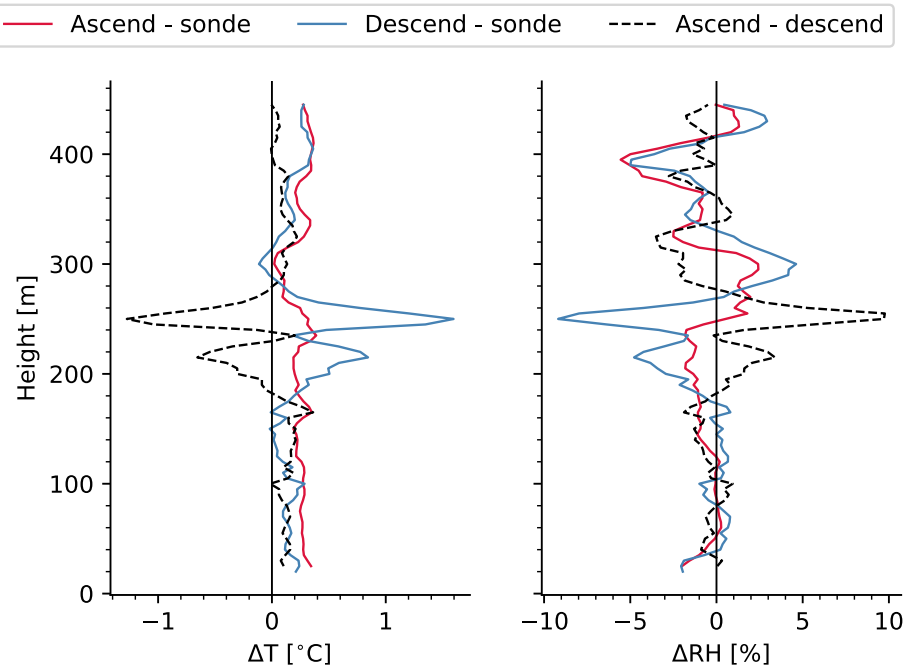

Figure 17. *Differences of temperature and humidity for case 2. The red and blue curves indicate the anomaly of ascend and descend from radiosonde, respectively. The dashed black curve indicate the difference between the ascend and descend legs. Temperature difference is on the left-hand profile and the humidity difference on the right-hand profile. The black vertical curves indicate the curve for 0 difference.*

as in cases when the temperature and humidity are changing monotonically through the atmosphere.

Based on these two cases, it is evident that the descending leg seems to have better agreement with the radiosonde and ground measurements. The ascending leg of the flight has biases in both temperature and humidity, and these biases seem to be rather constant throughout the measured profiles. In the next section a statistical analysis is performed on all the measured profiles to see if the bias is also present in other measurements.

4.2 Statistical analysis

To get a better idea of the differences between ascend and descend legs, a statistical analysis was performed for the measured temperatures and humidities. In total the analysis in-

cludes 32 different measurement flights, made between 31.08.2018 and 12.09.2018. Some measurements had to be excluded due to irregular flight patterns or sensor errors. For comparison with the radiosonde, 10 flights had radiosondes launched sufficiently close (temporal difference less than 30 minutes) to the measurement of the drone. Figure 18

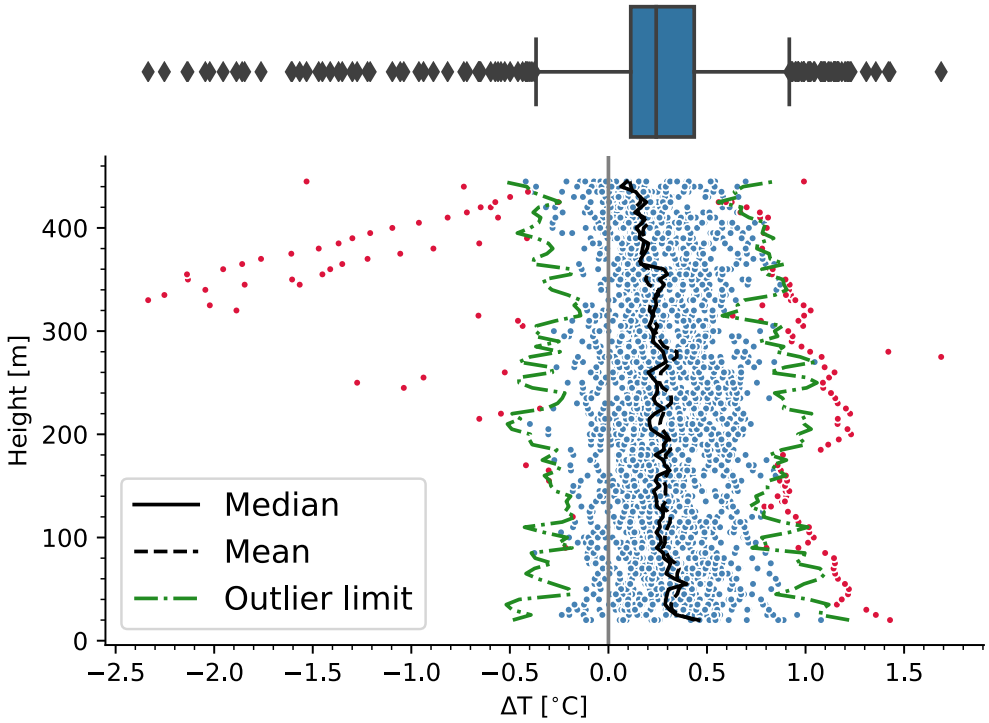

Figure 18. *Differences between ascend and descend leg from all measurements. Boxplot on the top summarizes the median, 1st and 3rd quartiles and outliers from the whole dataset. The scatter plot below shows the height distribution of the temperature differences as well as the median and mean profiles and the outlier limits. The outliers of the data are marked in red.*

summarizes the differences in measured temperatures from all of the flights. The box plot on the top indicates the median, 1st and 3rd quantiles as well as the outlier limits for the whole dataset. The scatter plot below shows the height distribution for the temperature differences. The outlier limits are marked in green and the outlier measurements in red. From the scatter plot it is evident that the outliers are not randomly distributed along the profiles, but rather they are always connected to same profiles. The outliers were calculated with the inter-quartile range method using equation 57. Since the dataset is reasonably small, the measurements where outliers were detected were taken for a more detailed study. The details of the outliers will be presented in section 4.3. With this motivation the outliers were separated from the rest of the data, and the rest of the statistical analysis will be carried on without them. From the total dataset, 4.8 % of the data points were classified as outliers.

The temperatures measured during ascend and descend leg after removal of the outliers are plotted against each other in the figure 19. Also the diagonal is plotted in the solid

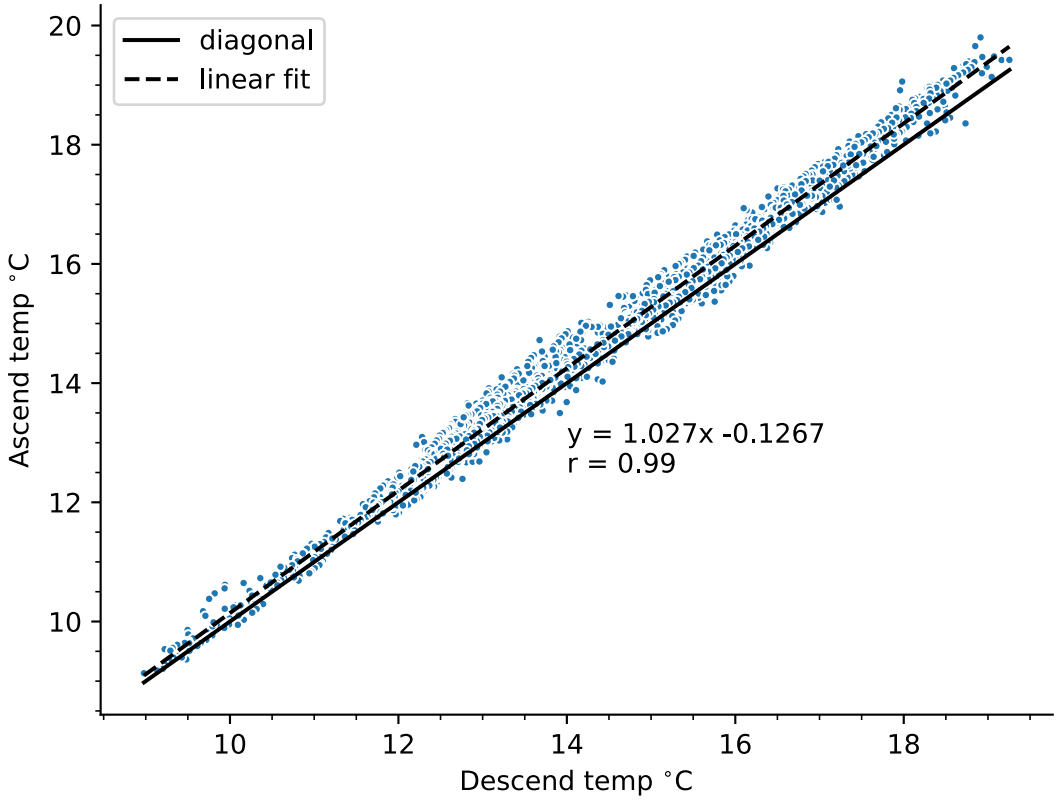

Figure 19. *The temperature measured during ascend leg and descend leg plotted against each other. The diagonal curve is drawn in solid curve and the fitted linear regression in dashed black curve. For the linear fit, the r-value is 0.99.*

black curve and and linear fit in a dashed black curve. As it can be seen in the figure, there is a small positive bias in the ascend temperature. The black dashed curve indicates the linear fit of the ascend temperature to the descend temperature. It also seems that the difference between the temperatures increases slightly with the absolute temperature. The minimum measured temperature was 9.1 °C during the ascend leg and 9.0 °C during the descend leg. The maximum temperature measured was 19.8 °C during the ascend leg and 19.3 °C during the descend leg. The average temperature for ascend leg was 14.9 °C and for the descend leg 14.6 °C. The r-value for the linear fit is 0.99, indicating a good correlation between the temperatures measured during both legs. Also the root mean squared error (RMSE) between the temperature measured in ascend leg and descend leg was calculated, and it is 0.34 °C.

Similarly for humidity, the height distribution of the differences as well as the related boxplot can be seen in figure 20. The distribution seems rather similar to the temperature difference distribution. No strong dependence on heights is evident, the distribution seems to even at each height. Outliers are also evident in humidity observations. However, in the humidity measurements the interquartile range (the width of the box plot) is smaller in the temperature measurements. Similarly to temperature measurements, alot of outliers can be seen above 300 m. These can be related to the outliers in temperature, since the

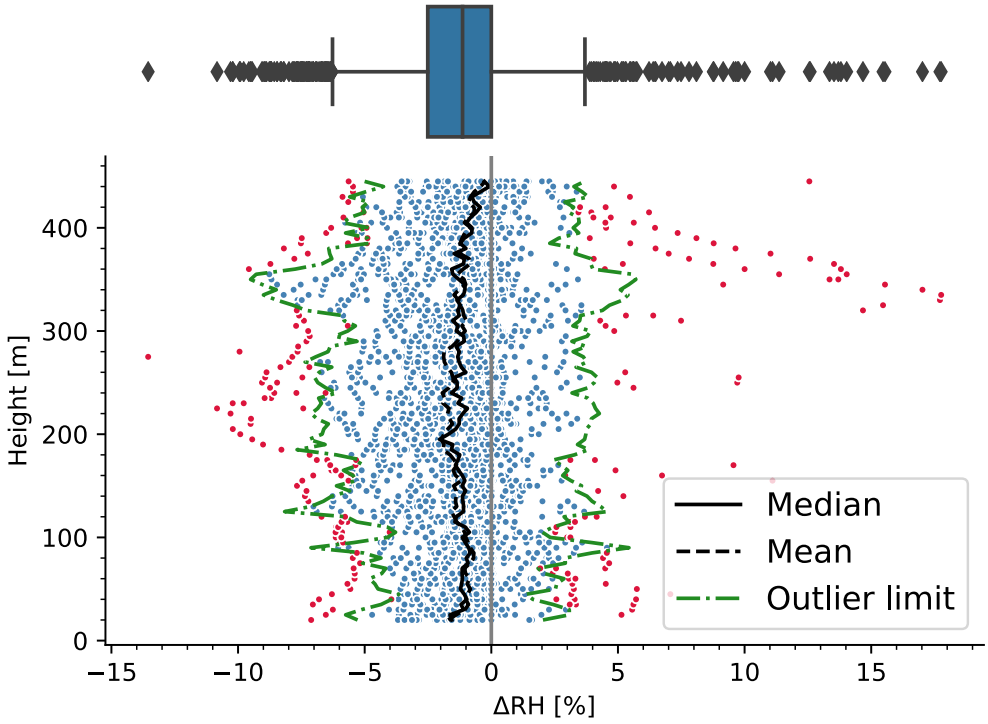

Figure 20. *Humidity differences between ascend and descend leg from all measurements. Boxplot on the top summarizes the median, 1st and 3rd quartiles and outliers from the whole dataset. The scatter plot below shows the height distribution of the temperature differences as well as the median and mean profiles and the outlier limits. The outliers of the data are marked in red.*

measured ambient temperature is needed for the humidity correction, using equation 37. Thus if there are strong outliers in the measured temperature these outliers can also be seen in the corrected humidity measurements. Similarly to the temperature measurements, these outliers were removed and considered separately. For the humidity measurements 7.8 % of the data points were labeled as outliers.

As with the temperature measurement, the humidity measurements during the ascend leg and descend leg were plotted against each other. This comparison can be seen in figure 21. As can be seen in the figure 21, the bias in for the humidity during the ascend leg is generally negative, and is spread out more above 65 %. The minimum humidity measured during the ascend leg was 51.2 % and the maximum humidity was 100 %. For the descend leg the minimum measured humidity was 53.2 % and the maximum humidity was 100 %. The mean humidity during the ascend leg was 81.1 % and during the descend leg 82.9 %, and the standard deviation for the ascend leg was 11.1 % and for the descend leg 10.9 %. For the linear fit the r-value is 0.98, and similarly to the temperature measurement indicates a good correlation between the humidities measured between the ascend and descend legs. The RMSE between the ascend and descend leg measurements is 2.6 %.

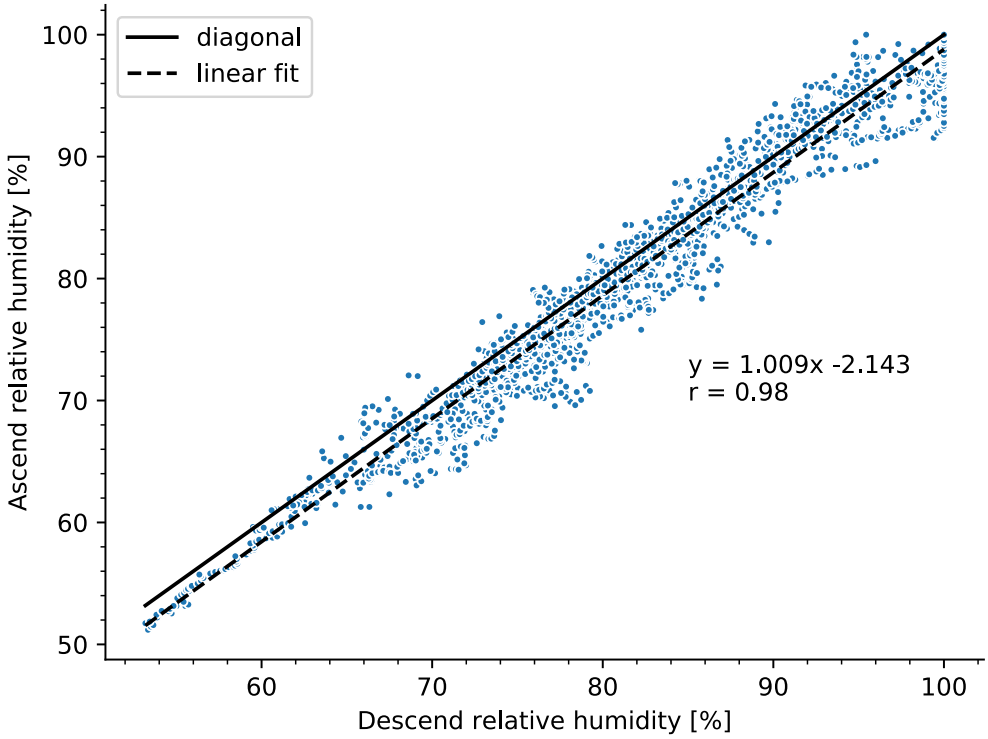

Figure 21. *Measured humidities during the ascend and the descend legs. The black solid curve indicates the diagonal curve and the black dashed curve indicates the linear fit for. For the linear fit the r-value is 0.98.*

The distributions of the differences in measured temperature and humidity are shown in the figure 22. The top panel (A) shows the distribution for temperature differences and the bottom panel (B) shows the distribution for the humidity differences. The solid black curves indicate the median difference and the dashed black curve indicate the mean differences. Also the range for 1 standard deviation is indicated by black dotted curve. Numerical analysis gives the mean difference in measured temperature to be 0.26 °C, and the median difference 0.24 °C. For the temperature differences the standard deviation is 0.22 °C. For the humidity measurements the mean difference is −1.3 %, the median difference is −1.1 %, and the standard deviation is 1.8 %. From the distributions a warm bias in the temperature and a dry bias in the relative humidity in the ascend leg is evident. While both of the distributions are slightly skewed, here the assumption is made that the skewness is small enough for a reliable t-test. For the temperature difference distribution the skewness coefficient is 0.23 and for the humidity difference distribution the skewness coefficient is -0.34. Thus the humidity difference distribution is slightly more skewed and it is skewed towards the negative tail, while the temperature difference distribution is skewed towards positive. After performing a t-test on the differences, in both cases the mean difference is significantly different from 0 ($p \ll 0.05$, H_0: $\Delta T = 0$ (for temperature) and $\Delta RH = 0$ (for humidity)), indicating that the two measurements are taken from two different distributions. This means that the air mass measured during the ascend differs from the air mass measured during the descend. This can be caused by the warming of

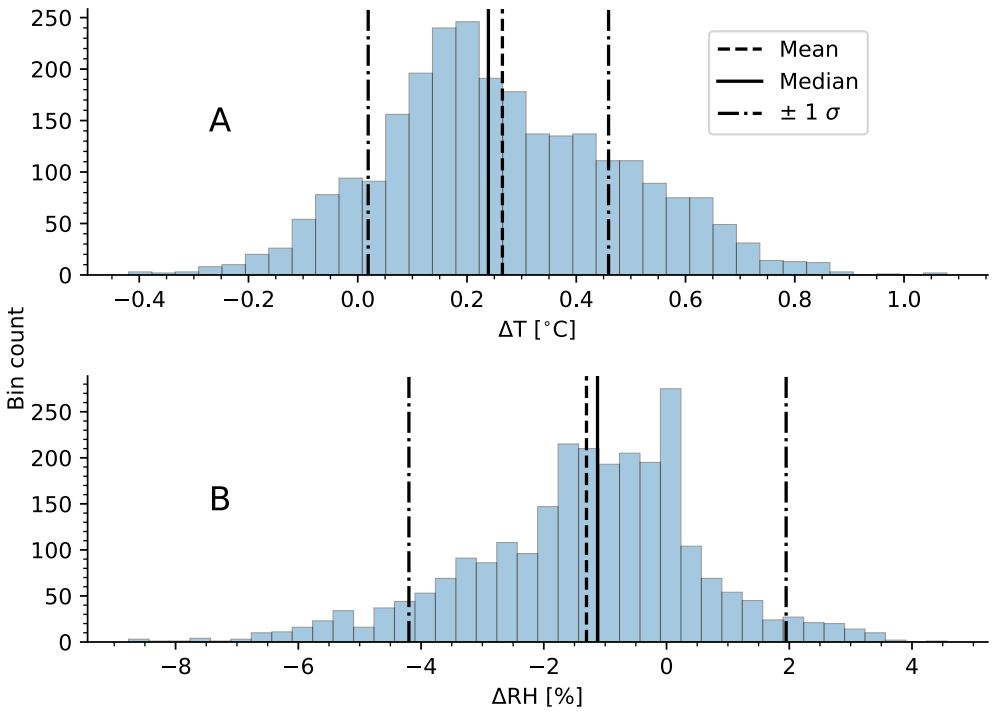

Figure 22. *Distribution of differences in measured temperature (A) and humidity (B) between the ascend leg and the descend leg. The mean difference is indicated by a dashed black curve, the median difference in solid black curve and the dotted curves indicate the range of 1 standard deviation.*

the air mass due to heat convected from the motors of the drone.

In order to evaluate which leg is better in terms of measurement accuracy, a similar analysis was done for the differences between the drone borne measurements and the radiosonde measurements. Height distribution for the differences in temperature during both ascend and descend leg when compared against the radiosonde measurements can be seen in figure 23. The distribution for ascend leg compared against radiosonde is on the distribution A the the descend leg compared against the radiosonde is on the distribution B. The black solid curve indicates the median, the black dashed curve indicates the mean and the green dotted curves indicate the outlier limits for each height. On top of the distributions the box plots represent the whole distribution. From this plot no strong height correlation is evident in neither leg. For the differences in ascend leg (plot A) the mean and median are very similar in the lower altitudes below 290 m approximately. Above this the outlier profile marked in red tends to cause noticeable difference in the mean compared to the median. Similarly for the descend leg (plot B) the strong outliers, especially between 290 m and 350 m cause a distinct difference between the mean and median values. In the ascend leg the mean difference is 0.47 °C and the median is 0.44 °C at 25 m. In the middle of the profile at 250 m the mean and median difference is 0.39 °C. At the top part of the profile at 350 m the mean is 0.18 °C and the median is 0.36 °C. In the descend leg at the lower part the mean difference is 0.17 °C and the median 0.24 °C

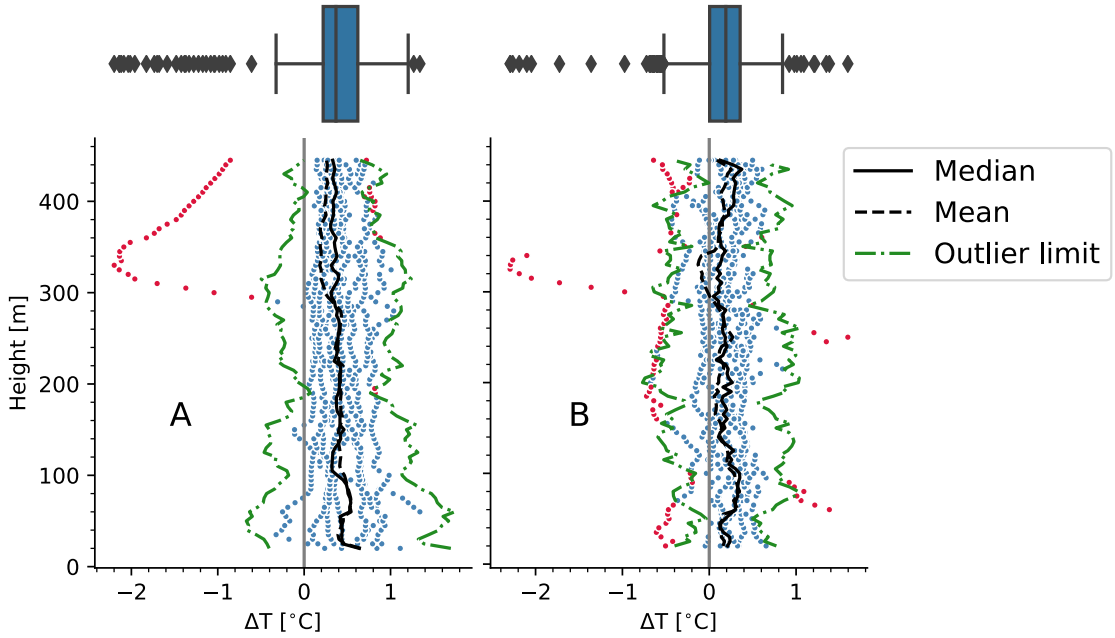

Figure 23. *Height distributions of the differences in temperature during ascend (A) and descend (B) leg when compared against the radiosonde. The boxplot on the top represents the whole distribution. The solid black curve indicated the median, the dashed black curve the mean and the green dotted curves the outlier limits for each height.*

at 25 m. At 250 m the mean is 0.27 °C and the median is 0.19 °C. At the top part of the profile at340 m where an outlier is also visible the mean difference is −0.10 °C and the median 0.15 °C. In this figure similarly few outliers can be noticed. For further analysis these will be removed and considered separately in section 4.3. These distributions already indicate that the difference during the descend leg is closer to 0 than during the ascend leg.

After removing the outliers, the distributions of the temperature differences can be seen in figure 24. The temperature difference in the ascend leg is in the panel A and the difference in the descend leg in panel B. The black solid curve indicates the median, black dashed curve the mean and the range for one standard deviation is marked with black dotted curves. For the ascend leg the median difference is 0.38 °C, the mean difference is 0.42 °C and the standard deviation is 0.25 °C. Similarly for the descend leg the median difference is 0.22 °C, the mean difference is 0.19 °C and the standard deviation is 0.23 °C. These results differ from previous measurements taken by Jonassen *et al.* (2015), who observed a bias of around −0.5 °C in temperature measured with a quadcopter. They compared the measurements against an automatic weather stations aboard RV *Polarstern* in the Weddell sea. However their results similarly shows warmer bias in ascending leg. While it is difficult to say why they observed a negative bias compared to the positive observed in this study, but it could be caused by the different conditions in the measurement sites (during the expedition in the Weddell sea the the temperatures of around −17 °C to −26 °C were reported), or the automatic weather station could have a bias itself.

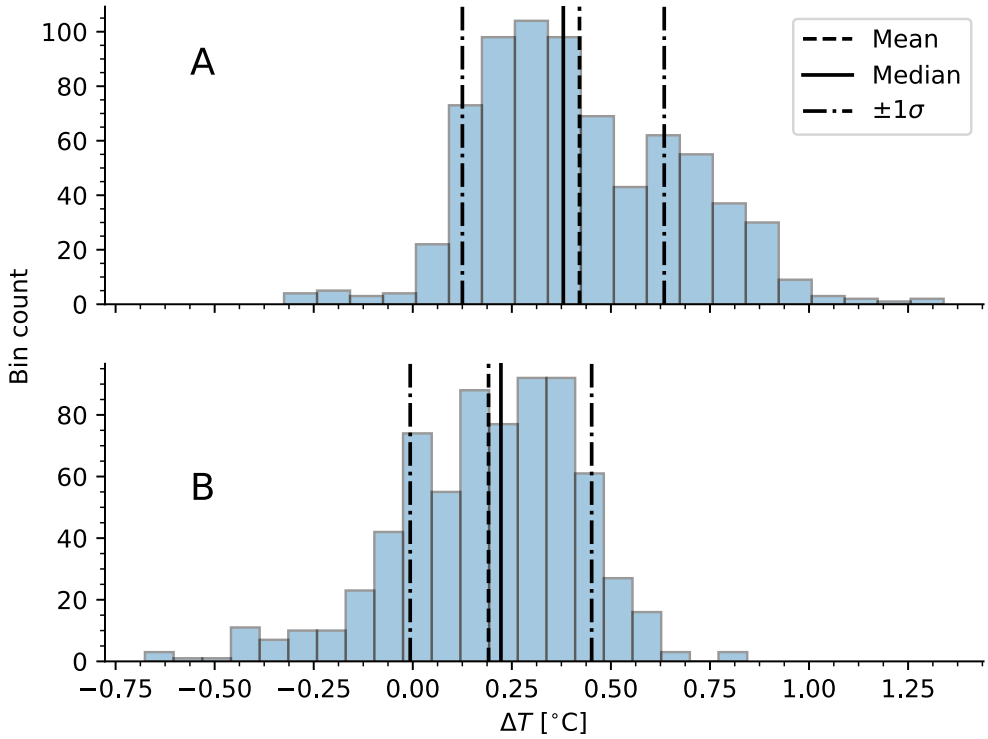

Figure 24. *Temperature difference distributions between the ascend leg and radiosonde (A) and between the descend leg and the radiosonde (B). The black solid curve indicates the median, black dashed curve the mean and the black dotted curve the range for one standard deviation.*

From the distributions and the numerical analysis it is evident that the descend leg agrees better with the radiosonde measurements than the ascend leg. Yet in both legs there exists a bias that was confirmed with a t-test ($p \ll 0.05$ for both distributions, H_0: $\Delta T = 0$), similarly to the differences between the ascending and descending legs.

Similarly the height distribution for the humidity differences was plotted in figure 25. Again the distribution A is the difference between the ascend leg and the radiosonde and the distribution B is the difference between the descend leg and the radiosonde. As before the boxplot at the top represents the whole dataset. Similarly to the temperature difference distributions the outliers are marked in red and the outlier boundaries for each height in green. The black solid curve indicates the median and the black dashed curve the mean. In these distributions the effect of the outliers on the mean is also easily visible. In the distribution A there seems to be a constant outlier profile with distinctly higher difference. In the distribution B the outliers are not as clearly caused by one profile. Again, these outliers will be described in detail in section 4.3. In the humidity difference profiles there does not seem to be strong correlation with height. For the ascend leg in the lower part of the distribution at 25 m the mean difference is $-0.8\,\%$ and the median $-2.2\,\%$. In the middle part of the profile at 250 m the mean difference is $-0.1\,\%$ and the median $-1.4\,\%$.

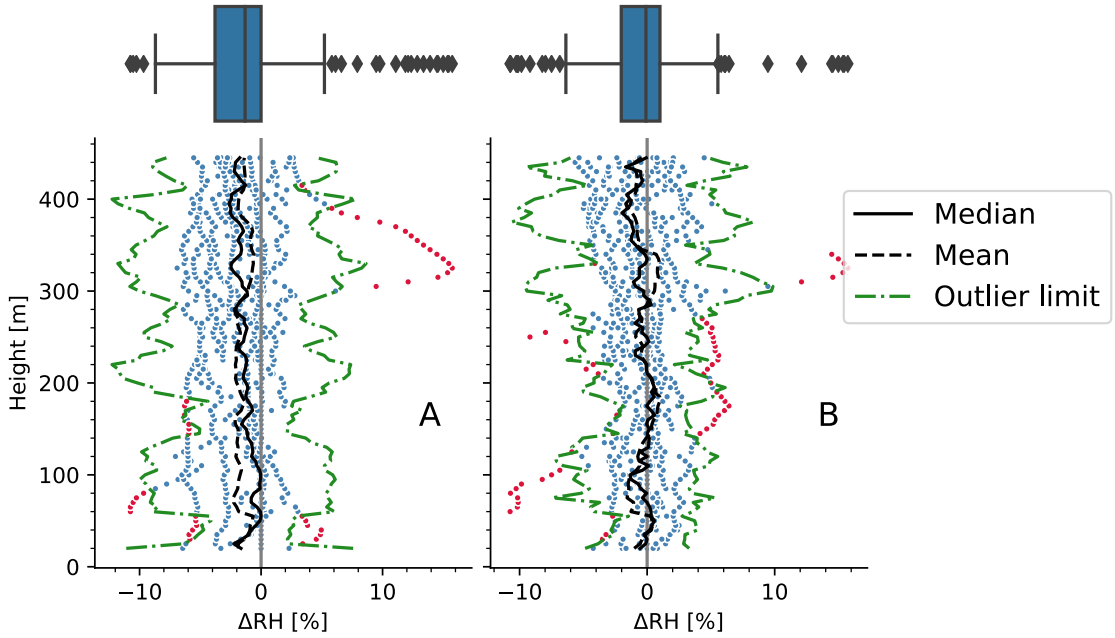

Figure 25. *Height distributions of the differences in humidity during ascend (A) and descend (B) leg when compared against the radiosonde. The boxplot on the top represents the whole distribution. The solid black curve indicates the median, the dashed black curve the mean and the green dotted curves the outlier limits for each height.*

At the very top of the profile at 440 m where there are no outliers the mean difference si -1.4 and the median is -2.1 %. For the descend leg at 25 m the mean difference is 0.3 % and the median is -0.1. In the middle part at 250 m the mean difference is 0.1 % and the median is 0.1 %. At the top of the profile at 440 m the mean difference is 1.5 % and the median is -0.8 %. The humidity distributions indicate that the descend leg agrees better with the radiosonde measurements than the ascend leg, similarly to the temperature measurements.

Again after removing the outliers from the dataset the distributions for the differences in measured humidity can be seen in figure 26. The distribution at the top (A) represents the difference between the ascend leg and the radiosonde measurements and the distribution at the bottom (B) represents the difference between the descend leg and the radiosonde. The black solid curve indicates the median, the dashed curve the mean and the dotted curves the range of one standard deviation from the median. For the differences in the ascend leg the median is -1.4 %, the mean is -1.8 % and the standard deviation is 2.4 %. For the difference in the descend leg the median is -0.1 %, the mean is -0.5 % and the standard deviation is 2.1 %. These values show that the descending leg agrees better with the radiosonde measurements than the ascend leg, similarly to the temperature measurements. Both legs also seem to have a dry bias. The distribution A has a slight skewness of 0.23, and the distribution B has a bit higher of 0.42.

In figure 27 the temperature and humidity measurements taken during the ascend and

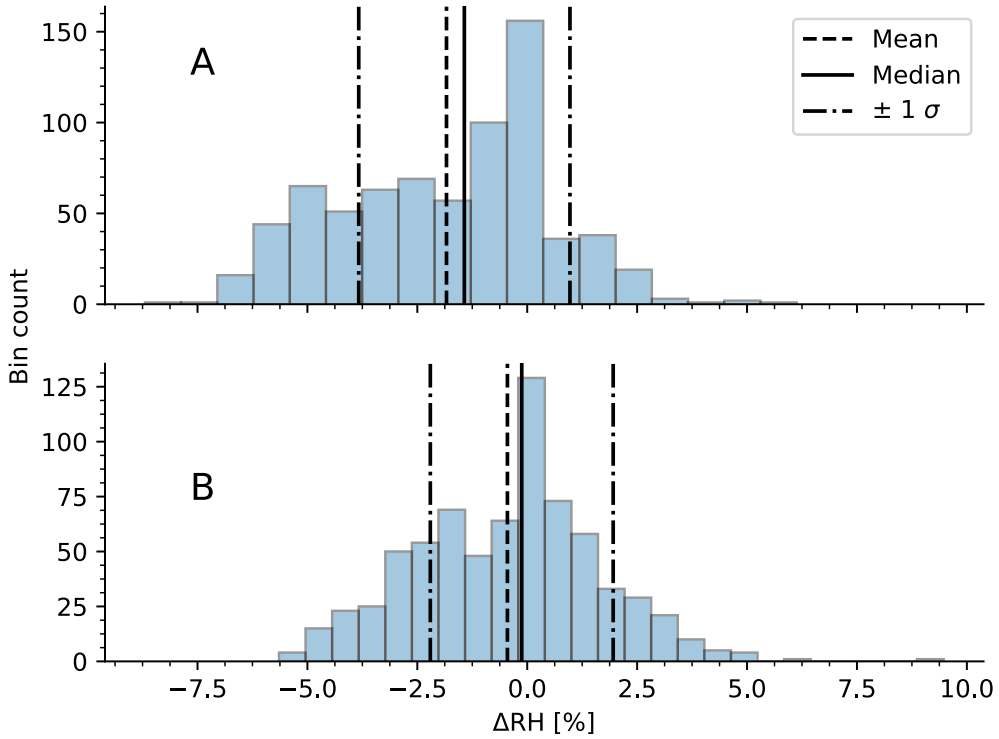

Figure 26. *Distribution of differences in the measured humidity. Top distribution at the top (A) represents the differences between the ascend leg and the radiosonde and the bottom (B) distribution the differences between descend leg and the radiosonde. The black solid curve indicates the median, the dashed curves the mean and the dotted curves the range for one standard deviation.*

descend legs and the radiosonde measurements are compared against each other. The black dashed curves indicate the linear fit to the data and the black solid curve the diagonal curve. In panel A the temperature measured during the ascend leg and the temperature measured by the radiosonde are compared. A positive bias in the measurements taken during the ascend leg can be seen in the figure, and the bias seems to grow slightly towards the higher temperatures. The panel C shows the temperature measurements during the descend leg compared against the radiosonde. Here the temperature measurements agree better with each other, and the linear fit almost fits to the diagonal. Only at the lower temperatures the linear fit deviates slightly from the diagonal. The minimum measured temperature by the radiosonde is 9.0 °C. During the ascend leg the minimum temperature is 9.1 °C and during the descend leg 9.0 °C. The maximum temperature measured by the radiosonde is 19.0 °C. During the ascend leg the maximum temperature is 19.8 °C and during the descend leg 19.1 °C. The mean temperature for the radiosonde measurements is 13.8 °C, for the ascend leg 14.3 °C and for the descend leg 14.0 °C. The standard deviations for the radiosonde, ascend leg and descend leg are 2.4 °C, 2.5 °C and 2.3 °C, respectively.

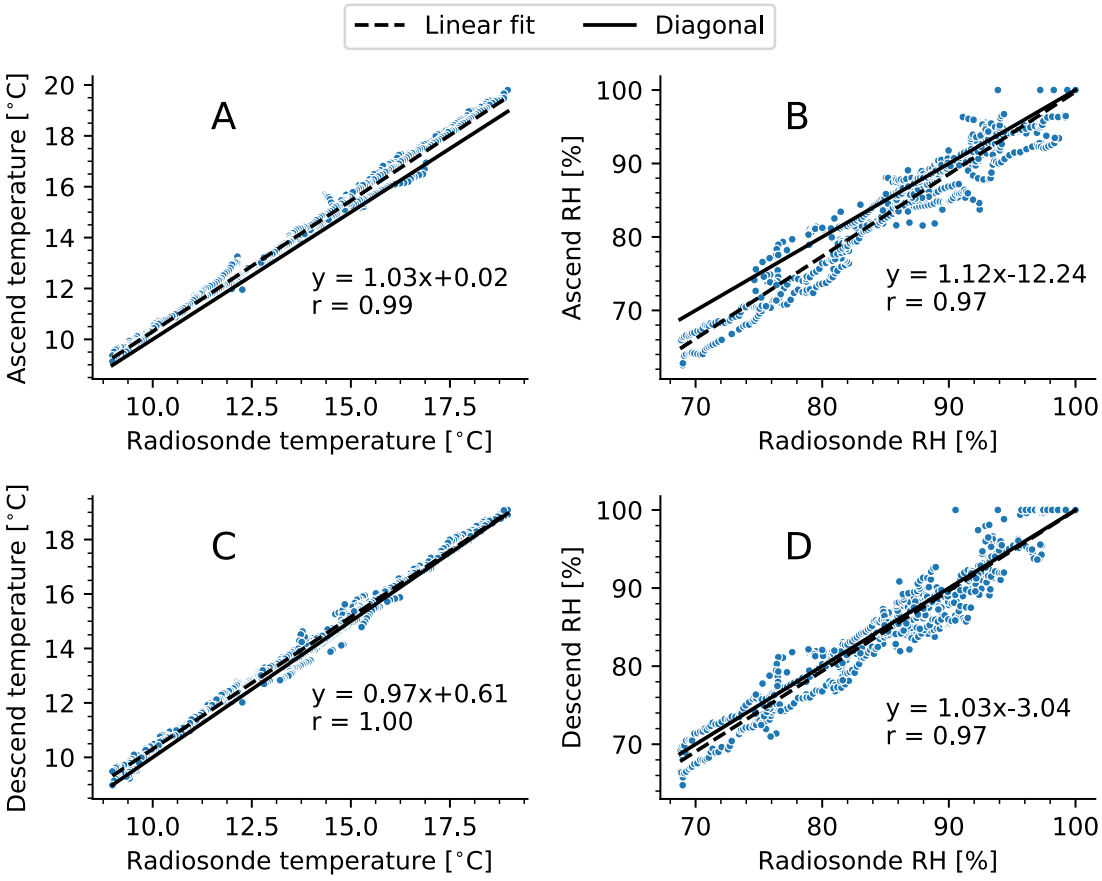

Figure 27. *Comparisons of the temperatures and humidities measured during the ascend leg and the descend leg against the radiosonde measurements. Panels A and C show the comparisons of temperatures during the ascend leg and the descend leg against the radiosonde, respectively. Panels B and D show the comparisons of the humidity measurements during the ascend leg and the descend leg against the radiosonde, respectively. The black solid curve indicates the diagonal curve and the dashed curve the linear fit .*

For comparison, the RMSE was also calculated for each curve. For (A) the RMSE is 0.49 °C and for (C) the RMSE is 0.30 °C. Panels B and D show the measured humidities during the ascend leg (B) and during the descend leg (C) compared against the radiosonde measurements. Similarly to the temperature measurements, the descend leg agrees better with the radiosonde measurements than the ascend leg. A dry bias is visible in both legs of the flight, and especially in the ascend leg and at the lower end the bias is strong. The minimum humidity measured by the radiosonde is 69 %. During the ascend leg the minimum humidity is 63 % and during the descend 65 %. For all of the measurements the maximum humidity is 100 % when measured inside a cloud. The mean humidity for radiosonde measurements is 86 %. For the ascend leg the mean measured humidity is 85 % and for the descend leg 86 %. The standard deviations for the radiosonde, ascend leg and the descend are 8 %, 10 % and 9 %, respectively. The RMSE for the humidity measurements are 3.0 % for B and 2.1 % for D.

4.3 Outliers

As mentioned in the previous chapter, data points lying outside the outlier range were taken under consideration separately. The measured profiles with outliers were studied separately in order to find out the reasons for the differences and to justify their removal from the statistical analysis.

For the temperature, there were 13 profiles with outliers in them. The analysis of the temperature outliers indicates three different circumstances where the outliers are often present. First of these is the inversion layers. One example of an inversion layer was already presented earlier in the case studies (case 2). Another example is given in the figure 28. In this measurement an inversion layer is visible between 325 m and 400 m in the ascend leg and between 280 m and 330 m in the descend leg. During the ascend leg the temperature at the bottom of the inversion layer is 12.6 °C and 14.5 °C at the top of the layer. During the descend leg the temperature at the bottom of the layer is 12.7 °C and 14.9 °C at the top of the layer. In this case the difference in the height of the layer between the legs is evident, with the bottom of the layer being 45 m lower during the descend phase and the top being 70 m lower. The inversion layer also appears to be thicker during the ascend leg. The in the temperature within the layer reaches -2.3 °C at highest, and it starts to deviate after 300 m, after the descending leg detects the layer bottom.

Another measured profile with an inversion layer can be seen in figure 29. In this case a low-level cloud is located below the inversion layer. The presence of cloud is indicated by the humidity profile, where the relative humidity inside the cloud is 100 %. The height of the cloud top is around 282 m when measured with the radiosonde, around 360 m during the ascend leg and 341 m during the descend leg. These heights are indicated in the figure by gray horizontal curves. The red curve indicates the measurements in ascend leg, the blue curve the measurements in descend leg and the black dotted curve indicates the radiosonde measurements.

The variation between the radiosonde and the drone flight legs is likely due to the temporal difference of around 20 min between the radiosonde measurement and the drone flight. Correspondingly the radiosonde detects the inversion layer at lower altitude. The smaller difference between the ascend leg and the descend leg can likewise be caused by the temporal difference of the measurements, or by the drone pushing the air downwards during the descend leg. At the top of the cloud and right below the inversion layer, the temperature measured with radiosonde is 11.8 °C. For the ascend leg this temperature is 12.0 °C and for the descend leg 12.2 °C. Inside the inversion layer the temperature peaks at 14.2 °C when measured with radiosonde, and at 14.1 °C for the descend leg measurements. Measurements during the ascend leg don't show any definite peak, but rather increase to 12.5 °C at the top of the profile.

In this profile the inversion layer is well detected by the radiosonde and the descend leg as seen in the, but the ascend leg doesn't detected the rise in temperature within the

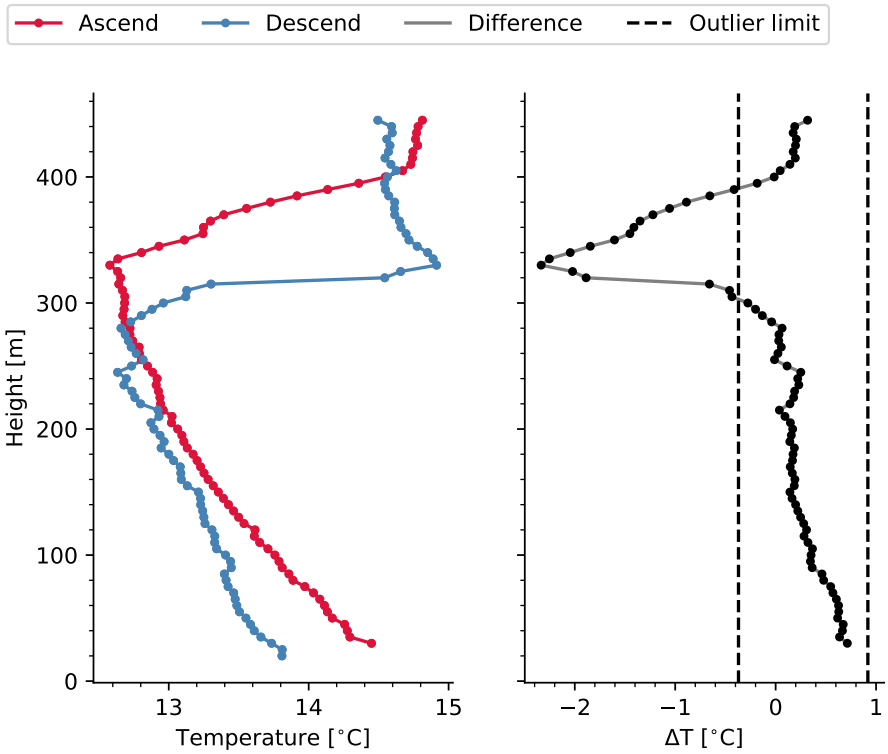

Figure 28. *An example of a measured profile with an inversion layer. This profile was measured at 04.09.2019 at 08.08 UTC. The profiles on the left show the measured temperatures in ascend leg (red) and descend leg (blue). The profile on the right shows the difference between these two profiles and the limits for the outliers. The dashed black curves indicate the limits used for the outliers. The dots on the profiles indicate the measurement points.*

inversion layer. The reason for this could be the humidity condensed on the temperature sensor: when ascending through the cloud the water vapour in the saturated air condenses on the surface of the sensor. Then after emerging from the cloud into the dryer air, the water droplets from the surface begin to evaporate. Since this process requires energy, the evaporation lowers the temperature of the sensor. This causes the temperature measured to be lower than the actual ambient temperature inside the inversion layer. During the descend leg the sensor would have dried already, measuring the temperature correctly. This effect is also a source of error in radiosonde measurements, when the sensor can get wet inside a cloud (Immler *et al.* 2010). Similar effect was also observed, though less pronounced in other profiles with cloud presence. In some cases this effect was observed at the lower part of the profile, when the cloud exits the cloud during the descend leg. Then the temperature difference at the lower part of the profile was higher than usually, likely due to the wetting of the sensor inside the cloud during the descend leg.

The second type of outlier was related to the top or bottom of the profile. At the top of the profile the drone turns around and begins the descend, and in some cases high differences in temperature can be noticed in this phase. This could be due to the thermal wake of the drone. When the drone turns around and begins the descend, at the beginning

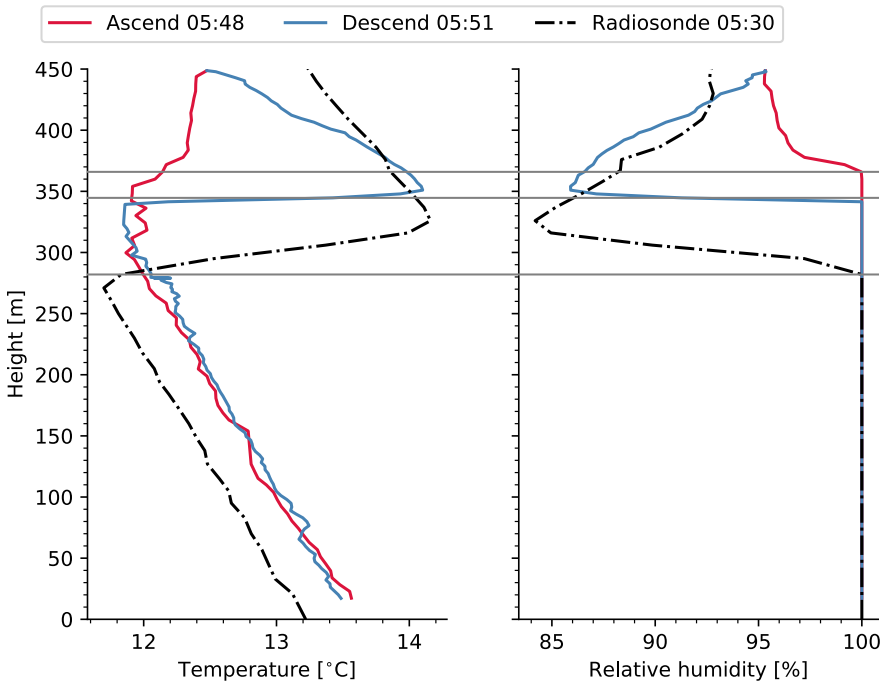

Figure 29. *Another example with an inversion layer above a cloud. The red curve indicates the measurements taken during the ascend leg, the blue curve the measurements taken during the descend leg and the black dashed curve the radiosonde measurements. The gray curves indicate the cloud top heights when the relative humidity falls below 100 %.*

it is essentially measuring this warmer air which did not cool down before the second measurement. This effect has also been observed in radiosonde measurements where the warm bias is caused by the thermal wake of the balloon. An example of this type of outlier can be seen in figure 30. In this profile a higher difference can be seen at the top of the profile, where the difference is $-1.5\,^{\circ}\mathrm{C}$. Otherwise at the lower heights the difference stays within the limits.

In figure 31, the top of the profile is presented in more detail. In this figure the data is not interpolated but rather taken directly from the measurements. To gain a better understanding of the temporal and spatial evolution of the temperature at the top of the profile, only data between 430 m and the top of the profile 449 m is shown. The time series of the measurements is shown on the top, and the height profile is shown at the bottom. Here it should be noted that unlike in other figures, the height is now shown at the x-axis rather than the y-axis to make it easier to compare with the time series. Here the ascend leg is plotted in red, the decending leg in blue and the measurement points with black dots. For comparison, the interpolation points are indicated at the figure (B) with black vertical curves. The time is shown in seconds from the beginning of the flight. The higher temperature after the flight switches from the ascending leg to the descending leg is evident. From the time series the turning point can be seen at 146 s, and the temperature starts to increase right before it. In the height profile this

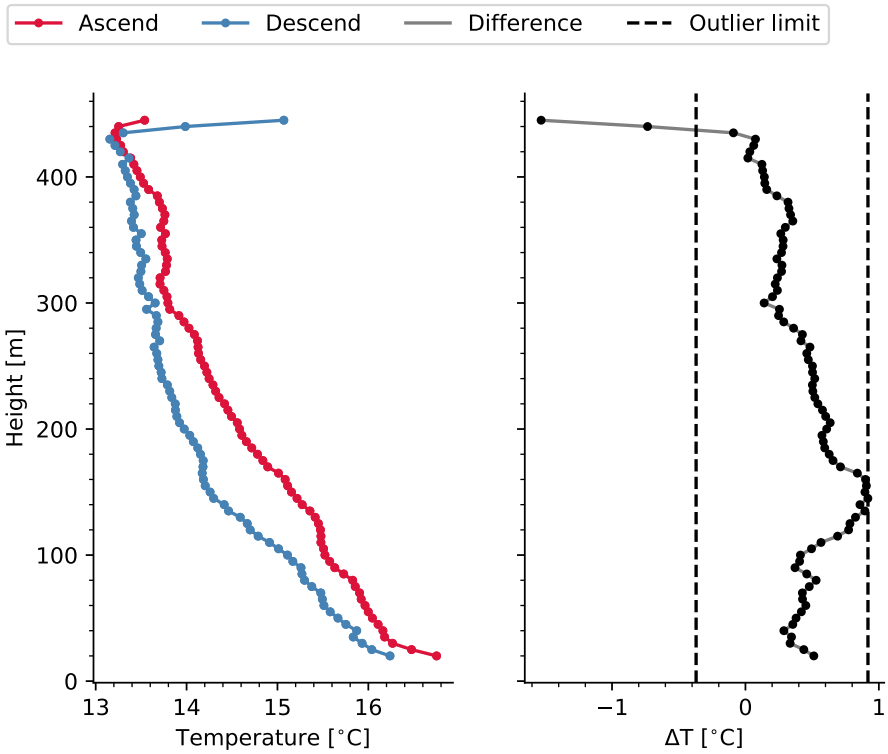

Figure 30. *An example of a measured profile with high difference on top of the profile. This profile was measured at 04.09.2019 at 08.08 UTC. The profiles on the left show the measured temperatures in ascend leg (red) and descend leg (blue). The profile on the right shows the difference between these two profiles and the limits for the outliers. The dashed black curves indicate the limits used for the outliers. The dots on the profiles indicate the measurement points.*

corresponds to 449 m. The increase in temperature before the turning point could be caused by the data logging frequency. The data is only logged every 2 s, and thus it is possible that what here is marked as the top of the profile is actually already on the descending leg. At 150 s the temperature peaks at 15.1 °C. At this time the corresponding height is approximately 445 m. At 158 s, corresponding to height just below 435 m the temperature anomaly seems to be over and the temperature is 13.2 °C.

Third outlier case is related to the very beginning of the flight, when the drone begins the ascend leg. An example profile for this case is presented in figure 32. In this profile the higher temperature difference is evident at the bottom of the profile, where the difference at the lowest point is 1.1 °C, and quickly decreases to approximately 0.5 °C. Since the drone is initially inside the ground station (see figure 7), and the temperature inside this station can be higher than the ambient temperature, the measured temperature at the lower part of the profile during ascend leg can be higher than actual ambient temperature.

For a more detailed analysis of the temperature evolution at the very beginning of the profile, the measured profile without the interpolation is studied. The time series for the first 23 s can be seen in figure 33. The dashed gray curve indicates the temperature measured at the ground level, the orange curve the drone measurements and the black dots are the

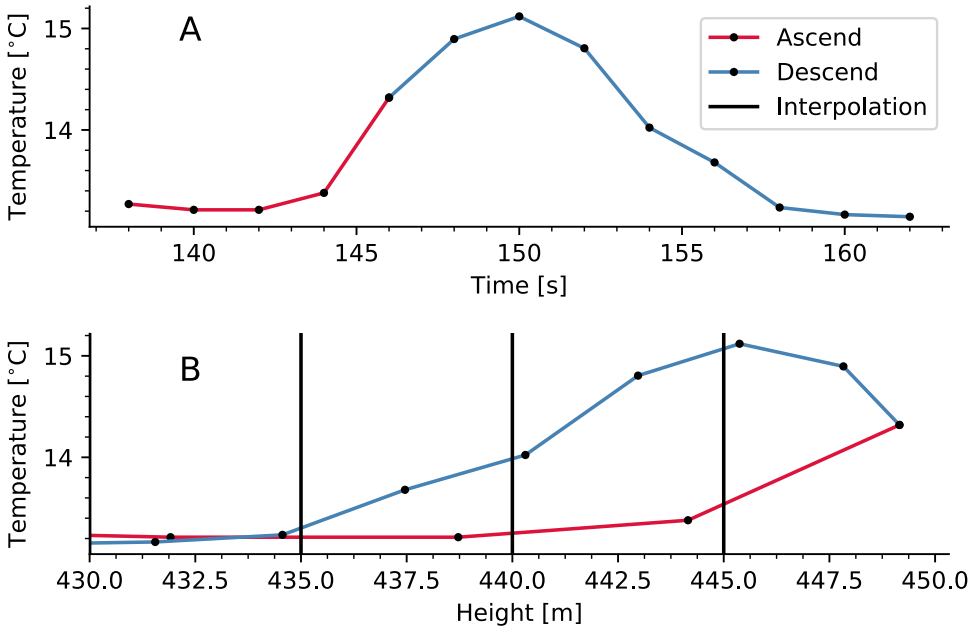

Figure 31. *Time series and the height profile of the temperature measurement at 04.09.2018 at 10:20 UTC. The figure on the top (A) shows the time series for the measurement with and the figure on the bottom (B) shows the height profile. Note that in this figure the height is placed on the x-axis, unlike the other figures where the height is at y-axis. The red curve shows the measurement at the ascend leg, blue curve the measurement at the descend leg, black dots indicate the measurement points and the black vertical curves in the figure (B) show where the interpolation points. The time in figure (A) is from the beginning of the flight.*

times when the measurements have been logged. The green curve indicates the vertical velocity of the drone with the black asterisk indicating measurement points. The ticks on the top of the figure indicate the heights where each of the data points are measured and the black vertical curve the time when the drone takes off at 3 s. The measurements prior to this time are taken inside the ground station. Here it can be seen that the temperature inside the station is clearly higher than the temperature measured outside. The outside temperature is 18.4 °C, while inside the station the temperature oscillates between 19.0 °C and 20.2 °C before taking off. After this the temperature drops as the drone begins the ascend. At the beginning the ascend velocity is lower, starting at 2.5 $\mathrm{m\,s^{-1}}$ and decreasing to almost 0 $\mathrm{m\,s^{-1}}$ at 13 s mark. After this the velocity sharply increases and the temperature starts to decrease more rapidly. Eventually at 18 s mark the ascend velocity settles to the value of 3 $\mathrm{m\,s^{-1}}$. Here the temperature can be seen to be very sensitive to the changes in the vertical velocity. This can be one reason for the higher differences in measured temperatures between ascend and descend legs.

Lastly, there were measurements where the outliers were attributed to the turbulence and small scale temporal changes of the atmosphere. An example of such a case is presented in figure 34. In this figure an outlier is detected at 85 m, 410 m, 420 m and 435 m. When

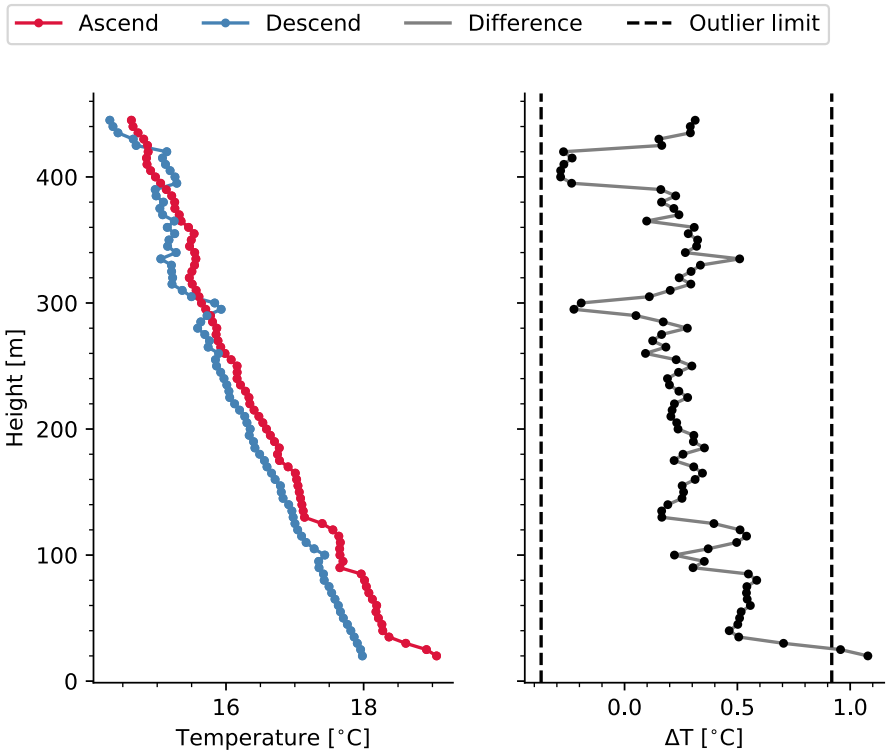

Figure 32. *An example of a measured profile with high difference on top of the profile. This profile was measured at 04.09.2019 at 12.35 UTC. The profiles on the left show the measured temperatures in ascend leg (red) and descend leg (blue). The profile on the right shows the difference between these two profiles and the limits for the outliers. The dashed black curves indicate the limits used for the outliers. The dots on the profiles indicate the measurement points.*

looking at the temperature difference profile and comparing the profiles during the ascend and descend legs, it can be seen that the temperature measured during the descend leg oscillates more than the temperature at the ascend leg which decreases almost monotonically. This oscillation causes the high variation observable in the difference profile, and some of these data points end up outside the outlier limits. While the exact cause for these remaining outliers are not known, they can possibly be attributed to the variability of the atmosphere itself and partly due to lower vertical velocity during the descend leg.

If the temperature varies rapidly the different resolution during the ascend leg (3 m vs 1 m during the descend leg) may not be sufficient for detecting this change. Especially in figure 34 the temperature varies rapidly just above 400 m. This variation could also be partly attributed to the low wind speeds: for the measured profile the mean wind speed between 40 m and 160 m, the range measured by the windcube, is only $1.7\,\mathrm{m\,s^{-1}}$. The reasoning for this is that with low wind speed the air flow around the sensor would be dominated by the turbulent air flow coming from the rotors, which can cause the high variations. With higher wind speed the wind would dominate the air flow and possibly flush away the warmer patches of air caused by the turbulence. However, since the availability of the wind speed data is limited, this hypothesis is difficult to enforce without additional

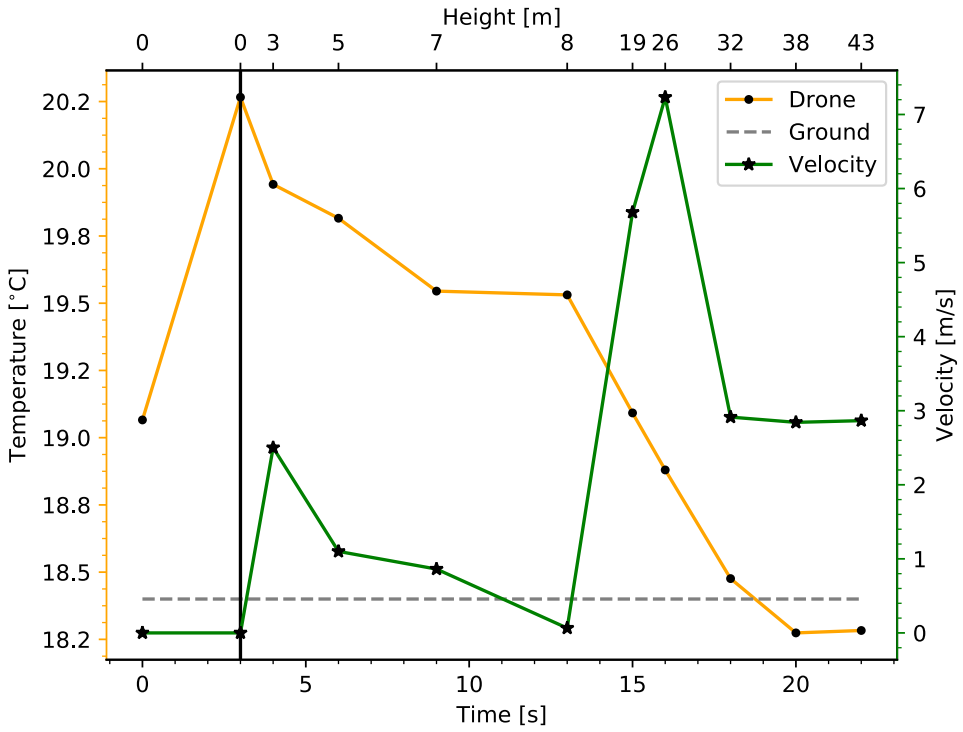

Figure 33. *A time series of the temperature and the velocity of the drone at the beginning of the ascend leg measured at 04.09.2018 12:35 UTC. The orange curve indicates the measured temperature, green curve the velocity and the black dots and asterisks indicate when the measurements have been logged. The axis at the top indicates the heights where the measurements have been logged. The dashed gray curve indicates the temperature measured at the ground level and the black vertical curve the time when the drone begins the ascend.*

measurements.

As a summary, out of the 13 profiles measured with outlier cases, 5 had an inversion layer causing the outlier, 3 cases had differences related to the top of the profile when the drone ends the ascend leg and begins the descend, 1 case had the difference caused at the very beginning of the ascend leg and 2 cases had the differences attributed to the small scale changes in the atmosphere or the high variation of the temperature profile on the descend leg. The 2 cases left had also cloud presence when the measurements were taken, which causes the wetting of the sensor and leads to temperature differences when the sensor is dry during one leg and wet during the other. In these two cases the difference was observed at the lower part of the profile. In these cases the cloud was high enough so that the drone did not exit the cloud at the top of the profile, but rather exited the cloud at the bottom.

It seems that the inversion layers are the most common cause for these outliers in the differences. In these the difference can also be seen very clearly, whereas in some cases it may be debatable if the difference actually should be classified as an outlier or not.

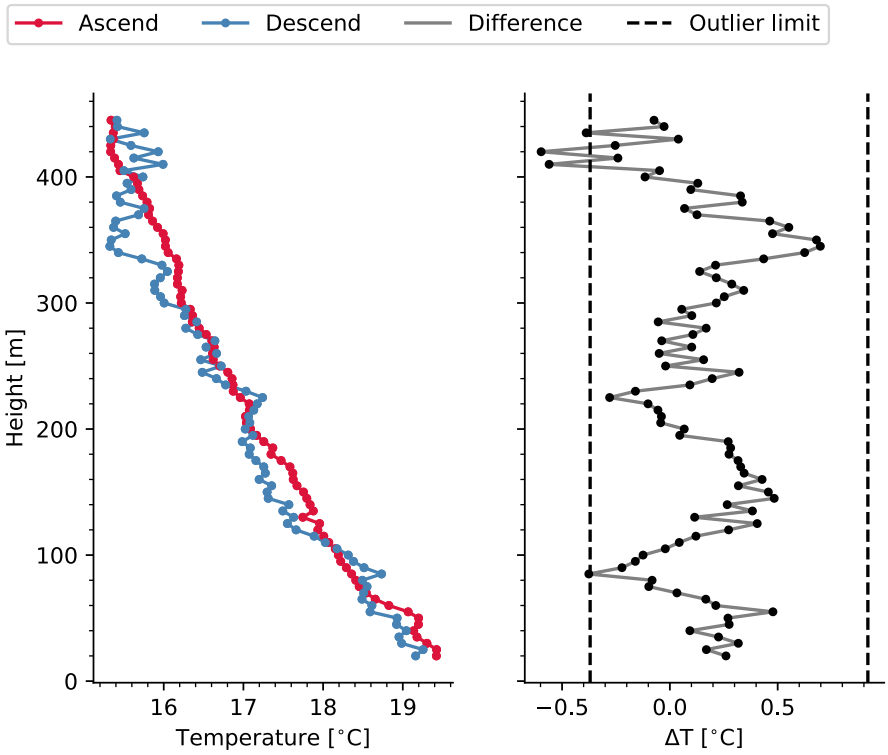

Figure 34. *A profile with temperature anomaly likely caused by small changes of the atmosphere measured at 07.09.2018 07:49 UTC. The profiles on the left show the measured temperatures in ascend leg (red) and descend leg (blue). The profile on the right shows the difference between these two profiles and the limits for the outliers. The dashed black curves indicate the limits used for the outliers. The dots on the profiles indicate the measurement points.*

The outliers in the humidity measurements were often related to the outliers in the measured temperature. This is due to the humidity correction (equation 37), which depends on the measured ambient temperature. If there is a high difference in the measured temperature, the correction propagates this difference also to the corrected humidity profiles. An example of this can be seen in figure 35. Here the red curve indicates the measurements taken during the ascend leg, and blue curve the measurements taken during descend leg and the black dashed curves the differences between these measurements. The profile on the left is the humidity profile and the profile on the right is the temperature. Here a higher difference in the measured temperature is observed at above 300 m. At the same height a higher difference in the humidity profile is also observed. Similarly at the lower part of the profile, around 100 m a higher difference is observed in temperature, leading to higher differences in the humidity profile.

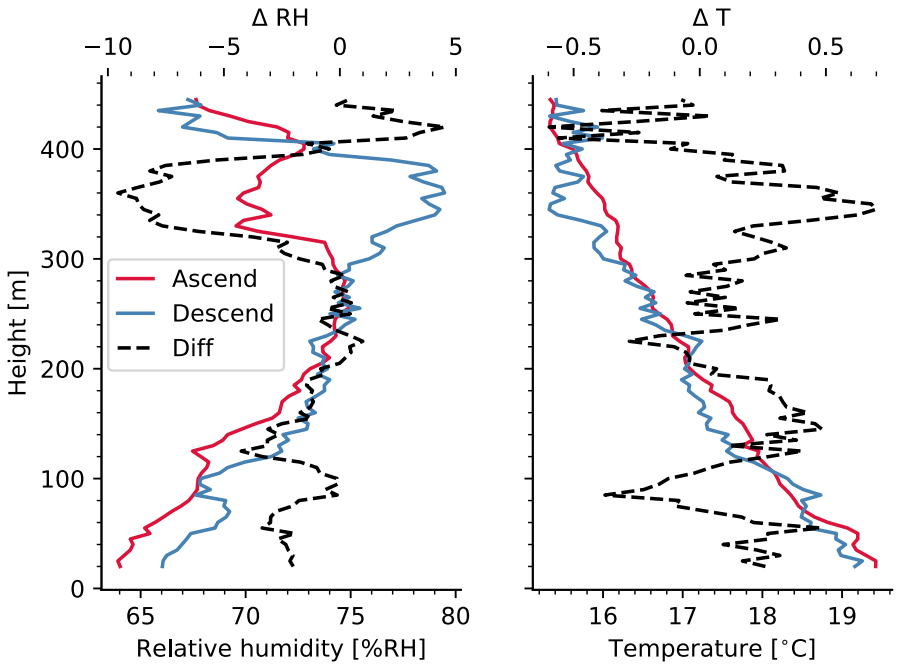

Figure 35. *The humidity (left) and temperature (right) profiles measured on 03.09.2018 beginning at 07:47 UTC. The red curves indicate the measurements taken during ascend leg, the blue curves the measurements taken during descend leg and the black dashed curve the difference.*

4.4 Radiation correction

The difference of 0.26 °C in temperature was observed before applying the correction equation for radiation (equation 39). Since the radiation correction depends on the ventilation speed v at the sensor, and the ventilation speed during the ascend and descend legs are different due to different vertical velocities and the shielding the drone, could this be the explanation for the observed difference?

To correct the effect of the solar radiation, the ventilation speed at the sensor has to be estimated. This in turn depends on the vertical and horizontal velocities of the drone as well as the wind speed, as explained in section 3.4. Since the wind speed data is available only at the heights between 40 m and 160 m from the windcube, or from the radiosoundings in those measurements that are temporary sufficiently close to the radiosonde measurements, the correction can only be applied to these measurements points or the effect of the wind speed has to be ignored. The latter is not a good option, since the inverse relationship between the ventilation speed and the temperature correction causes the correction to be unreasonably high if the ventilation speed is too small. Since this correction was derived between wind speeds 2.5 $\mathrm{m\,s^{-1}}$ and 5 $\mathrm{m\,s^{-1}}$, this equation should not be used below this range. Thus, the first thing to consider is how significant the wind speed is on the total ventilation speed. For this a distribution of how the wind speed contributes to the total ventilation speed from the existing wind speed data can be seen in figure 36. In this figure the contribution of the wind speed is defined as $\frac{u^2}{v^2}$, where u is the wind speed and v is

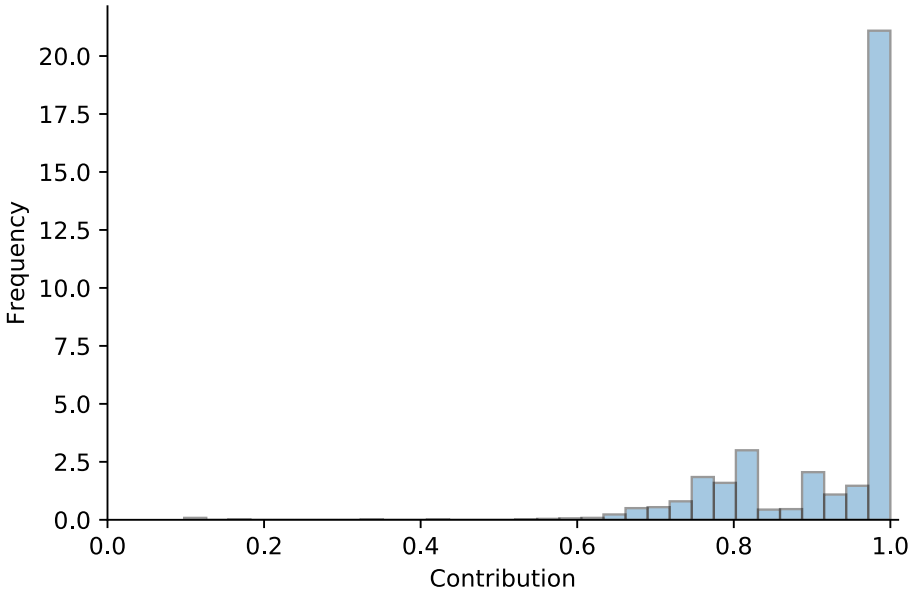

Figure 36. *A distribution to show the contribution of the wind speed to the total ventilation. The scale on the x-axis goes from 0 (no contribution) to 1 (the only component contributing).*

the total ventilation speed calculated with the equation 42. As it can be seen from the figure, in almost all of the cases the major contribution (> 0.6) to the ventilation speed is attributed to the wind speed. Thus it is clear that the wind speed cannot be ignored when calculating the radiation correction, and this correction can only be applied to the measurements that have wind speed data available.

Applying the radiation correction to the data that has wind speed available, the magnitude of this correction can be estimated. Especially when we want to know if observed difference between the ascend and descend legs can be attributed to the radiation correction, we should take a look at the difference between the temperature error ΔT between the legs. Since the ventilation speed depends on the vertical velocity which is different between the legs, the correction should also be different. Thus if the actual ambient temperature is T, the temperature error during the ascend leg is ΔT_a and the temperature error during the descend leg is ΔT_d, the measured temperatures during the ascend and descend legs (T_a and T_d, respectively) are

$$T_a = T + \Delta T_a \tag{58}$$

$$T_d = T + \Delta T_d \tag{59}$$

and thus the difference between the ascend and descend legs is

$$T_a - T_d = \Delta T_a - \Delta T_d. \tag{60}$$

If this quantity is equal to the differences observed between the ascending and descending leg, it would give us strong evidence that the radiation error is indeed the source for the

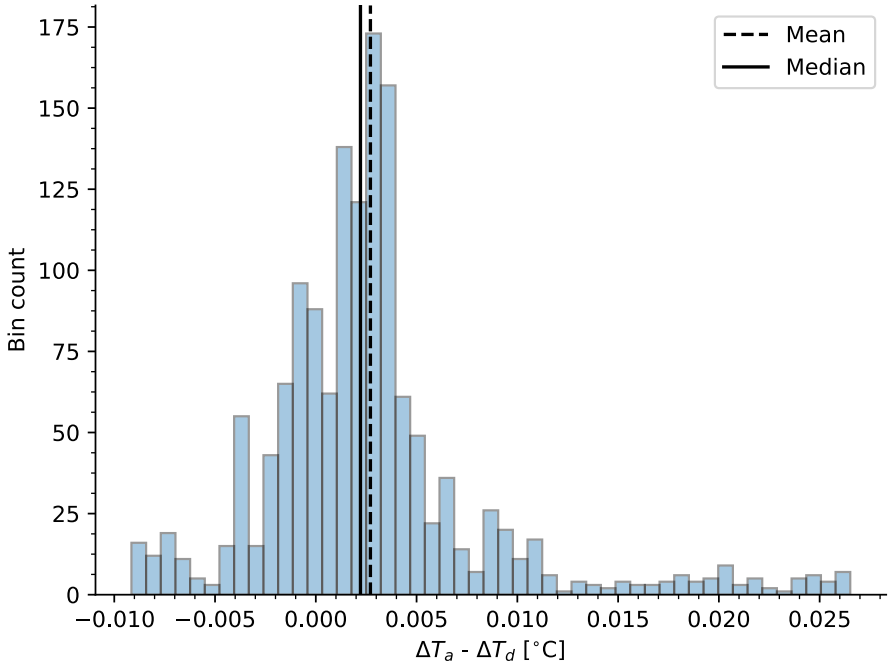

Figure 37. *A distribution to show the difference between the radiation corrections applied to the ascending and descending legs. The mean is indicated with a dashed black curve and the median with a solid black curve.*

warm bias on the ascending leg. In order to test this, the radiation correction was applied to the data with wind speed data available. Then the difference between the corrections for the ascend leg and the descend leg was calculated. The distribution for this difference is visualized in figure 37. A quick visual comparison with the temperature difference distribution (A) in figure 22 shows that the difference range is more than order of magnitude smaller. The mean difference for the radiation correction is 0.003 °C and the median 0.002 °C with the maximum difference being 0.027 °C. It is rather easy to see that the radiation correction can not cause the observed differences during the two legs of the flight. This can also be confirmed using the t-test (with hypothesis H_0: $T_a - T_d = \Delta T_a - \Delta T_d$), with the p-value being much lower than the chosen limit 0.05. Furthermore the radiation correction at the measured altitudes can be considered to be negligible, and the comparison of the measured data without the applied correction is reasonable. Finally, keeping in mind that the correction equation was originally derived for the older temperature sensor used in Vaisala RD92 dropsonde, and the fact that the new sensor should have even smaller solar radiation error, the true error caused by the solar radiation and the correction is likely smaller than what has been estimated here.

4.5 Effect of wind speed

If the assumption that the higher temperatures measured during the ascend leg are caused by the heat convected from the drone to the sensor, we would expect to see some correlation in the temperature difference and the wind speed. If the heat is convected from the drone itself to the sensor, the airflow around the sensor should mix the air more effectively, reducing the convection of heat and lowering the difference between the ascend leg and the descend leg. In order to investigate this effect, the temperature difference was compared against the wind speed to see if a correlation exists. This comparison can be seen in figure 38. Only cases with wind speed higher than $5\,\mathrm{m\,s^{-1}}$ were taken. Below this the data was clustered and there was no correlation. Three cases were available for the analysis with sufficient wind speeds. Measurements from the flights at 07.09.2018 at 05:36 UTC, 11.09.2018 at 12:43 UTC and 12.09.2018 at 08:00 UTC, indicated with the different colours of the markers. The black dashed curves indicate the linear fit to the data, with each measurement having the linear fit separately. From the figure it can be seen that the first measurement case contradicts the hypothesis, with positive correlation between the wind speed and the temperature difference. For this case the correlation coefficient is 0.49, indicating a weak but existing correlation. For the other two cases the correlation is stronger with correlation coefficients of -0.71 and -0.76, respectively. For these cases the correlation is also negative, as predicted. During the first case with positive correlation, it is possible that the wind speed is still not high enough to have any effect. Also the low correlation coefficients indicates this. The two other cases seem to indicate that there is

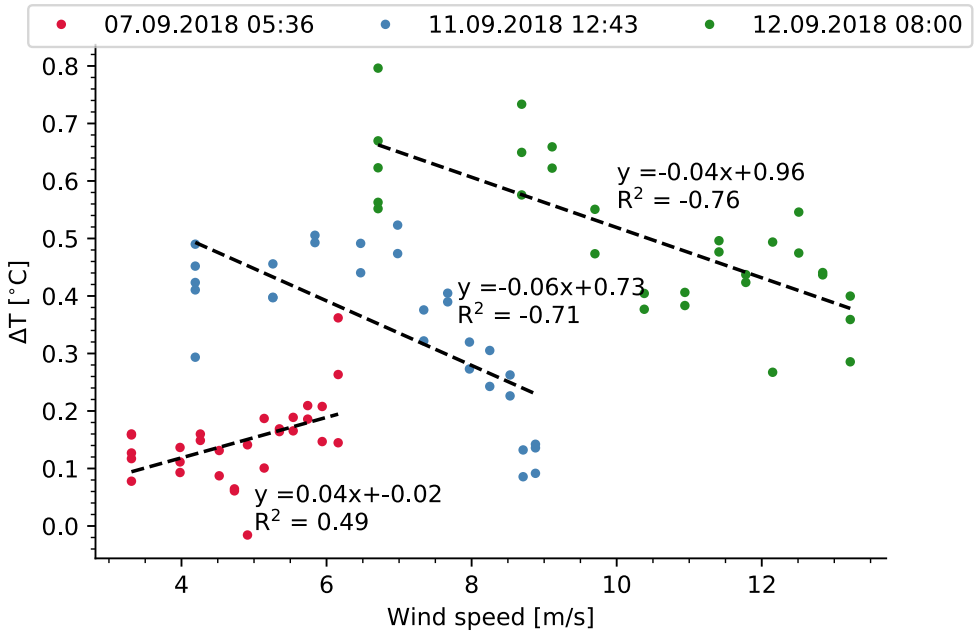

Figure 38. *The temperature difference plotted against the wind speed. The different colors of the markers represent the different measurement cases, and the black dashed curves the linear fit to the data.*

indeed a negative correlation between the wind speed and the temperature difference, as predicted.

4.6 Hovering phase

To better understand the convection of heat from the drone, the drone was kept hovering at a stationary height for longer time. This allows the investigation of the temperature evolution below the drone where the sensor is located. The drone was hovering stationary at a height of approximately 9 m for 218 s, and the temperature was measured during this time. The measurements were taken on 05.09.2018 08:23 UTC. This phase is plotted in figure 39.

The black solid curve indicates the time 0, when the hovering phase begins, the blue curve is the temperature measured by the drone with black dots indicating the measurement points, and the black dashed curve is the measured temperature at ground level. At time < 0, the drone was descending to the hovering height. The boxplot on the right-hand side represents the distribution of the temperature measured during this period. In the boxplot and the time series, a high variation in the measured temperature can be seen. While the median measured temperature is 16.0 °C, the maximum temperature is 16.8 °C and the minimum temperature is 15.7 °C. The standard deviation for the temperature is 0.2 °C. When compared to the ground temperature, the variance in the measured temperature with

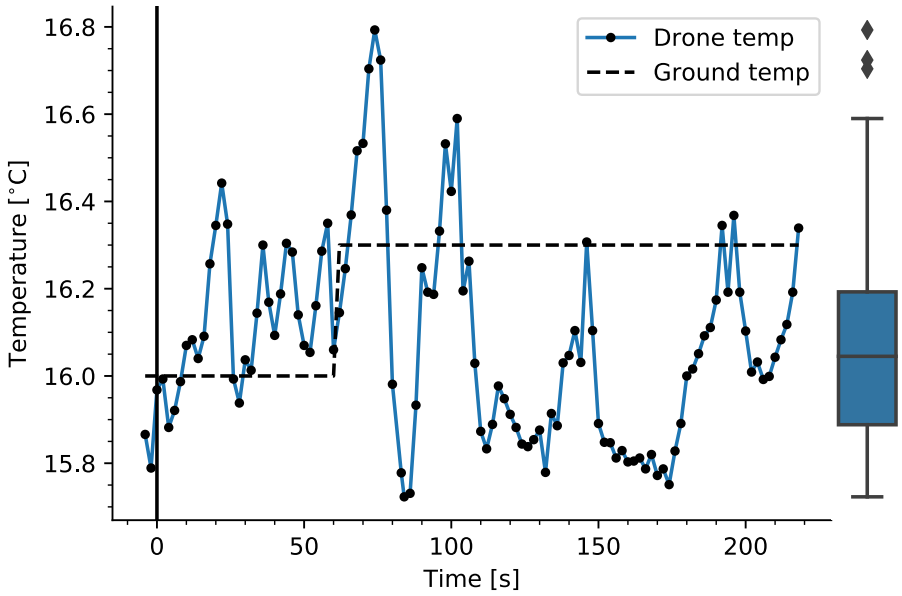

Figure 39. *The measured temperature while hovering at a stationary height. The blue curve indicates the drone measurement with the black dots indicating the measurement points, the black dashed curve indicates the temperature measured at ground level and the black solid curve the time when the hovering phase starts. The boxplot on the right-hand side represents the distribution of the measured temperatures.*

drone seems too high to be caused by changes in the atmosphere itself. The variance is also too high to be the electrical noise. It seems that the heat convected from the drone can be highly variable and the air flow around the sensor is turbulent. Especially rapid changes in temperature happen after 60 s, when the temperature rapidly changes from 16.1 °C to the maximum temperature of 16.8 °C in the span of 14 s, then decreases to the minimum of 15.7 °C in the span of 10 s. Also before the 60 s mark the temperature measured by the drone seems to be generally above the temperature measured at the ground level, but afterwards the temperature starts to oscillate and after 104 s oscillates less and settles below the temperature measured at the ground. The temperature measured at the ground level is 16.0 °C until 62 s mark, and afterwards increases to 16.3 °C.

It seems that while the drone is hovering above a fixed location without sufficient ventilation available at the sensor, the temperature behaviour can vary strongly. Similar behaviour was observed by Greene *et al.* (2019) where the temperature varies strongly while hovering the drone at fixed height. However, the temperature seems to behave better during the flight, which indicates that the airflow is steadier when the drone is not hovering at a fixed height. Thus, for the measurements of the temperature it is beneficial and even necessary to maintain a steady vertical velocity in order to minimize the turbulence and acquire better measurements.

4.7 Calibration

Here a simple calibration method for the temperatures measured during the ascend leg is proposed. The underlying assumption for the calibration is that the descend leg measures the correct temperature, and the ascending temperature is calibrated based on that. The calibration is simply taken to be the mean temperature difference between the ascend and descend legs and this temperature is then subtracted from the temperature measurements taken during the ascend leg. Thus if T_a is the temperature measured during the ascend leg and $\overline{\Delta T}$ is the mean difference observed between the legs, the calibrated temperature T_{ac} would be

$$T_{ac} = T_a - \overline{\Delta T}. \tag{61}$$

This calibration assumes that the temperature difference is constant in all measurement conditions. While this assumption may not be completely satisfied, the calibration seems to work well. In figure 40 the results for the calibration are presented. The black solid curve indicates the diagonal, the black dashed curve indicates the linear fit to the calibrated temperature and the red dashed curve indicates where the linear fit for uncalibrated temperature would be. For the calibration the dataset was randomly split into two groups: 70 % of the dataset was used for calculating the mean difference and the calibration was applied to the remaining 30 % of the data.

From the comparison it can be seen that the calibration brings the data closer to the diagonal, and the linear fit to the data also agrees well with it. The mean difference for the calibrated temperature is 0.02 °C and the median is 0 within all the significant digits. The

standard deviation is still 0.22 °C, which is expected since the calibration does not change the shape of the difference distribution. The root mean squared-error for the calibrated temperature is 0.22 °C, which is less than the RMSE of 0.35 °C for the uncalibrated data. The linear fit fort the calibrated temperature gives the slope of 1.02 and the intercept at −0.33 °C. As the calibration only subtracts a constant from every measurement, it does not change the slope of the fit, but the intercept point moves from −0.07 °C to −0.33 °C. Also the r-value is 0.99 for both fits, indicating a good agreement between the temperatures measured during the descend leg and the calibrated temperature. This is a good indication that the this simple calibration for the temperature measurement can reduce the temperature difference between the legs and can be used to retrieve the actual temperature from the temperature measurements during the ascend leg.

Figure 41 shows an example of a measured temperature profile and the temperature differences, with the calibration applied. In this figure the dashed red and blue curves indicate the measurements taken during the ascend and descend leg, respectively. The solid red curve indicates the calibrated temperature for the ascend leg. The black solid curve indicates the difference with the calibration applied and the dashed black curve without the calibration. As can be seen from this figure, the calibration causes the difference to be slightly negative instead of positive, but closer to 0. For this profile, the mean difference without the calibration applied is 0.16 °C and with the calibration applied the mean dif-

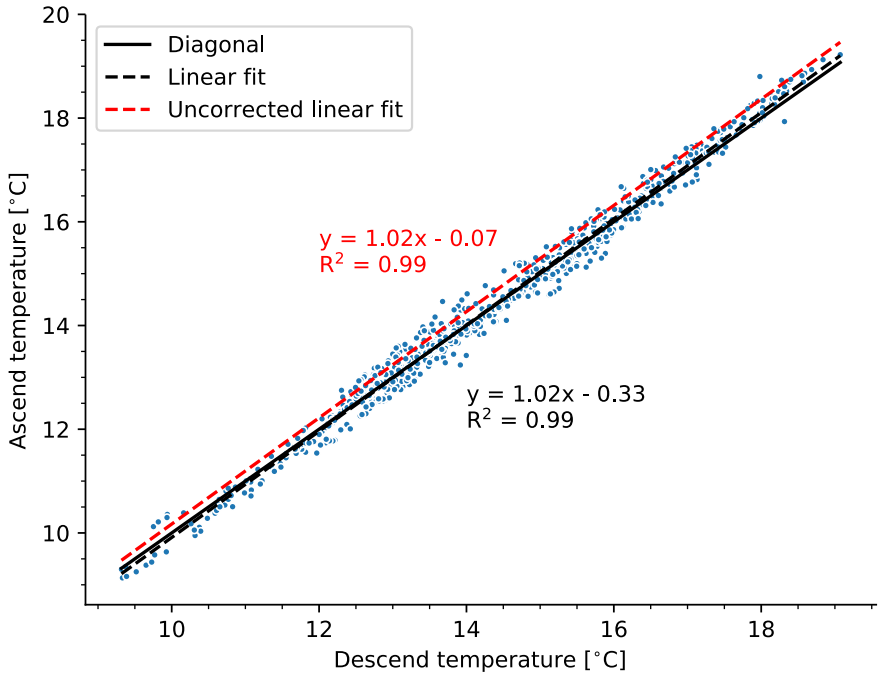

Figure 40. *Comparison of the calibrated temperatures for the ascend leg and the temperature measured during the descend leg. The black solid curve indicates the diagonal, the black dashed curve the linear fit to the data and the red dashed curve indicates where the linear fit for the uncalibrated temperature would be.*

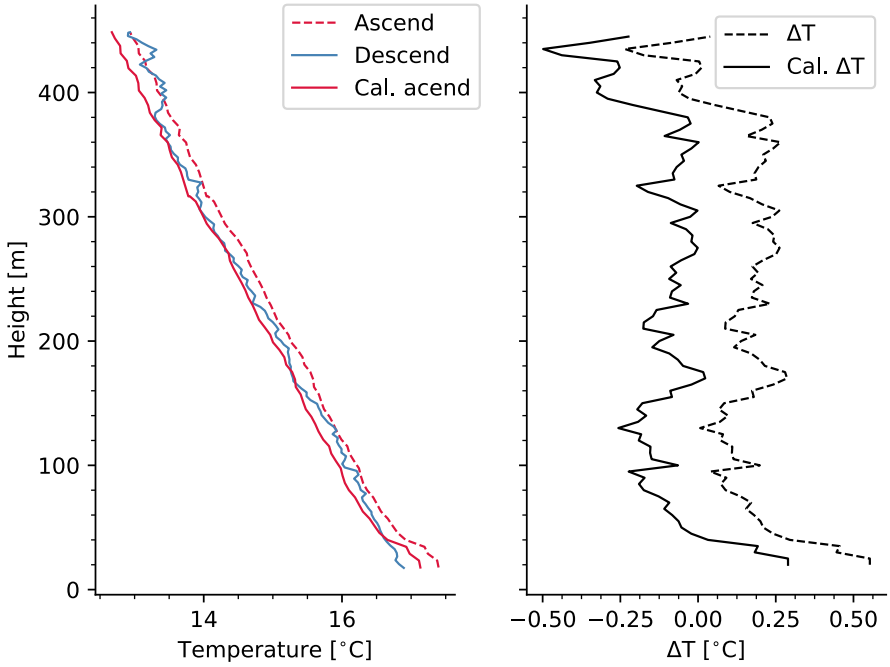

Figure 41. *Temperature profile with calibrated temperature during ascend leg on the left and the temperature difference profile on the right. Measurements taken on 05.09.2018 at 12:26 UTC. The dashed red curve indicates the ascend temperature, the dashed blue curve indicates the descend temperature and the solid red curve the calibrated ascend temperature. The black dashed curve indicates the temperature difference without the calibration and the solid black curve with the calibration.*

ference is −0.11 °C. The standard deviation for the differences is 0.13 °C. After applying the calibration the ascending leg agrees generally better with the descend leg. However in few regions, especially at the top of the profile above 380 m, the descend leg agrees better with the uncalibrated temperature. This could be caused by the warm wake of the drone at the top of the profile as explained in section 4.3, corresponding to the second outlier type. Another explanation is simply small scale variations of the atmosphere itself, corresponding to the last outlier type.

5. CONCLUSIONS AND OUTLOOK

In this thesis an analysis of the drone-borne vertical profiles of temperature and humidity during the ascending and the descending legs of the flight are presented. The statistical analysis accompanied by individual case studies was conducted In addition cases with distinctly larger differences between the ascend and descend legs in the measured profiles were analyzed in more detail in order to explain the reasons for the observed differences. Collocated radiosonde measurements were used as a reference measurements. The most important findings are:

1. The descending leg of the flight agrees better with the reference measurements than the ascending leg of the flight.
2. A warm bias in the measured temperature and a dry bias in the measured humidity were observed in the ascending leg compared to the descending leg.
3. Inversion layers are often detected at lower altitude during the descend leg than the ascend leg.
4. The wet-bulbing effect when the drone emerges from inside a cloud can lead to lower measured temperatures.

The temperature difference between the drone measurements and the radiosonde is likely caused by the heat convected from the drone to the sensor. This convection would happen when the parts of the drone heat up and warm the air around it. Especially the motors, which are located in the middle of the rotors, are heating up significantly during the flight and warm the air around them. This air gets pushed downwards below the drone, causing the warmer air to be measured by the sensor. This would also explain why the difference is higher during the ascend leg. Since the drone is shielded by the airflow during this leg, the warmer air from the drone gets less diluted before the measurement. During the descend leg the airflow caused by the vertical movement likely mixes the air and causes the temperature difference to be lower.

For the humidity measurements, differences in the ascend and descend leg are expected already due to the humidity correction in equation 37. Thus, if the measured temperatures different this inevitably leads to different humidities after the correction, even if the humidity measurement itself would be correct. Thus it is important to have accurate measurements of the ambient temperature in order to also accurately correct the humidity.

Also the effect of the solar radiation on the measured temperature was corrected in order to determine if this could be the source of the difference between the ascending and descending legs. However, the magnitude of the solar radiation error is much smaller than

the observed difference between the two legs, and thus can not be the sole source of error. In addition, the solar radiation error was found to be insignificant, and thus justifying the use of uncorrected data for the statistical analysis.

The effect of wind speed on the observed temperature difference was investigated. At small wind speeds no clear correlation was found, but in few cases when the wind speed was above $6\,\mathrm{m\,s^{-1}}$ a negative correlation between the temperature difference and the wind speed was found. This agrees with the assumption that the difference should decrease with increasing wind speed. However only two cases and handful of measurement points were available for this study. Still this indicates that the wind speed does reduce the temperature difference.

To characterize the behaviour of temperature when the drone is hovering at a fixed height, the temperature measurements were taken during the hovering phase. While letting the drone hover for around 3 minutes at height of 9 m, the temperature below the drone was measured. The results for this show high oscillation in the temperature, indicating that the air flow around the drone is highly turbulent.

The results of this work indicates that drones are capable of accurate vertical profiling. For temperature and humidity, measurements taken during the descending leg are recommended since they agree better with the reference measurements. If the ascending leg is also used, the measurements should be calibrated using the method presented in section 4.7. For the measurements taken during the ascend leg, the higher uncertainty should be then taken into account. Furthermore the correction of the humidity measurements using the equation 37 is necessary.

For future measurements, the placing of the sensor should also be considered. It would be beneficial to place the sensor farther away from the drone itself, reducing the effects of the drone on the measurements. Especially the sensor should be placed away from the drone in vertical direction in order to reduce the effects caused by the rotors and to allow sufficient air flow around the sensor. Furthermore the vertical placement of the sensor would likely reduce and possibly eliminate the differences observed between the ascending and descending legs, allowing accurate measurements during both legs.

The benefits of drone measurements also include different and predetermined flight paths, which are not possible with weather balloons. Especially for multi-rotor drones this is an advantage, since they can be more easily controlled than fixed-wing drones, being able to go straight up or down without need for vertical movement. Yet a sufficiently high total velocity should be maintained, especially if the sensor is located near the drone or straight below it. As demonstrated in section 4.6, the measured temperature can oscillate strongly if the drone is hovering at a fixed position.

While the limited maximum flight altitude means that the drones are unlikely to completely replace radiosoundings in vertical profiling of the atmosphere, they can still be

used to make valuable observations on the state of the boundary layer. In addition the drones could potentially be used to support radiosoundings or different remote-sensing instruments. The limited temporal coverage of the radiosoundings and the vertical coverage of remote-sensing instruments could be covered by drones in the lower altitudes, and using data-assimilation techniques these measurements together could be used to derive more accurate observations of the state of the atmosphere. This in combination with accurate weather prediction and climate models can help us gain even deeper understanding of the state and processes of the atmosphere.

REFERENCES

Allaby, M. (2013). Specific humidity. In: A Dictionary of Geology and Earth Sciences, 4th ed. Oxford University Press. Available: http://www.oxfordreference.com/view/10.1093/acref/9780199653065.001.0001/acref-9780199653065-e-7924

Atkins, T. & Escudier, M. (2013). Hydrostatic equation. In: A Dictionary of Mechanical Engineering. Oxford University Press. Available: http://www.oxfordreference.com/view/10.1093/acref/9780199587438.001.0001/acref-9780199587438-e-3006

Balin, I., Serikov, I., Bobrovnikov, S., Simeonov, V., Calpini, B., Arshinov, Y. & Bergh, H. van den (2004). Simultaneous measurement of atmospheric temperature, humidity, and aerosol extinction and backscatter coefficients by a combined vibrational–pure-rotational raman lidar. Applied Physics B, Vol. 79(6), pp. 775–782.

Barrera-Verdejo, M., Crewell, S., Löhnert, U., Orlandi, E. & Di Girolamo, P. (2016). Ground-based lidar and microwave radiometry synergy for high vertical resolution absolute humidity profiling. Atmospheric Measurement Techniques, Vol. 9(8), pp. 4013–4028.

Båserud, L., Reuder, J., Jonassen, M.O., Kral, S.T., Paskyabi, M.B. & Lothon, M. (2016). Proof of concept for turbulence measurements with the RPAS SUMO during the BLLAST campaign. Atmospheric Measurement Techniques, Vol. 9(10), pp. 4901–4913.

Butterfield, A.J. & Szymanski, J. (2018). A Dictionary of Electronics and Electrical Engineering, 5th ed. Oxford University Press. Available: http://www.oxfordreference.com/view/10.1093/acref/9780198725725.001.0001/acref-9780198725725

Chanin, M.L., Garnier, A., Hauchecorne, A. & Porteneuve, J. (1989). A doppler lidar for measuring winds in the middle atmosphere. Geophysical Research Letters, Vol. 16(11), pp. 1273–1276.

Childs, P., Greenwood, J. & Long, C. (2000). Review of temperature measurement. Review of scientific instruments, Vol. 71(8), pp. 2959–2978.

Committee Guides Metrology, J. (2008). Evaluation of measurement data - guide to the expression of uncertainty in measurement. JCGM (Joint Committee for Guides in Metrology), Vol. 100, p. 120.

Dabberdt, W., Shellhorn, R., Cole, H., Paukkunen, A., Hörhammer, J. & Antikainen, V. (2003). Radiosondes. In: Holton, J.R. (ed.), Encyclopedia of Atmospheric Sciences. Academic Press, Oxford, pp. 1900 – 1913. Available: http://www.sciencedirect.com/science/article/pii/B0122270908003444

Dellinger, J. (1911). The temperature coefficient of resistance of copper. Govt. Print. Off., Bulletin of the Bureau of Standards. Available: https://books.google.fi/books?id=0SbNypzYv7EC

Dirksen, R.J., Sommer, M., Immler, F.J., Hurst, D.F., Kivi, R. & Vömel, H. (2014). Reference quality upper-air measurements: GRUAN data processing for the vaisala RS92 radiosonde. Atmospheric Measurement Techniques, Vol. 7(12), pp. 4463–4490.

Drude, P. (1900). Zur elektronentheorie der metalle. Annalen der Physik, Vol. 306(3), pp. 566–613.

Engelmann, R., Kanitz, T., Baars, H., Heese, B., Althausen, D., Skupin, A., Wandinger, U., Komppula, M., Stachlewska, I.S., Amiridis, V., Marinou, E., Mattis, I., Linné, H. & Ansmann, A. (2016). The automated multiwavelength raman polarization and water-vapor lidar polly^{XT}: the next generation. Atmospheric Measurement Techniques, Vol. 9(4), pp. 1767–1784.

Fernald, F.G., Herman, B.M. & Reagan, J.A. (1972). Determination of aerosol height distributions by lidar. Journal of Applied Meteorology, Vol. 11(3), pp. 482–489.

Fernicola, V.C. & Iacomini, L. (2008). Approximating the its-90 temperature scale with industrial platinum resistance thermometers. International Journal of Thermophysics, Vol. 29(5), pp. 1817–1827.

Fisher, R.A. (1925). Statistical methods for research workers, 1st ed. Oliver & Boyd, Edinburgh.

Fontes, J. (2005). Chapter 20 - temperature sensors. In: Wilson, J.S. (ed.), Sensor Technology Handbook. Newnes, Burlington, pp. 531 – 561. Available: http://www.sciencedirect.com/science/article/pii/B9780750677295500604

Fraczek, M., Behrendt, A. & Schmitt, N. (2012). Laser-based air data system for aircraft control using raman and elastic backscatter for the measurement of temperature, density, pressure, moisture, and particle backscatter coefficient. Appl. Opt., Vol. 51(2), pp. 148–166.

Goldsmid, H.J. (2016). The thermoelectric and related effects. In: Introduction to Thermoelectricity. Springer Berlin Heidelberg, Berlin, Heidelberg, pp. 1–7. Available: https://doi.org/10.1007/978-3-662-49256-7_1

Google (2019a). Satellite picture of Finland. Imagery©2019 IBSAO Landsat / Copernicus, Data SIO,NOAA,U.S. Navy,NGA,GEBCO,IBCAO, Map data©2019 Google. Available: https://goo.gl/maps/a5NprDJX1NtbkRj56

Google (2019b). Satellite picture of Jokioinen measurement site. Imagery©2019 Google, Map data©2019 Google. Available: https://goo.gl/maps/mFFFWmQTVrrzvjyZ9

Greene, B.R., Segales, A.R., Bell, T.M., Pillar-Little, E.A. & Chilson, P.B. (2019). Environmental and sensor integration influences on temperature measurements by rotary-wing unmanned aircraft systems. Sensors, Vol. 19(6).

Guiraud, F.O., Howard, J. & Hogg, D.C. (1979). A dual-channel microwave radiometer for measurement of precipitable water vapor and liquid. IEEE Transactions on Geoscience Electronics, Vol. 17(4), pp. 129–136.

Halldórsson, T. & Langerholc, J. (1978). Geometrical form factors for the lidar function. Appl. Opt., Vol. 17(2), pp. 240–244.

Hashemian, H.M. & Petersen, K.M. (1992). Achievable accuracy and stability of industrial RTDs. In: Temperature. Its Measurement and Control in Science and Industry, Vol. 6. American Institute of Physics, New York, pp. 427 – 431.

Herwig, H. (2016). What exactly is the nusselt number in convective heat transfer problems and are there alternatives? Entropy, Vol. 18(5).

Hijikagawa, M., Miyoshi, S., Sugihara, T. & Jinda, A. (1983). A thin-film resistance humidity sensor. Sensors and Actuators, Vol. 4, pp. 307 – 315.

Hofmann, D.J., Rosen, J.M., Pepin, T.J. & Pinnick, R.G. (1975). Stratospheric aerosol measurements i: Time variations at northern midlatitudes. Journal of the Atmospheric Sciences, Vol. 32(7), pp. 1446–1456.

Huang, J. (2018). A simple accurate formula for calculating saturation vapor pressure of water and ice. Journal of Applied Meteorology and Climatology, Vol. 57(6), pp. 1265–1272.

Illingworth, A.J., Cimini, D., Gaffard, C., Haeffelin, M., Lehmann, V., Löhnert, U., O'Connor, E.J. & Ruffieux, D. (2015). Exploiting existing ground-based remote sensing networks to improve high-resolution weather forecasts. Bulletin of the American Meteorological Society, Vol. 96(12), pp. 2107–2125.

Immler, F., Dykema, J., Gardiner, T., Whiteman, D., Thorne, P. & Vomel, H. (2010). Reference quality upper-air measurements: guidance for developing gruan data products. Atmospheric Measurement Techniques, Vol. 3(5), pp. 1217–1231.

Jonassen, M.O., Tisler, P., Altstaedter, B., Scholtz, A., Vihma, T., Lampert, A., König-Langlo, G. & Lüpkes, C. (2015). Application of remotely piloted aircraft systems in observing the atmospheric boundary layer over antarctic sea ice in winter. Polar Research, Vol. 34: p. 15(25651).

Kipp & Zonen (2014). CGR4 Pyrgeometer instruction manual. Kipp and Zonen, Delftechpark 36, 2628 XH Delft. Manual version: V1401. Available: https://www.kippzonen.com/Download/38/Manual-CGR4-Pyrgeometer

Kubba, A.E., Hasson, A., Kubba, A.I. & Hall, G. (2016). A micro-capacitive pressure sensor: design and modelling. Journal of Sensors and Sensor Systems, Vol. 5(1), pp. 95–112.

Kuuluvainen, H., Poikkimäki, M., Järvinen, A., Kuula, J., Irjala, M., Maso, M.D., Keskinen, J., Timonen, H., Niemi, J.V. & Rönkkö, T. (2018). Vertical profiles of lung deposited surface area concentration of particulate matter measured with a drone in a street canyon. Environmental Pollution, Vol. 241, pp. 96–105.

Law, J. & Rennie, R. (2015). Temperature coefficient. In: A Dictionary of physics, 7th ed. Oxford University Press. Available: http://www.oxfordreference.com/view/10.1093/acref/9780198714743.001.0001/acref-9780198714743-e-3027

Lawrence, M.G. (2005). The relationship between relative humidity and the dewpoint temperature in moist air: A simple conversion and applications. Bulletin of the American Meteorological Society, Vol. 86(2), pp. 225–234.

Leosphere. Windcube vertical profiler lidar. Leosphere, 6A rue Rene Razel, 91 400 Saclay - France. Available: https://www.leosphere.com/products/windcube-vertical-profiler/

Lev, L. (2016). Humidity and temperature profiling radiometer at the barbados clouds observatory. Licence: Labzovskiy lev [CC BY-SA 4.0 (https://creativecommons.org/licenses/by-sa/4.0)]. Available: https://upload.wikimedia.org/wikipedia/commons/8/80/Microwaveradiometerbardabos.jpg

Luers, J.K. (1990). Estimating the temperature error of the radiosonde rod thermistor under different environments. Journal of Atmospheric and Oceanic Technology, Vol. 7(6), pp. 882–895.

Martin, S., Bange, J. & Beyrich, F. (2011). Meteorological profiling of the lower troposphere using the research UAV "M^2 AV Carolo". Atmospheric Measurement Techniques, Vol. 4(4), pp. 705–716.

Maschwitz, G., Löhnert, U., Crewell, S., Rose, T. & Turner, D.D. (2013). Investigation of ground-based microwave radiometer calibration techniques at 530 hpa. Atmospheric Measurement Techniques, Vol. 6(10), pp. 2641–2658.

Massaro, G., Stiperski, I., Pospichal, B. & Rotach, M.W. (2015). Accuracy of retrieving temperature and humidity profiles by ground-based microwave radiometry in truly complex terrain. Atmospheric Measurement Techniques, Vol. 8(8), pp. 3355–3367.

Moyers, C.G. & Baldwin, G.W. (1999). Psychrometry, evaporative cooling, and solids drying. Chapter 12 in: Perry, R., Green, D. & Maloney, J. (eds.), Perry's Chemical Engineers' Handbook, 7th ed. McGraw-Hill, McGraw-Hill CD-ROM Handbooks, pp. 1142–1231.

Münkel, C., Roininen, R. & Oyj, V. (2010). Investigation of boundary layer structures with ceilometer using a novel robust algorithm. American Meteorological Society, Techn. rep.

Okcan, B. & Akin, T. (2004). A thermal conductivity based humidity sensor in a standard cmos process. , pp. 552 – 555.

Palomaki, R.T., Rose, N.T., Bossche, M. van den, Sherman, T.J. & De Wekker, S.F.J. (2017). Wind estimation in the lower atmosphere using multirotor aircraft. Journal of Atmospheric and Oceanic Technology, Vol. 34(5), pp. 1183–1191.

Preston-Thomas, H. (1990). The international temperature scale of 1990 (its-90). Metrologia, Vol. 27(1), p. 3.

Rees, G. (2012). Physical principles of remote sensing. Cambridge University Press, Cambridge New York.

Reynolds, O. (1883). Xxix. an experimental investigation of the circumstances which determine whether the motion of water shall be direct or sinuous, and of the law of resistance in parallel channels. Philosophical Transactions of the Royal Society of London, Vol. 174, pp. 935–982.

Rose, T., Crewell, S., Löhnert, U. & Simmer, C. (2005). A network suitable microwave radiometer for operational monitoring of the cloudy atmosphere. Atmospheric Research, Vol. 75(3), CLIWA-NET: Observation and Modelling of Liquid Water Clouds, pp. 183 – 200.

Salasmaa, E. & Kostamo, P. (1986). Humicap® Thin Film Humidity Sensor. Springer Netherlands, Dordrecht, pp. 135–147. Available: https://doi.org/10.1007/978-94-009-4404-6_6

Schroeder, R., McDonald, K.C., Chapman, B.D., Jensen, K., Podest, E., Tessler, Z.D., Bohn, T.J. & Zimmermann, R. (2015). Development and evaluation of a multi-year fractional surface water data set derived from active/passive microwave remote sensing data. Remote Sensing, Vol. 7(12), pp. 16688–16732.

Skou, N. & Le Vine, D. (2006). Microwave Radiometer Systems : Design and Analysis. Artech House, Norwood, UNITED STATES. Available: http://ebookcentral.proquest.com/lib/tut/detail.action?docID=253353

Spencer, R.W., Christy, J.R. & Grody, N.C. (1990). Global atmospheric temperature monitoring with satellite microwave measurements: Method and results 1979–84. Journal of Climate, Vol. 3(10), pp. 1111–1128.

Steinhart, J.S. & Hart, S.R. (1968). Calibration curves for thermistors. Deep Sea Research and Oceanographic Abstracts, Vol. 15(4), pp. 497 – 503.

Strauch, R.G., Derr, V.E. & Cupp, R.E. (1971). Atmospheric temperature measurement using raman backscatter. Appl. Opt., Vol. 10(12), pp. 2665–2669.

Swindells, J.F. & States., U. (1958). Calibration of liquid-in-glass thermometers. U.S. Dept. of Commerce, National Bureau of Standards : For sale by the Supt. of Docs., U.S. G.P.O., Washington, D.C. ii, 21 p. Available: //catalog.hathitrust.org/Record/011445746

Vaisala (2018). Vaisala Dropsonde RD41. RD41 datasheet B211706EN-A. Available: https://www.vaisala.com/sites/default/files/documents/RD41-Datasheet-B211706EN.pdf

Wallace, J.M. & Hobbs, P.V. (2006). Atmospheric science: an introductory survey, 2nd ed., Vol. 92. Elsevier, 30 Corporate Drive, Suite 400, Burlington, MA 01803, USA.

Wandinger, U. (2005). Introduction to Lidar. Springer New York, New York, NY, pp. 1–18. Available: https://doi.org/10.1007/0-387-25101-4_1

Wandinger, U. & Ansmann, A. (2002). Experimental determination of the lidar overlap profile with raman lidar. Appl. Opt., Vol. 41(3), pp. 511–514.

Wentz, F.J., Gentemann, C., Smith, D. & Chelton, D. (2000). Satellite measurements of sea surface temperature through clouds. Science, Vol. 288(5467), pp. 847–850.

Wilks, D. (2005). Statistical Methods in the Atmospheric Sciences. Elsevier Science, International Geophysics. Available: https://books.google.fi/books?id=_b4R9j2Iy7EC

Yamazoe, N. & Shimizu, Y. (1986). Humidity sensors: Principles and applications. Sensors and Actuators, Vol. 10(3), pp. 379 – 398.

Yang, I., Suherlan, Gam, K.S. & Kim, Y.G. (2015). Interpolating equation of industrial platinum resistance thermometers in the temperature range between 0 °c and 500 °c. Measurement Science and Technology, Vol. 26(3), p. 035104.

Yoshitaka, S., Takamasa, Y., Yukihiko, M., Michiyoshi, N., Michihiko, T., Rikio, Y., Haruto, H. & Kiyoho, M. (2003). Development of the highest altitude balloon using the ultra thin polyethylen film (BU60-1). 宇宙科学研究所報告. 特集 , Vol. 45, pp. 1–10.